UNIVERSITAT
POLITÈCNICA
DE VALÈNCIA

DEPARTAMENTO DE
COMUNICACIONES

PhD Dissertation

New quasi-TEM waveguides using artificial surfaces and their application to antennas and circuits.

Universitat Politècnica de València

Departamento de Comunicaciones

Author

Esperanza Alfonso Alós

Advisor

Dr. Alejandro Valero Nogueira

Valencia, June 2011

A mi familia.

Preface

This work was initiated in 2005 with the objective of studying a new proposal for low-cost high-gain planar antennas for millimeter-wave applications. This proposal, the so-called Single Hard Wall Waveguide (SHWW), is based on the use of soft/hard surfaces within oversized rectangular waveguides to feed planar slot arrays. The research has been developed in the Electromagnetic Radiation Group, headed by Prof. Miguel Ferrando Bataller, at the iTeAM Institute of the Universidad Politécnica de Valencia (UPV), and supervised by Prof. Alejandro Valero Nogueira. This work has been supported in part by the Universidad Politécnica de Valencia under a 4-year PhD grant (the FPI-UPV program), and by the Spanish Ministerio de Ciencia e Innovacion under projects TEC2007-66698-C04-03 and PTA2008-0892-P.

The need of a deeper understanding of the soft/hard surface concept led me to visit Prof. Kildal's group at Department of Signals and Systems at Chalmers University of Technology, during 3 months the Autumn 2007. Prof. Per-Simon Kildal established the definition of soft/hard surfaces in 1989. And since then, he has done many contributions to the study and application of these surfaces. This visit not only meant a encouragement to our research, but also inspired the invention of a new gap waveguide by Prof. Kildal. This waveguide has a large application potential, in particular to the realization of circuits and components at the millimeter-wave band. The first studies on this waveguide were carried out during a second visit to Kildal's group during 3 months the Autumn 2008. Further works on the study and development of this new technology were later done in Valencia. Gap waveguides are now being investigated in several research groups (UPV, Chalmers, Siena, Zagreb, Mississippi).

Agradecimientos - *Acknowledgments*

Sois muchas las personas que a lo largo de estos años habéis estado conmigo, y que de una u otra forma, aún sin ser conscientes de ello, habéis contribuido a la realización de esta tesis. A todos vosotros os la quiero dedicar.

Quiero transmitiros mi más sincera gratitud, porque sin vosotros no habría encontrado la fuerza, la calma y la ilusión necesarias para llegar hasta aquí. No es mi intención nombraros directamente, pues estoy segura de que de sobra sabéis lo importantes que habéis sido para mí cada uno de vosotros, tan solo lo haré cuando no pueda evitarlo. Os llevo en mi recuerdo y en mi corazón, y os voy a estar por siempre agradecida, a todos.

Me gustaría empezar por mi tutor. Gracias Alejandro, por darme la oportunidad de emprender este camino. Gracias por acompañarme en todo momento, por guiarme, y confiar en mí. Gracias por tu ayuda, tu apoyo, paciencia y dedicación.

Gracias José Ignacio, por ordenar mis pensamientos tantas veces, por todo lo que he podido aprender contigo. Gracias por tu inestimable ayuda, interés y seguimiento de este trabajo. Gracias por tu continuo apoyo y absoluta disposición. Ojalá puedas ayudar a otros tanto como a mí.

Gracias Mariano, por la ayuda prestada. Gracias por tus consejos, tiempo y dedicación. Gracias por implicarte y hacer posible una mayor colaboración con el grupo de investigación en el que estuve de estancia, y al cual me incorporaré tras finalizar esta etapa.

Gracias Miguel, porque como director de nuestro grupo siempre has velado por nuestros intereses, facilitándonos los medios necesarios para desempeñar nuestro trabajo en las mejores condiciones. Gracias por contribuir a nuestra formación proporcionándonos la oportunidad de asistir a cursos, congresos, etc. Gracias por felicitarnos por nuestros logros, animarnos, y compartir tus ideas y tu pasión por tu trabajo.

Gracias encargados del laboratorio, por vuestra importante labor, pieza fundamental con la que deben culminar la mayoría de nuestros trabajos. Gracias por el apoyo y el afecto recibidos, y por hacer del laboratorio un lugar de descanso para todos.

Gracias amigos y compañeros del GRE, gracias a todos por vuestros ánimos, apoyo, afecto y confianza. Son muchos los años que nos hemos tenido que soportar, muchas las experiencias vividas, mucho lo que me habéis enseñado, y todo eso ya forma parte de mí. En especial, gracias Dani, por mantenerte cerca, por ayudarme, apoyarme y animarme durante todo este tiempo. Gracias por estar ahí.

Gracias también compañeros de oficina y compañeros del iTeAM, muchos de vosotros pertenecientes al GCM, gracias por vuestro interés y vuestra compañía en los momentos de descanso.

Thanks Per-Simon for welcoming me warmly in your group and allowing me to have such a great experience. Thanks for encouraging me to carry on and for involving us in collaboration works with other researchers. Thanks to all the members of Antenna group in Chalmers and the people I met during my two research stays in Gothenburg for your hospitality, attention and company. Thanks for making me feel like at home and letting me enjoy of a nice multi-cultural atmosphere.

Gracias amigos, gracias por hacer la vida más alegre, por ayudar a mantener viva la ilusión, por obligarme a desconectar de vez en cuando. Gracias Elías, gracias Ana, gracias por lo que ha representado para mí vuestra amistad durante mis años de universidad. Gracias por vuestra compañía, por vuestro tiempo y reflexiones. Gracias por poder contar siempre con vosotros, sin importar la distancia. Y gracias Pelayo, porque conocerte fue un regalo que siempre perdurará.

Y por último, como no, gracias familia. Gracias por quererme tanto, por estar siempre a mi lado bajo cualquier circunstancia, por tantos sacrificios y tanta comprensión, por ayudarme a que mis ilusiones se hagan realidad, porque gracias a vosotros soy como soy. Gracias por ser mi brújula, a la que tengo que recurrir para orientarme y sin la que no podría continuar mi camino.

En fin, gracias a todos por acompañarme en este largo viaje, que va a continuar gracias a vosotros, y me encantaría que continuase muchos años más.

Abstract

Research interest: In recent years we have seen the emergence of commercial applications at high frequencies, such as the top part of the microwave band and the millimeter and sub-millimeter bands, and it is expected a big increase in the coming years. This growing demand requires a rapid development of low-cost technology with good performance at these frequencies, where common technologies, such as microstrip and standard waveguides, have some shortcomings. In particular, existing solutions for high-gain planar scanning antennas at these frequencies suffer from the disadvantages of these technologies giving rise to high-cost products not suitable for high volume production.

Objectives: The main objective of this thesis is to study the feasibility of a new proposal to improve existing solutions to date for low-cost high-gain planar scanning antennas at high frequencies. This overall objective has resulted in another central objective of this thesis, which is the research of new quasi-TEM waveguides that are more appropriate than current technologies for the realization of circuits and components at these frequency bands. These guided solutions make use of periodic or artificial surfaces in order to confine and channel the fields within these waveguides.

Methodology: The work follows a logical sequence of specific tasks aimed at achieving the main objective of this thesis. Chapter 2 presents the proposed guiding solution and shows its performance numerical and experimentally. The optimized design of high-gain antennas based on waveguide slot arrays requires the development of efficient ad-hoc codes. The implementation and validation of this code is presented in Chapter 3, where a new method for the analysis of corrugated surfaces is proposed, and in Chapter 4, which extends this code to the analysis of waveguide slot arrays. The process design and optimization of a two-dimensional array is described in Chapter 5, where a preliminary experimental validation is also described. Moreover, the proposed guiding solution has inspired the development of a new guiding technology of wider bandwidth and more versatile for the realization of circuits and components at high frequencies. Chapter 6 presents the contributions to the study of this technology and its application to the design of circuits.

Results: It has been shown numerical and experimentally that the two guiding structures, which have been studied here, one designed to support a slot array, and the other one especially interesting for the realization of circuits and components, have particular characteristics that give them great potential for application in antennas and circuits at high frequencies. The feasibility study culminates with the design of a two-dimensional slot array fed by the proposed guide. For this design an efficient ad-hoc code based on a new method for the analysis of corrugated surfaces has been used. This numerical implementation is one of the main contributions of this work. The application of the second guiding structure to the realization of circuits has been demonstrated through the design, fabrication and measurement of some microwave circuits.

Resumen

Interés de la investigación: En los últimos años hemos asistido a la aparición de aplicaciones comerciales a frecuencias elevadas, como son la parte alta de la banda de microondas y las bandas de milimétricas y submilimétricas, y se espera un incremento en los próximos años. Esta creciente demanda exige un rápido desarrollo de tecnología de bajo coste con buenas prestaciones a estas frecuencias, donde las tecnologías más comunes, como son la tecnología microstrip y las guías de onda, presentan algunas deficiencias. En concreto, las soluciones existentes para antenas planas de barrido de alta ganancia a estas frecuencias sufren los inconvenientes de dichas tecnologías y dan lugar a productos con un coste demasiado alto para su producción masiva.

Objetivos: El objetivo principal de la presente tesis doctoral consiste en estudiar la viabilidad de una nueva propuesta que mejore las soluciones existentes hasta la fecha en lo referente a antenas planas de barrido de alta ganancia y bajo coste a frecuencias elevadas. Este objetivo global ha desembocado en otro objetivo central de esta tesis que consiste en la investigación de nuevas guías cuasi-TEM más apropiadas que las tecnologías actuales para la realización de circuitos y componentes en estas bandas de frecuencia. Estas soluciones guiadas hacen uso de superficies periódicas o artificiales con la finalidad de confinar y dirigir los campos en el interior de estas guías.

Metodología: El trabajo desarrollado sigue una secuencia lógica de tareas específicas encaminadas a la consecución del objetivo principal de esta tesis. En el capítulo 2 se presenta la solución guiada propuesta y se muestra su funcionamiento numérica y experimentalmente. El diseño optimizado de antenas de alta ganancia basadas en agrupaciones de ranuras en guía exige el desarrollo de códigos propios eficientes. La implementación y validación de este código se presenta en el capítulo 3, donde se propone un nuevo método para el análisis de superficies corrugadas, y en el capítulo 4, donde se extiende este código para el análisis de agrupaciones de ranuras en guía. El proceso de diseño y optimización de una agrupación bidimensional se describe en el capítulo 5, donde se expone también una validación experimental preliminar. Por otra parte, la solución

guiada propuesta ha inspirado la aparición de una tecnología guiada con mayor ancho de banda y más versátil para la realización de circuitos y componentes a frecuencias elevadas. El capítulo 6 presenta las contribuciones realizadas al estudio de esta tecnología y a su aplicación en el diseño de circuitos.

Resultados: Se ha demostrado numérica y experimentalmente que las dos estructuras guiadas estudiadas aquí, una ideada como soporte de una agrupación de ranuras, y la otra especialmente interesante para la realización de circuitos y componentes, presentan unas características particulares que les confieren un gran potencial para su aplicación en antenas y circuitos a frecuencias elevadas. El estudio de viabilidad culmina con el diseño de una agrupación de ranuras bidimensional en la guía propuesta. Para este diseño se ha empleado un código propio eficiente basado en un método nuevo para el análisis de superficies corrugadas, el cual constituye una de las aportaciones principales de este trabajo. La aplicación de la segunda estructura guiada en la realización de circuitos se ha demostrado mediante el diseño, fabricación y medida de circuitos de microondas.

Resum

Interés de la investigació: En els últims anys hem assistit a l'aparició d'aplicacions comercials a freqüències elevades, com són la part alta de la banda de microones i les bandes de milimètriques i sub-milimètriques, i s'espera un increment en els propers anys. Aquesta creixent demanda exigeix un ràpid desenvolupament de tecnologia de baix cost amb bones prestacions a aquestes freqüències, on les tecnologies més comuns, com són la tecnologia microstrip i les guies d'ona, presenten algunes deficiències. En concret, les solucions existents per a antenes planes de rastreig d'alt guany a aquestes freqüències pateixen els inconvenients d'aquestes tecnologies i donen lloc a productes amb un cost massa alt per a la seva producció massiva.

Objectius: L'objectiu principal d'aquesta tesi doctoral consisteix a estudiar la viabilitat d'una nova proposta que millore les solucions existents fins ara pel que fa a antenes planes de rastreig d'alt guany i baix cost a freqüències elevades. Aquest objectiu global ha desembocat en un altre objectiu central d'aquesta tesi que consisteix en la recerca de noves guies quasi-TEM més apropiades que les tecnologies actuals per a la realització de circuits i components en aquestes bandes de freqüència. Estes solucions guiades fan ús de superfícies periòdiques o artificials amb la finalitat de confinar i dirigir els camps en l'interior d'aquestes guies.

Metodologia: El treball desenvolupat segueix una seqüència lògica de tasques específiques encaminades a la consecució de l'objectiu principal d'aquesta tesi. En el capítol 2 es presenta la solució guiada proposta i es mostra el seu funcionament numèrica i experimentalment. El disseny optimitzat d'antenes d'alt guany basades en agrupacions de ranures en guia exigeix el desenvolupament de codis propis eficients. La implementació i validació d'aquest codi es presenta en el capítol 3, on es proposa un nou mètode per a l'anàlisi de superfícies corrugades, i en el capítol 4, on s'estén aquest codi per a l'anàlisi d'agrupacions de ranures en guia. El procés de disseny i optimització d'una agrupació bidimensional es descriu en el capítol 5, on s'exposa també una validació experimental preliminar. D'altra banda, la solució guiada proposta ha inspirat l'aparició d'una tecnologia guiada amb major ample de banda i més versàtil

per a la realització de circuits i components a freqüències elevades. El capítol 6 presenta les contribucions realitzades a l'estudi d'esta tecnologia i a la seua aplicació en el disseny de circuits.

Resultats: S'ha demostrat numèrica i experimentalment que les dues estructures guiades estudiades ací, una ideada com a suport d'una agrupació de ranures, i una altra especialment interessant per a la realització de circuits i components, presenten unes característiques particulars que els confereixen un gran potencial per a la seua aplicació en antenes i circuits a freqüències elevades. L'estudi de viabilitat culmina amb el disseny d'una agrupació de ranures bidimensional en la guia proposta. Per a aquest disseny s'ha emprat un codi propi eficient basat en un mètode nou per a l'anàlisi de superfícies corrugades, el qual constitueix una de les aportacions principals d'aquest treball. L'aplicació de la segona estructura guiada en la realització de circuits s'ha demostrat mitjançant el disseny, fabricació i mesura de circuits de microones.

Table of contents

List of Figures

List of Tables

LIST OF TABLES

Acronyms

1-D   1-Dimensional

2-D   2-Dimensional

3-D   3-Dimensional

ACBC   Asymptotic Corrugated Boundary Conditions

AIE   Aperture Integral Equation

AMC   Artificial Magnetic Conducting

AR   Axial Ratio

CG   Conjugate Gradient

CG-FFT   Conjugate Gradient - Fast Fourier Transform

CP-RLSA   Circularly Polarized Radial Line Slot Array

DBS   Direct Broadcast Satellite

EBG   Electromagnetic BandGap

FWA   Fixed Wireless Access

HIS   High Impedance Surface

IBC   Impedance Boundary Condition

LH-CP   Left Handed Circularly Polarized

LP-RLSA   Linearly Polarized Radial Line Slot Array

MMIC   Monolithic Microwave Integrated Circuit

MoM   Method of Moments

ACRONYMS

PBG	Photonic BandGap
PCB	Printed Circuit Board
PEC	Perfect Electric Conducting
PMC	Perfect Magnetic Conducting
PPW	Parallel Plate Waveguide
RCS	Radar Cross Section
RGW	Ridge Gap Waveguide
RLSA	Radial Line Slot Array
RW	Rectangular Waveguide
SHWW	Single Hard Wall Waveguide
TE	Transverse Electric
TEM	Transverse ElectroMagnetic
TM	Transverse Magnetic
VSWR	Voltage Standing Wave Ratio
WLAN	Wireless Local Area Network

Chapter 1

Introduction

The proliferation of wireless and multimedia applications nowadays is arising design challenges for greater functionality and better performance in smaller size. In addition, since the lower part of the radioelectric spectrum is running out, the current tendency is moving towards upper frequencies such as the microwave and millimeter- and submillimeter-wave bands that provide wider bandwidth.

It is expected an imminent expansion of applications at these bands, where there are already working some, such as Direct Broadcast Satellite (DBS) at 12 GHz [1], radiolinks for mobile system base stations at 22 GHz [2], Fixed Wireless Access (FWA) systems at 26 GHz [3], Wireless Local Area Networks (WLAN) at 60 GHz [4], or car collision avoidance radars at 76 GHz [5]. The gradual occupation of these frequency bands for commercial applications demands a fast development of low-cost technology appropriate for such bands, which have been mainly used for military applications.

The use of the millimeter-wave band is very challenging for antenna designers. Not only from the mechanical point of view, given the smaller size of all the elements involved, but also from the antenna radiation efficiency. For low profile antennas, the use of microstrip patch arrays entails high losses at the distribution network. Therefore, it is more convenient using waveguides to distribute the power to the radiating elements. The most common arrangement consists of juxtaposed monomode rectangular waveguides. This solution is generally adopted for antennas requiring control of the beam steering. However, these structures are generally expensive and thus not much feasible for commercial applications.

During the last years, researchers have worked on the development of high gain antennas for these bands using simplified waveguide based structures that reduce the cost keeping acceptable performance. However, such solutions are

not completely satisfactory with regard to the bandwidth or beam steering ability, a very interesting feature for satellite mobile communications.

The solution commonly adopted, based on monomode waveguides, presents serious problems in the manufacturing process derived from the physical constraints imposed by the design itself to meet antenna specifications, especially for applications over 30 GHz. As it is well-known from array theory, array elements must be equally spaced apart a maximum distance to avoid grating lobes. This maximum distance is even smaller for beam tilting. On the other hand, rectangular waveguides cannot be as narrow as desired because they could be below cut-off. In order to fulfill these requirements the internal walls are made as thin as possible, but if they are very thin the milling technique could be not suitable in the manufacture. Even so, the design normally forces the waveguides to work close to the cut-off frequency, where losses at sidewalls are higher, especially at the millimeter- and submillimeter-wave bands. Besides, these waveguide slot arrays are usually made in two parts, the bottom part consisting of a groove surface, and the top part, which is a metal plate containing the radiating slots. Both parts have to be joined together later assuring a good electrical contact at joints. The previous drawback added to the fact that the plate is never completely flat, presenting protrusions and irregularities, lead to a difficult manufacturing process, which increase the final cost making these antennas only affordable for military applications.

Several attempts have been made at Tokio Institute of Technology to solve the junction problem. One proposal consists of alternating phase-fed waveguides, where adjacent waveguides are fed with opposite phase. The net current at joints is zero so that a perfect electric contact is not required. Other solution is based on oversized waveguides, electrically wide, fed by a quasi-TEM wave, which is a combination of TE modes. However, these solutions are narrow band and not valid for phase-scanning. Therefore, there is a need for new waveguide feeders for steerable slot arrays for commercial applications at high frequencies.

Slot arrays have been used as high gain antennas at high frequencies for many commercial and military applications with low manufacturing cost. Most of the designs come from Tokio Institute of Technology [6], [7], although some works have been also published at Technical University of Madrid (UPM) [8], Queensland University in Australia [9], and Technical University of Valencia (UPV) [10]. The design of these antennas has risen during the last three decades. Such designs can be classified depending on the type of feeding waveguide as: radial waveguide, monomode rectangular waveguide array, and multimode or oversized rectangular waveguide.

The radial waveguide gives rise to the most simple structure, the Radial Line Slot Array (RLSA). This structure is basically a parallel-plate waveguide, which is fed by a coaxial probe generally at its center. This simple excitation and an appropriate arrangement of the slots at the upper metal plate can

provide circular polarization (CP-RLSA) [1], [11] and linear polarization (LP-RLSA) [12], [13]. However, as a consequence of the matching problems of LP-RLSA, there are many more references about CP-RLSA designs than LP-RLSA designs. The main application of a CP-RLSA is DBS reception that uses circular polarization in Japan. The research on these antennas has been mostly promoted by Tokio Institute of Technology getting very high efficiencies [14]. Nevertheless, this type of antennas is not versatile for mobile applications, thus the use of rectangular waveguides, that allow electronic control of the beam steering, is more common.

A monomode rectangular waveguide has usually been the support of 1-Dimensional (1-D) slot arrays for circular [15], [16] and linear polarization [17]. The location and orientation of the slots are designed to obtain a given radiation pattern and polarization. Later, these concepts have been applied to the development of high gain planar antennas. The evolution towards 2-Dimensional arrays has taken two alternatives. The first one consists of the juxtaposition of a group of slotted monomode waveguides, fed by a proper distribution network at the same layer. The design complexity lies on the distribution network, since the slot arrangement over the waveguides is similar to the 1-D case. The manufacture is high-cost mainly due to the thin internal walls that should have a perfect electric contact with the slotted metal plate.

One of the first designs of this type is reported in [18]. The radiating element is formed by two crossed slots to provide circular polarization as shown in Fig. 1.1(a). As in most of the designs, the distribution network exciting the radiating waveguides is a perpendicular waveguide, which is fed by a monomode port. The transition between this waveguide and the radiating waveguides is done by means of windows of π-union type which are duly designed to match the input and provide a uniform magnitude pattern among the radiating waveguides. All the input power is radiated by the slots so that it works like a leaky-wave antenna [19]. Regarding to the design of the radiating elements, a method of moments formulation and periodic boundaries are used in the analysis [20]. Following this design, an antenna of dual polarization with two different beams was demonstrated in [21]. Due to the strong mutual coupling of a leaky-wave antenna, a more rigorous analysis of each of the radiating waveguides as exposed in [22]-[24] can be required. It is worth noting that even though their low impact, other radiating elements for circular polarization were published [25]-[27].

The same feeding structure can also be used for linear polarization, modifying the slots properly. The radiating element consists of a slot, which can be transverse or longitudinal to the propagation direction in the monomode waveguides. The first design, proposed in [28], makes use of transverse slots (see Fig. 1.1(b)). The slots are one wavelength, λ, equally spaced apart for broadside radiation. Therefore, the reflected waves coming from the radiating

(a) crossed slots for circular polarization   (b) transverse slots for linear polarization
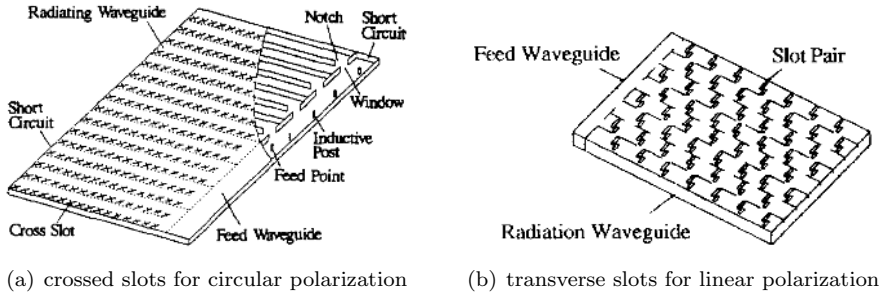
Figure 1.1: Array of monomode waveguides as feeding structure for slot array antennas.

elements are added up in phase within the waveguide, what leads to a bad input matching. This drawback is usually alleviated by adding a group of canceling slots, which are located at $\lambda/4$ away from the original ones so that they cancel the reflections coming from the former. An alternative solution for canceling reflections can be found in [29].

Owing to the high cost of the internal sidewalls manufacture, other technology has been applied to the manufacture of these waveguides. The post wall technology replace the sidewalls by a group of metal posts close to each other. This waveguides are also known as laminated waveguides [30] or Substrate Integrated Waveguides (SIW) [31]. The use of this technology reduces the manufacturing cost especially at high frequencies since it takes benefits of mature manufacturing techniques like etching slots and drilling via holes in a Printed Circuit Board (PCB) [32]-[34].

Nevertheless, the most common alternative for linear polarization employs longitudinal slots. Such slots are $\lambda/2$ spaced with opposite offsets with respect to the alignment axis to compensate the phase difference, as shown in Fig. 1.2 (a). This is the typical design of a 1-D slot array, but now is replicated to obtain a highly directive antenna. The first example of this type is reported in [35]. In order to improve the matching, slot locations are usually modified so that the reflected waves do not add up in phase, what causes a tilted radiated beam of a few degrees [36]-[37]. Taking this first design as a starting point, different variants have arisen, which try to solve some difficulties or add new functions [38]-[42].

The main drawback of this type of antennas is the manufacturing cost, since there must be perfect conducting joints between the internal sidewalls and the slotted plate, which are manufactured separately. As a solution to this problem, a new design comes up that consists of alternating phase waveguides, where adjacent waveguides have a phase difference of 180° [43]. To provide such
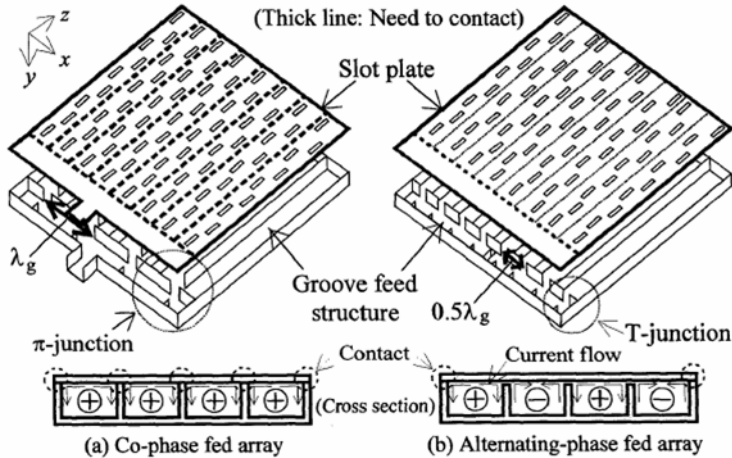
Figure 1.2: Longitudinal slots for linear polarization on an array of monomode waveguides.

phase difference the distribution network is changed including T-type unions instead of π-type unions, as can be seen in Fig. 1.2 (b). The net current at the joints is zero, therefore a perfect electric contact to the upper plate is not required, what allows to join both parts using some screws. However this improvement is done at the expense of a reduction of efficiency and bandwidth [44], [45]. Better efficiencies were obtained later including chokes [46], [3]. These designs have been recently modified in order to improve the bandwidth. That is done moving the distribution waveguide to the central part of the radiating waveguides [47]. However, this change increases the sidelobe level due to the blocking introduced by the central distribution waveguide over which there are no radiating slots. Several proposals have been done to solve this problem, like in [48], [49] where Taylor distributions are used, or trying to reduce the blocking using different types of unions for the central distribution waveguide [50]-[52]. On the other hand, a recent evolution uses a distribution waveguide oriented obliquely with respect to the cross section of the monomode waveguides so that the reflections coming from the radiating waveguides do not add up in phase and in consequence the input matching is improved [53].

Despite the antennas fed by an array of monomode waveguides have good performance for professional applications, the manufacturing cost is slightly high for volume production for commercial applications. This extra-cost principally comes from the internal sidewalls of the radiating waveguides. Thus, their suppression would help to a simpler construction, especially at high fre-
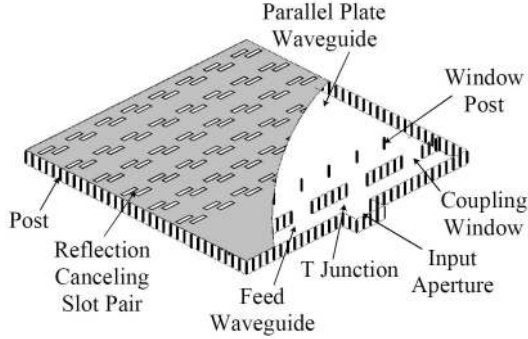
Figure 1.3: Post-wall oversized rectangular waveguide fed slot array.

quencies. That is the reason for the second design alternative of 2-Dimensional (2-D) waveguide slot arrays to appear. This alternative uses an oversized multimode rectangular waveguide as feeder of the slot array. The desired mode has to be excited inside the waveguide. Besides, a uniform magnitude pattern is always preferred. In this sense, it is usual to excite a combination of modes, which has similar characteristics to a Transverse ElectroMagnetic (TEM) mode. For this purpose, a group of sources of uniform magnitude are located in a cross section of the waveguide. This has been done in three different ways: by windows in a distribution waveguide at the same layer, by slots on a distribution waveguide located at a different layer [54], or by a microstrip corporate network [55]-[57].

The excitation by means of a distribution waveguide at the same layer is the most common one and the one frequently used in the designs developed at Tokio Institute of Technology. The feeding structure is very similar to that one used for antennas based on an array of monomode waveguides except for the internal sidewalls, which have been suppressed. In general, this type of antennas make use of the post-wall technology, what reduces even more its cost (see Fig. 1.3). The first design of this type is reported in [58] where 45° oriented slots are used for linear polarization and additional slots are also included as reflection canceling elements. The key point of these antennas lies on a good design of the windows, which couple the field at the input port to the multimode waveguide in which the generation of a quasi-TEM mode is intended [59]. Some examples can be found in [5], [60]. These antennas are narrow-band since the quasi-TEM mode is a combination of many modes. Regarding to the analysis, it is common the use of the method of moments with periodic boundary conditions [61]. Other more rigorous methods can be found in [62]. It should be stressed that this waveguide supports many modes so that even if the excitation generates a given field pattern, its preservation is not guaranteed.

The field pattern is strongly distorted as passes for the radiating slots, what affects to the overall performance. As a consequence of the multimode feature of this waveguide, it is very difficult to control the magnitude and phase of the radiating elements. Therefore, the general performance of this kind of antennas is narrow-band and not suitable for phase-scanning applications. However, they exhibit low manufacturing cost due to the lack of internal sidewalls.

On the other hand, during the last years there has been an explosion of research on new periodic structures widely known as metamaterials [63]-[67]. These structures can be made up of metal, dielectric materials, or both, and they have special properties, which are not normally found in nature. Their interest lies on their ability to modify the propagation properties of microwave devices and antennas [68], [69]. The origin of these structures is the Photonic BandGap (PBG) technology in the optical domain [70]. Since Yablonovitch explored for first time in 1987 the PBG technology in the microwave band the number of publications has increased drastically [71].

One type of metamaterials are the electromagnetic bandgap (EBG) materials. They have frequency bands (so-called bandgaps or stopbands) within which field propagation is not allowed. The EBG surfaces are also known as High Impedance Surfaces (HIS) because they show a very high surface impedance. Thus, they behave like Artificial Magnetic Conductors (AMC) for normal or close to normal incidence. These particular properties make them very attractive for improving the performance of microwave devices and antennas. Among the multiple applications, we can mention its use on low profile microstrip antennas [72], [73], the suppression of surface waves in patch antennas [74], [75], the reduction of the coupling between patch antennas [76], or the prevention of the leakage of cavity backed coplanar waveguides [77]. These surfaces have also been recently made electronically tunable by means of integrated active components and applied to reconfigurable antennas [78], [79].

One interesting application of these surfaces is reported in [80]. They are located on the sidewalls of a rectangular waveguide in order to achieve a TEM propagation with a uniform field pattern inside (see Fig. 1.4). TEM waveguides have been traditionally obtained using dielectric substrates on the sidewalls of standard metal waveguides. These waveguides, also known as hard waveguides, have been used as radiating structures in phased arrays [81], as feeding structures for planar slot arrays [82], and applied to hard horns for power amplifiers [83], [84]. Higher permittivity values provides better performance at a expense of a reduction of bandwidth. The use of EBG sidewalls instead gives wider bandwidths, but still can be narrow for some applications. An oversized waveguide of this type is used in [85] to feed a 2-D slot array. A slightly different example can be found in [86], where a squared TEM waveguide with dual polarization is obtained by using 1-D EBG surfaces over all the walls of a squared metal waveguide [86]. Additionally, other related proposal has been
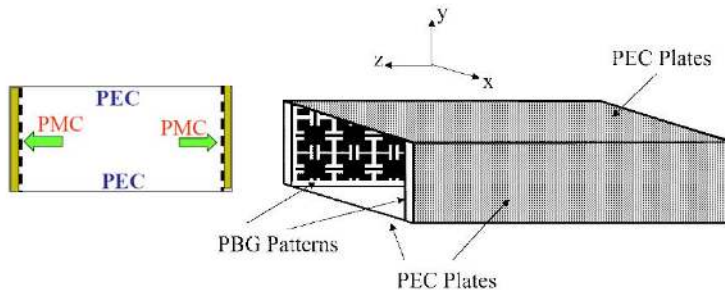
Figure 1.4: Rectangular waveguide with EBG sidewalls for quasi-TEM propagation.

published in [87], where AMC-Perfect Electric Conducting(PEC)-AMC strips are used on the walls of a parallel-plate waveguide with the purpose of emulating the behavior of a conventional rectangular waveguide without using metal sidewalls. AMC strips works like virtual electric walls. This guiding structure was applied later in [88] to feed a 1-D slot array. The handicap of this structure to feed 2-D slot arrays lies on the minimum AMC strip width that should be kept to work like virtual electric walls. The working principle and an experimental validation of this structure are reported in [89].

Soft/hard surfaces are directly connected with EBG surfaces since they show a bandgap within which there is no field propagation. But whereas an EBG surface has a bandgap for any direction, the bandgap in a soft/hard surface appears only for a given direction. In this sense, soft/hard surfaces can also be seen like the 1-D equivalent of an EBG surface. They are usually made up of corrugations or etched strips on a grounded substrate [90], [91]. Corrugations have been traditionally used from the sixties as chokes to reduce the coupling [92],[93], to design horn antennas with symmetrical radiation patterns and low cross-polarization [94]-[96], and for compact hard horns [97]-[100].

Soft/hard surface concept was established in [101], [90]. A surface is soft or hard in a given direction if stops or allows, respectively, field propagation in that direction regardless of its polarization. The soft or hard behavior appears when the corrugations/strips are oriented perpendicular or parallel, respectively, to the propagation direction. Alternatively, these surfaces can be ideally seen as a grid of parallel Perfect Electric Conducting / Perfect Magnetic Conducting (PEC/PMC) strips [102]. The definition of these surfaces and other canonical surfaces in terms of the boundary conditions and characteristic impedance can be seen in Fig. 1.5 [103].

Since then, a large number of publications on numerical studies of these soft/hard surfaces can be found in the literature [104]-[109]. Different ways of
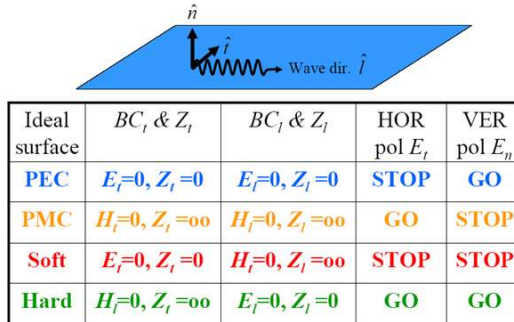
Figure 1.5: Boundary conditions and surface impedances of some canonical surfaces.

realization of these surfaces have been investigated [110]-[113]. Among them it is worth mentioning the planar versions of standard corrugations, and its realization using via-holes and etched strips on a grounded substrate. Regarding to the applications, apart from the above-mentioned, it can be highlighted the reduction of mutual coupling between antennas [76], their use as grounded planes of planar antennas to reduce the back radiation [114], and covering masts to reduce the blocking caused by these masts present in reflectors [115]. This latter application was related later in [116], [117] to the cloaking concept in view of the emergence of new structures that are able to make objects invisible at a given frequency [118].

It has been shown that such periodic or artificial surfaces, in particular soft/hard surfaces and EBG surfaces or HIS, are able to modify propagation and radiation properties of antennas and microwave devices. Oversized rectangular waveguides could benefit from the use of these artificial surfaces in order to control the fields and guide the waves in the desired directions within these waveguides without resorting to internal metal sidewalls.

1.1 Objectives and structure of the thesis

The main objective of the present thesis is the development of a viability study of a new proposal for low-cost high-gain steerable planar antennas at high frequencies. This new proposal is an alternative solution for this type of antennas, which, as it has already been exposed, shows some deficiencies and manufacturing problems, especially at the millimetre- and submillimetre-wave bands. For these frequency bands, there is a lack of low-cost and good performance technology not only for antennas, but also for transmission lines and waveguide devices for commercial applications.

A very interesting application of this type of antennas is the satellite mobile TV reception where the control of the beam pointing is essential. Besides, a key point for commercial applications is the manufacturing cost. Waveguide slot arrays represent a promising solution for high-gain applications at high frequencies, in particular for mobile applications. However, the existing solutions are not completely satisfactory regarding to the cost or with respect to the bandwidth and beam steering capability. A new guiding structure, which has been called Single Hard Wall Waveguide (SHWW), is proposed here to feed slot arrays. This solution could go beyond such limitations. Therefore, the general objective is the viability study of this alternative solution. For this aim, a number of specific objectives has been established from chapter 2 where the new structure is proposed to chapter 5 where a complete design of a SHWW fed 2-D slot array antenna is shown.

In addition, this research work has been inspiration for the emergence of a new waveguide technology invented by Professor Per-Simon Kildal in Chalmers University of Technology, the so-called Ridge Gap Waveguide (RGW). Provided the apparent potential of this technology to make circuits and components for the millimetre- and submillimetre-wave bands, and the possibility of integration with SHWW fed slot arrays, some contributions to the development of this technology have also been done in this work. They are reported in chapter 6.

Chapter 2 presents the propagation properties and performance characteristics of SHW-Waveguides. The first objective is the description of the guiding structure and the study of its propagation properties by using commercial electromagnetic simulators. A demonstration of the ability of this waveguide to guide multiple independent local quasi-TEM waves along the longitudinal direction is shown. Then, the second objective is to find a way of characterizing this waveguide in order to be able to evaluate its performance for different realizations of hard surfaces and to carry out optimizations of the geometrical parameters. Such characterization is based on the performance of these confined waves. Finally, the last objective of this chapter is the experimental demonstration of a low-cost realization of the guiding structure.

Once the propagation properties of the proposed solution have been shown numerical and experimentally, we should think on its application to feed slot arrays. Waveguide slot array antennas are normally used for high-gain applications, thus they can be electrically very large and contain a high number of radiating elements. An optimized design of these large antennas can take hundreds of iterations to fulfil the design specifications. Therefore, a rigorous and efficient ad-hoc code for this problem in particular is needed. To this aim, a Method of Moments (MoM) formulation based on the Aperture Integral Equation (AIE) is proposed and presented in chapter 3 for the analysis of corrugated surfaces. The implementation of this rigorous code takes benefits from efficient techniques like the Conjugate Gradient - Fast Fourier Transform (CG-FFT)

and other acceleration techniques. This code is not only valid for standard corrugations, but also for planar versions. Simulated results are validated with commercial codes.

Next, the objective of chapter 4 is to extend this code to include the presence of a metal plate over the corrugated surfaces so that a SHWW with continuous corrugations can be analyzed. Moreover, some modifications of the code must be done for traveling-wave designs. Initial studies of the impedance of a radiating slot on a SHWW, as well as of slot mutual coupling are also shown. Finally, the optimization and design process of a complete design of a circularly polarized 2-D slot array on a SHWW using the implemented code is described in chapter 5.

Chapter 7 summarizes the main issues of this research work and the more relevant results.

Chapter 2

Quasi-TEM waveguides based on soft/hard surfaces: SHWWs

2.1 Introduction

For the purpose of devising a low-cost solution to feed a slot array, the first idea was to use an oversized rectangular waveguide, i.e., a waveguide that is much wider than the standard monomode ones. But now, some kind of material or periodic structure should be added in order to modify its propagation properties in such a way that this waveguide emulates the behavior of a collection of juxtaposed monomode rectangular waveguides. As seen in chapter 1, this guiding structure composed by a group of standard waveguides has been the traditional way to feed a slot array antenna, which requires control of the beam steering, however it involves some trouble in the manufacturing process that results in a high-cost product. This drawback is specially serious for frequencies over 30 GHz. Here, it has been tried to get almost the same behaviour, i.e. the transmission of physically spaced independent channels, but using a new guiding structure instead. This new structure should be more simple from the manufacturing point of view.

Oversized rectangular waveguides can support a multiplicity of modes, each one with its own propagation constant. By a proper combination of TE modes it is possible to generate a uniform quasi-TEM mode [119],[85], but its inherent dispersive behavior makes this quasi-TEM propagation very narrowband. As it is well-known, each Transverse Electric (TE) mode in a waveguide can be seen as the result of the interference between two waves impinging and reflect-

ing successively from both sidewalls with a particular angle of incidence [120]. Thus, it is easy to glimpse that if transverse currents are stopped so that only longitudinal currents can flow along the waveguide, then the two plane waves, which form each of the TE modes, are forced to change their propagation directions to the longitudinal direction of the waveguide (see Fig. 2.1). Thereby, only plane waves parallel to the longitudinal direction are allowed. In other words, any kind of propagation is suppressed except for the TEM-like one.
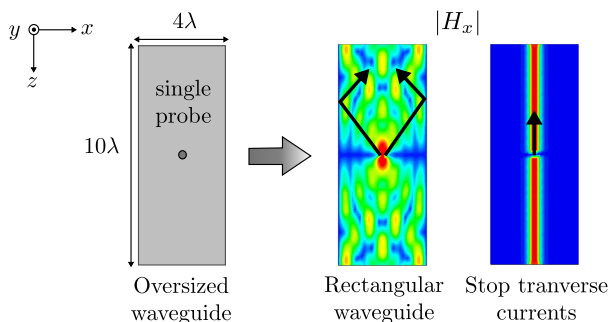
Figure 2.1: Top view of an oversized rectangular waveguide $(4\lambda \times 10\lambda)$ excited by a central single probe. Magnitude of the transverse x-component of the magnetic field inside this waveguide and also in case of transverse currents stopped.

The previous reasoning leads us to try to find out a waveguide in which propagation in the transverse direction is restrained while it is favored in the longitudinal direction. As a result, the Single Hard Wall Waveguide (SHWW) comes up [121]-[123]. The waveguide is comprised of a conducting upper face and a hard surface [101] as the lower face. The gap between these two faces, d, must not be higher than a quarter wavelength. The waveguide can be as many wavelengths wide as desired and its left and right sides can be left open since walls are not required to support the modes. Nevertheless, conducting sidewalls may be used, closing the waveguide to assure rigidity of the whole structure, as sketched in Fig. 2.2.

It is important to mention that ideal hard surfaces have already been shown to support pure TEM modes within cylindrical waveguides, regardless of its cross-section [124]. It is required that all the walls exhibit a hard boundary condition. For the purpose of making a slot array, however, the upper face must be a perfect conductor. It can be easily shown that forcing the waveguide height to be less than $\lambda/4$ the same behavior as in the ideal hard waveguides can be expected.

Single hard wall waveguides are a new type of waveguides that are able to propagate a plurality of degenerate independent quasi-TEM modes within the

Figure 2.2: Sketch of a Single Hard Wall Waveguide (SHWW).

same waveguide. Such local quasi-TEM waves in strip-type or corrugated hard surfaces were previously detected in Green's functions of planar hard surfaces [108],[102]. The local modes are believed to be present in all hard surfaces although they are normally not found by standard ways of deriving analytical modes based on separation of variables and assumptions of harmonic solutions. Each of these local modes would be excited by its own source (see Fig. 2.3). The waveguide does not require vertical walls to isolate these parallel modes from each other since they experience a strong transverse attenuation. This property makes the waveguide very attractive for applications over 30 GHz. In particular, those applications requiring multiple rectangular waveguides, like planar slot array antennas or slotted waveguide power amplifiers, can benefit from this type of waveguiding structure.

Figure 2.3: Four quasi-TEM waves excited by four probes within a SHWW.

As it can be seen in chapter 6 this idea has been improved so that the waves are no longer constrained to follow straight paths. The wave follows in the gap between a conducting ridge and the metallic upper face because the ridge is surrounded by artificial PMC surfaces on both sides, e.g., in the form of a bed of nails [125], i.e., a surface formed by metal pins standing on a ground plane.

The bed of nails is more effective than the grooves when the ridge supporting
the wave has to split, bend, make a corner, etc. Therefore, this other new type
of waveguide, so-called Ridge Gap Waveguide (RGW), is specially suitable to
make millimeter- and submillimeter-wave circuits and components. Studies
and designs about this new technology have been done to contribute to its
evolution. They are developed in chapter 6.

2.2   Propagation properties

Propagation properties of single hard wall waveguides have been numerically
studied through simulations provided by commercial software CST Microwave
Studio [126]. The results obtained are shown in this section together with
physical explanations to better understand their performance.

2.2.1   Physical theory

Propagation in hollow waveguides is generally described in terms of eigenmodes.
As it is well-known, the collection of eigenmodes that can propagate depends
on the waveguide cross-section and the working frequency. Let us refer to
the eigenmodes as global waves to emphasize the fact that these solutions of
Helmholtz's wave equation extend to the whole cross-section of the waveguide.
Let us now introduce local waves. Local waves, unlike global waves, would
be field solutions that propagate in a highly confined fashion, using mainly
a certain portion of the waveguide cross-section. Certainly these waves are
the result of a linear combination of eigenmodes and extend also to the whole
waveguide cross-section, but they are negligible for most part of it [127]. Con-
sequently, if we consider an electrically wide waveguide, several of these local
waves could share the same waveguide using different portions of the waveguide
cross-section without resorting to walls to keep them separated [128].

Single hard wall waveguides have such a particular property, thereby it is
possible to propagate multiple local waves within the same waveguide, as shown
in Fig. 2.3. These waves may show some degree of overlapping depending on
the spacing between them, but beyond a given separation they can be con-
sidered independent. To drive waves locally, the waveguide is formed in the
gap between a conducting plate and a hard surface. Artificially soft and hard
surfaces in electromagnetics are realized by corrugations or by metal strips
loading a grounded substrate [90] (see Fig. 2.4). Such surfaces make use of
surface resonances owing to the depths of the grooves, appearing for depths of
$h = \lambda/(4\sqrt{\varepsilon_{reff}})$, where ε_{reff} is the effective permittivity of the dielectric ma-
terial, which is ε_r for corrugated soft surfaces and $(\varepsilon_r - 1)$ for the hard surface.
In the soft case, corrugations are oriented transversely to the propagation and
they form so-called electric and magnetic current fences that stop the waves.

On the contrary, in the hard case, corrugations form electric and magnetic current lanes that support wave propagation. Actually, the corrugated surface used in this waveguide must act simultaneously as a hard surface in the direction of propagation and as a soft surface in the transverse direction. Yet the name given to the waveguide, single hard wall waveguide, put the emphasis on type of surface in the propagation direction.
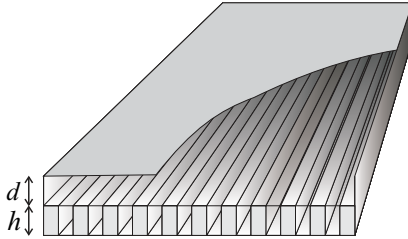
Figure 2.4: Single Hard Wall Waveguide realized by corrugations.

From the description above, it might be drawn that the conducting plate on top plays a secondary role, since all the guiding seems to be done by the corrugated surface. However, the truth is that the height of the gap left between the plate and the hard surface decisively contributes to keep waves bounded despite the absence of walls. Indeed the plate must be less than a quarter wavelength above the hard surface ($d < \lambda/4$) to achieve the desired effect. To better understand this effect we should look at the ideal model of a hard surface. Ideally, a hard surface can be seen as a grid of parallel strips where every second strip is a perfect electric conductor (PEC) and a perfect magnetic conductor (PMC), respectively [102]. It can be easily shown that by placing the metallic upper face not higher than a quarter wavelength from the hard surface, propagation in any direction other than the longitudinal one is stopped (see Appendix A). A PEC strip combined with the PEC plate above forms a transmission line. On the contrary, when a wave encounters a PEC on the upper plate and a PMC strip on the lower, it can barely trespass it for the given gap height. After crossing a few of these PEC/PMC strips in the transverse direction, the wave is deeply attenuated, producing a confined wave propagating only in the longitudinal direction as depicted in Fig. 2.5.

It is worth noticing that the corrugated surface should not be seen as a mere choke to the transverse propagation. If that were the case, $\lambda/4$ deep, air-filled grooves could have been used. The fact is that air-filled grooves do not work and the reason was stated above: the corrugated surface must be simultaneously soft and hard. In other words, the frequency band for which the corrugated surface functions in hard mode coincide with the soft mode band
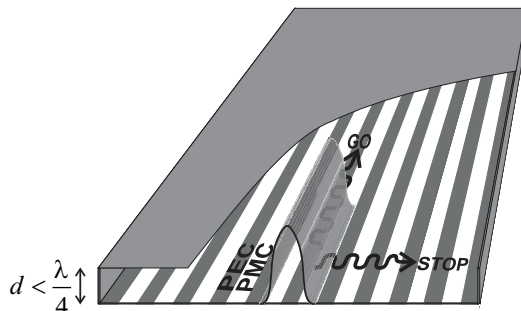
Figure 2.5: Ideal PEC/PMC interpretation of the hard surface and its overall
effect on the waves.

of the surface, and that only happens when grooves are filled with a dielectric
material.

Additional understanding comes from the observation of the dispersion dia-
gram obtained for the hard direction of a single hard wall waveguide (Fig. 2.6).
Assume a single hard wall waveguide having a corrugated surface whose groove
depth is $h = 2.95$ mm (around $\lambda/(4\sqrt{\varepsilon_r - 1})$ at 15 GHz), edge width $s = 1$ mm,
corrugation period $p = 3$ mm and dielectric permittivity $\varepsilon_r = 4$. The gap be-
tween the corrugated surface and the PEC plate on top is $d = 2$ mm. The
waveguide is 15 mm wide and sidewalls are PEC. Without loss of generality,
width is kept purposely small to relax computational effort. Fig. 2.6(b) shows
the dispersion diagram for the hard direction computed using CST. Light line
is also shown for reference. If now the PEC sidewalls are removed leaving the
waveguide open to the sides, the result is the dispersion diagram of Fig. 2.6(a).

A set of quasi-TEM eigenmodes can be seen in both diagrams. At the
intersection point, all the eigenmodes share the same phase velocity, and the
propagation constant is almost that one of light in vacuum. That point establi-
shes the hard condition. As explained above, local waves are obtained at this
point as a linear combination of these eigenmodes. Interestingly, when corru-
gations are air-filled there is no intersection point, as can be seen in Fig. 2.7.
Therefore eigenmodes have different phase velocities and the sought local wave
can not be obtained. On the other hand, higher permittivity values would lead
to steeper slopes for the quasi-TEM modes, which implies a narrower band-
width behavior. This can be observed in Fig. 2.6(c) and Fig. 2.6(d) for an
open waveguide and a closed waveguide by metal sidewalls, respectively. The
grooves are filled with a dielectric material of permittivity $\varepsilon_r = 10$, and groove
depth has changed to 1.68 mm to fulfill the hard condition $h = \lambda/(4\sqrt{\varepsilon_r - 1})$.
Simultaneously, a wide stopband exists in the soft direction around the fre-

(a) open, $\varepsilon_r = 4$

(b) closed by PEC sidewalls, $\varepsilon_r = 4$

(c) open, $\varepsilon_r = 10$

(d) closed by PEC sidewalls, $\varepsilon_r = 10$
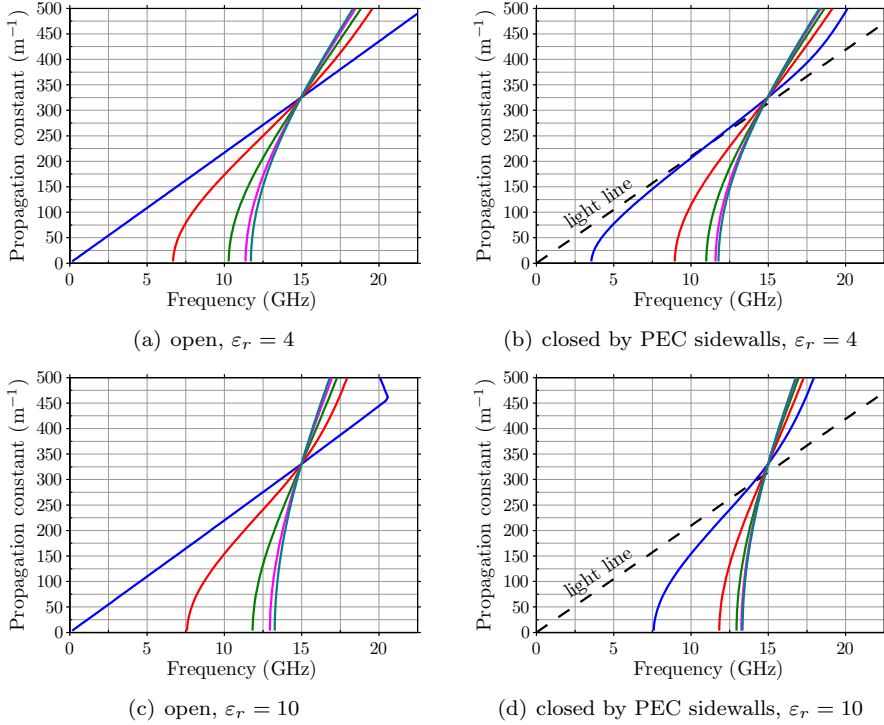
Figure 2.6: Dispersion diagrams in the hard direction of a SHWW with a groove filling material of dielectric permittivity ε_r.
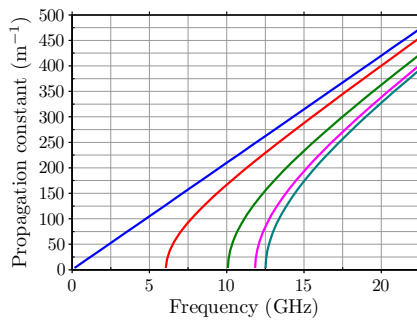
Figure 2.7: Dispersion diagram in the corrugations direction of a PPW with one wall made up of air-filled corrugations.
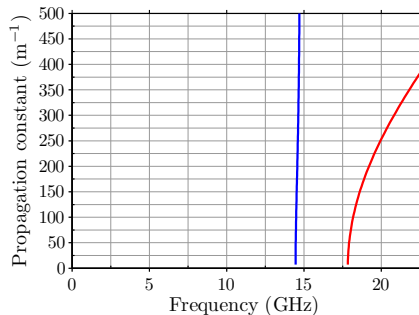
Figure 2.8: Dispersion diagram in the soft direction of a SHWW with a dielectric permittivity of the grooves of $\varepsilon_r = 4$.

quency where the hard condition holds, as Fig. 2.8 shows. Close to the hard frequency, we can see a line almost straight representing a mode of group velocity zero. Since this has no meaning it can be ignored. Next line represents a mode with cutoff frequency close to 18 GHz, so this frequency points out the end of the stopband in the soft direction. As a result, fields excited by a given local source are forced to propagate locally in the corrugations direction, which means that inner walls are not required to isolate waves. Thereby, the manufacturing process of planar slot array antennas can be greatly simplified if we can avoid the walls between the waveguides, which become increasingly thinner as we go above 30 GHz.

2.2.2 Numerical analysis

Some simulations have been carried out to illustrate the properties described above. We are interested in showing that a wave excited by a source at a given point stays confined as it propagates along the waveguide. We also show that these waves are quasi-TEM and can propagate side by side without intermingle. The simulated structure consists of a closed 4λ wide $\times$ 10λ long single hard wall waveguide having the same corrugation pattern (for a dielectric permittivity of the grooves $\varepsilon_r = 4$) as that used above to compute the dispersion diagram. Electric field is excited by coaxial probes and the working frequency is 15 GHz. To illustrate the difference of propagated fields excited by a single probe within a single hard wall waveguide and a rectangular waveguide of same dimensions, transverse and longitudinal components of the magnetic field are depicted in Fig. 2.9. As expected, a number of global modes are excited within an oversized rectangular waveguide, what causes a non-uniform field pattern in both, amplitude and phase, resulting in a highly dispersive and narrow-band transmission media. In the same way, these modes are excited within a single

hard wall waveguide, but on the contrary, they combine to produce a local quasi-TEM wave parallel to the longitudinal direction.

(a) $|H_x|$: transverse x-component

(b) $|H_z|$: longitudinal z-component
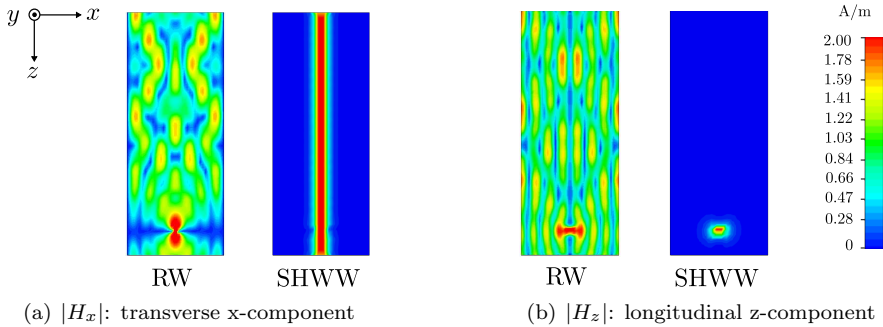
Figure 2.9: Magnitude of the transverse x- and longitudinal z-components of the magnetic field excited by a single probe of a Rectangular Waveguide (RW) and a Single Hard Wall Waveguide (SHWW) of $4\lambda \times 10\lambda$.

Fig. 2.10 shows both, transverse x- and longitudinal z-components of the magnetic field of the wave excited by a single probe within the SHWW. Fields are normalized to the maximum. Two transverse cuts along the waveguide are shown. As can be seen, field decays very rapidly to the sides and the longitudinal component is negligible, as expected for a quasi-TEM wave. Besides, the wave remains well-confined as it propagates.
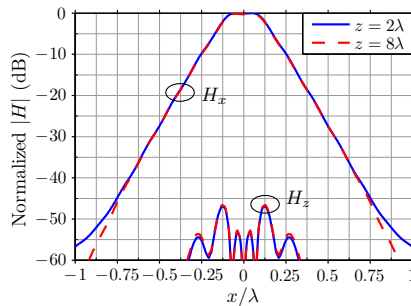
Figure 2.10: Magnetic field at the top metal plate of two transverse cuts along the waveguide produced by a single probe. $|H_x|$ and $|H_z|$ at two planes $z = 2\lambda$ and $z = 8\lambda$ from the source normalized to the maximum.

Next, the waves excited by an array of four probes are shown in Fig. 2.11. Probes are equispaced one wavelength. They are fed with uniform magnitude
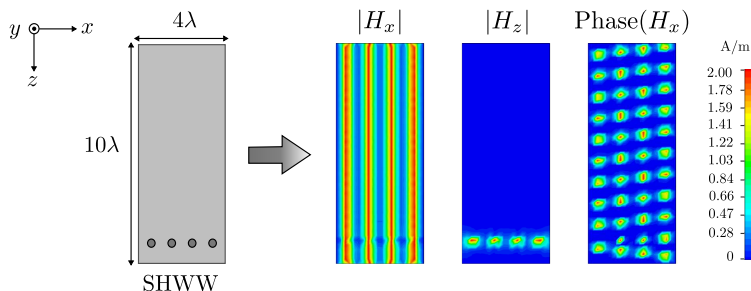
Figure 2.11: Magnitude and phase of the magnetic field on top of a SHWW fed by four probes with uniform amplitude and a linear phase of 45°.

(a) Magnitude of the transverse and longitudinal components

(b) Phase profile of the transverse component
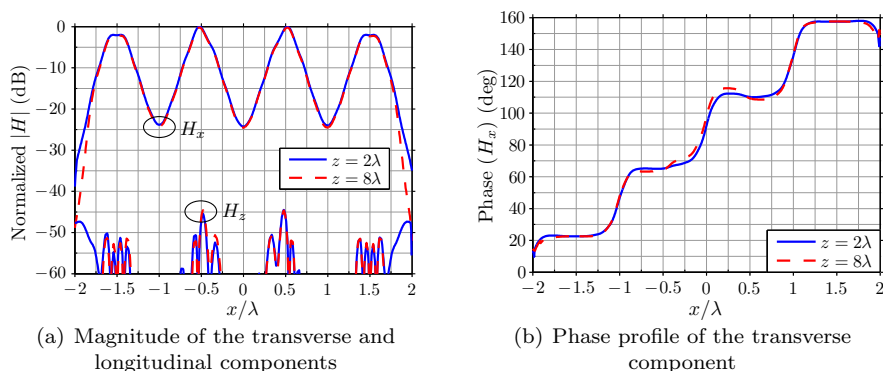
Figure 2.12: Magnetic field produced by four probes fed with uniform amplitude and linear phase of 45°. Field is obtained on the top metal plate at two planes $z = 2\lambda$ and $z = 8\lambda$ from the source.

and a linear phase of 45°. Magnitude and phase of the magnetic field throughout the waveguide can be seen.

Four local waves can be distinctly observed in Fig. 2.12(a), where the magnitude of the transverse component of the magnetic field is shown. Overlapping level is well below -20 dB even far from the source, therefore no relevant interference exist between them. A higher level would obviously be obtained for closer spacing but even so it is enough for slot array antennas. Fig. 2.12(b) highlights the stability and isolation of modes even with a linear phasefront. It is worth recalling that, unlike a parallel plate waveguide, where a linear phasefront would inevitably lead to linear amplitude patterns in transverse cuts, the single hard wall waveguide amplitude pattern seen in Fig. 2.12(a) remains uniform.

2.2.3 Waveguide characterization

Once propagation properties of single hard wall waveguides have been demonstrated to be those predicted, it is worth trying to characterize the waveguide in order to know how well the waveguide works for different realizations of hard surfaces. This characterization must allow us to determine the bandwidth or frequency band where the waveguide works as it is expected.

We propose to characterize the single hard wall waveguide by the performance of a local quasi-TEM wave [129]. Next, a single hard wall waveguide made up of dielectric-filled corrugations, like that shown in Fig. 2.13, is studied. For the sake of comparison the ideal model of a single hard wall waveguide is also analyzed. In this case, an ideal PEC/PMC strip grating is used as the hard surface.
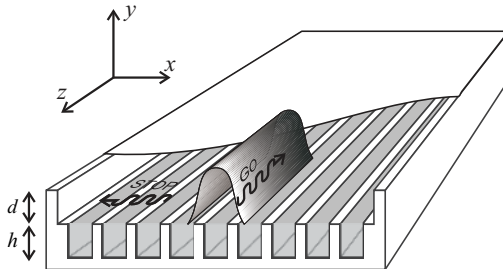
Figure 2.13: Single hard wall waveguide made up of dielectric-filled corrugations. A sketch of the quasi-TEM wave is also shown.

A single probe at the center of the waveguide is connected to the upper metal wall to excite a local quasi-TEM wave inside. This wave will be present at frequencies for which the soft and hard frequency bands coincide for the transverse and longitudinal propagation, respectively. In order to obtain such bands, the hard and soft properties of the corrugated surface are observed through the computation of couplings from the excitation probe to field probes in both the transverse soft x-direction and the longitudinal hard z-direction. The transverse component of the magnetic field $|H_x|$ is computed at a point 4.5λ away from the source in z-direction (hard line), and the longitudinal component of the magnetic field $|H_z|$ is computed at a point λ away from the source in x-direction (soft line), as sketched in Fig. 2.14. The objective is then to maximize the coupling (relative $|H_x|$) in the hard direction and minimize the coupling (relative $|H_z|$) in the soft direction over the same frequency range. It may also be useful to establish a lower hard threshold and an upper soft threshold that represents a certain quality of such a waveguide. In order to establish such thresholds, we computed $|H_x|$ and $|H_z|$ at the two specified locations and

normalized the values to the computed $|H_x|$ for the ideal case when the hard surface consists of a PEC/PMC strip grating. In this way, a proper comparison of different hard surface realizations and dimensions can be carried out. For the simulations the waveguide was terminated by an absorbing material.
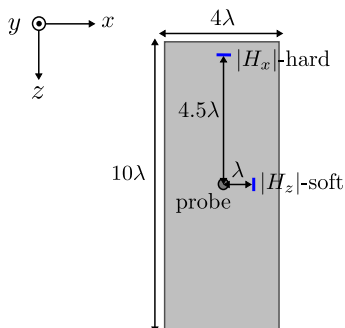
Figure 2.14: Scheme of the probe setup to obtain soft and hard field values.

To sum up, the procedure of characterizing oversized waveguides with single hard wall for different realizations of the hard surface lies in obtaining soft and hard field values and normalize them to those obtained for an ideal PEC/PMC strip grating excited with the same probe and having an overlying PEC surface at the same height.

Soft and hard field values of an ideal PEC/PMC single hard wall waveguide are shown in Fig. 2.15. For a waveguide height approaching to $\lambda/4$, e.g. $d = 5$ mm at 15 GHz, soft and hard field values are almost the same, what means that PEC/PMC strip gratings are not stopping transverse waves anymore.
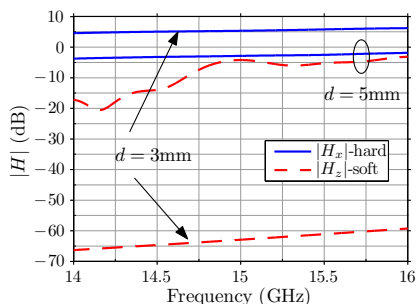
Figure 2.15: Soft and hard frequency lines of an ideal PEC/PMC single hard wall waveguide for waveguide heights of $d = 3$ and 5 mm.

(a) Soft and hard frequency lines

(b) $|H_x|$ and $|H_z|$ at different frequencies
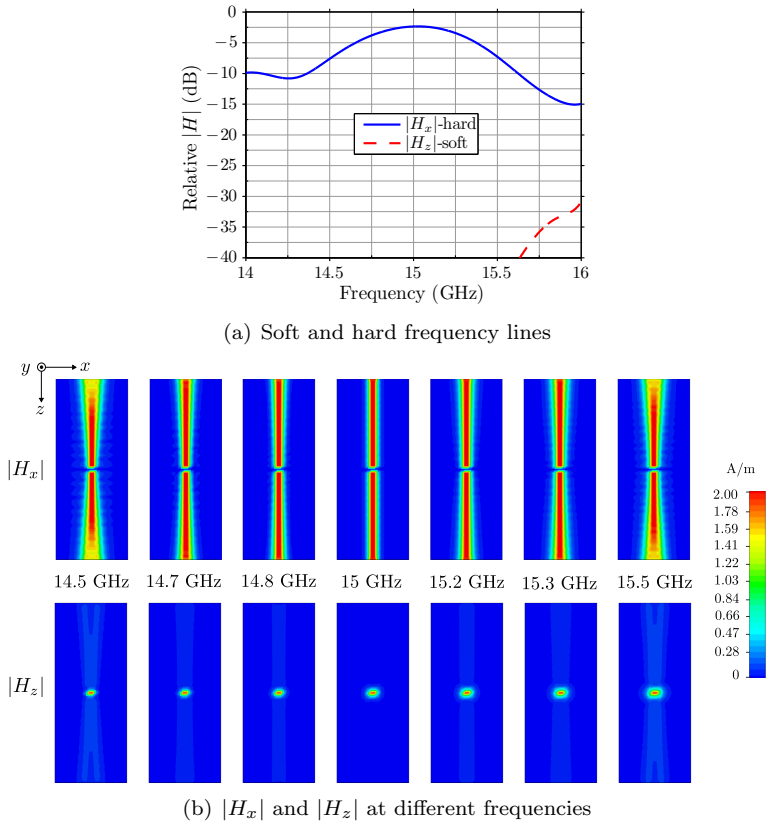
Figure 2.16: SHWW characterization. Soft and hard frequency lines and field patterns for $d = 2$ mm and $\varepsilon_r = 10$.

Now, a single hard wall waveguide with a dielectric-filled corrugated surface as the hard surface is analyzed. Dimensions of the hard surface are those of the previous section. Fig. 2.16 shows simulated results for a waveguide height $d = 2$ mm and dielectric permittivity $\varepsilon_r = 10$. Field patterns $|H_x|$ and $|H_z|$ throughout the waveguide at different frequencies are shown in Fig. 2.16(b). We can see that there is a frequency band where the wave remains well-confined along propagation direction. Beyond this band (from 14.7 GHz to 15.3 GHz, 600 MHz roughly for this example) dispersion of the wave is increasingly higher as frequency goes away the band. If now we look at Fig. 2.16(a), where soft and hard field values are depicted, it is observed that for such frequency band the hard line is above -5 dB approximately. Depending on the desired quality

(a) Soft and hard frequency lines

(b) $|H_x|$ and $|H_z|$ at different frequencies
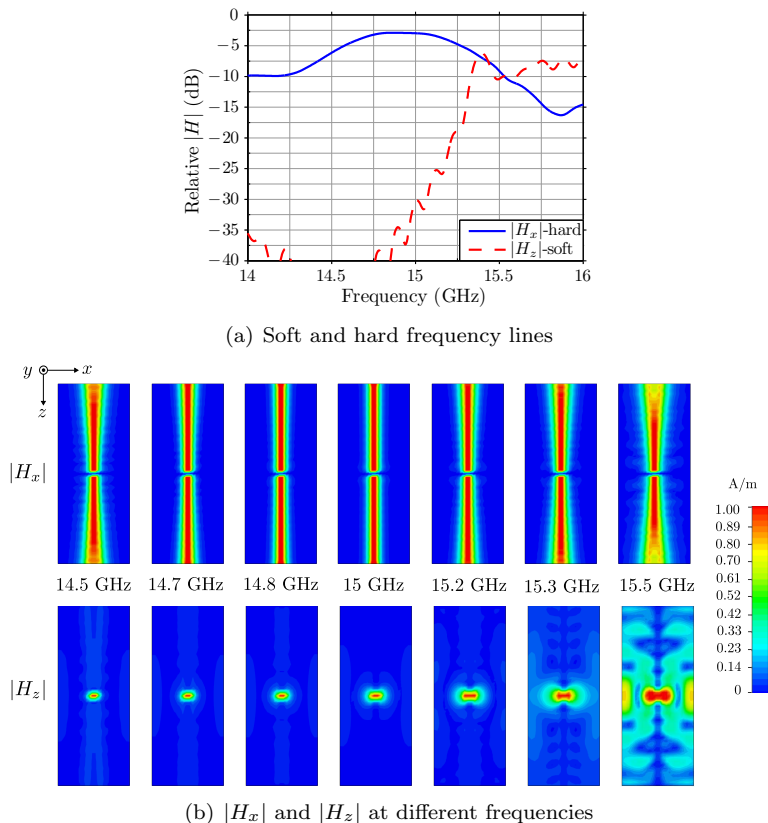
Figure 2.17: SHWW characterization. Soft and hard frequency lines and field patterns for $d = 3$ mm and $\varepsilon_r = 10$.

we can deduce a lower hard threshold, so that the hard frequency band is that one for which the hard line is above this threshold. A good lower hard threshold value may be then -5 dB. Same threshold can also be deduced from Fig. 2.17 and Fig. 2.18 for $d = 3$ mm and $\varepsilon_r = 10$, and $d = 2$ mm and $\varepsilon_r = 4$, respectively. Looking at Fig. 2.16(a) and Fig. 2.17(a) we can see that the hard band does not change with waveguide height. Just a small shift of the hard band to lower frequencies can be appreciated when waveguide height increases, since now, following the previous criteria of -5 dB for the hard line, the band spans 600 MHz from 14.6 GHz to 15.2 GHz. Nevertheless, a wider band is observed for lower permittivity values, as can be seen in Fig. 2.18(a). Following the previous criteria, a hard band of 1400 MHz (from 14.3 GHz to

(a) Soft and hard frequency lines

(b) $|H_x|$ and $|H_z|$ at different frequencies
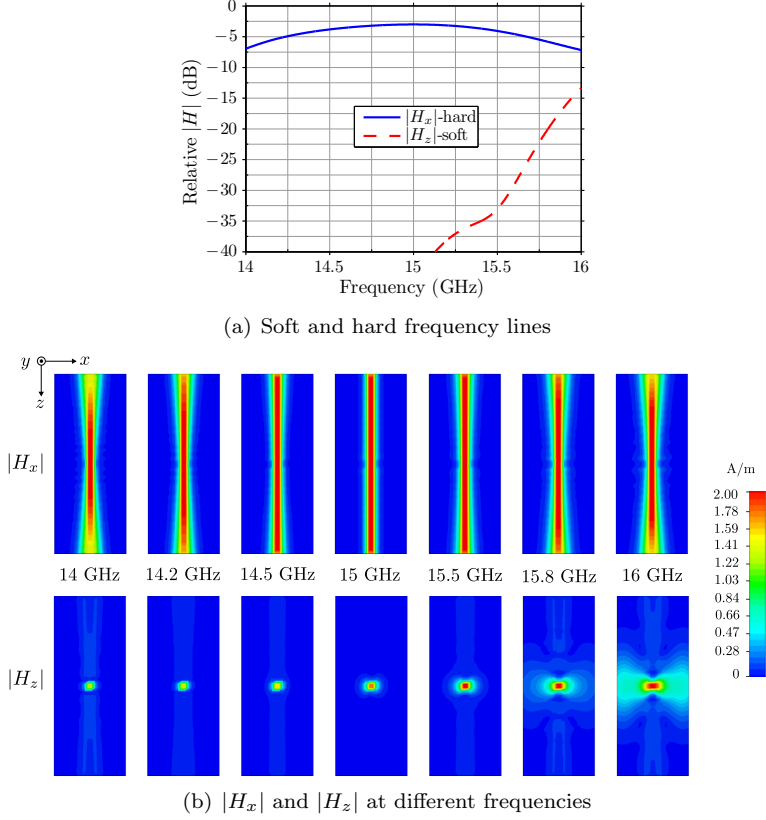
Figure 2.18: SHWW characterization. Soft and hard frequency lines and field patterns for $d = 2$ mm and $\varepsilon_r = 4$.

15.7 GHz) is obtained for $\varepsilon_r = 4$ and groove depth altered to meet the hard condition.

It is clear from the results that the soft frequency band is wider than the hard band, thus normally the bandwidth is determined by the hard band. On the one hand, the parameter that determines the hard band is the dielectric permittivity of the groove-filling material. The hard band is wider for lower permittivity values, up to one permittivity value below which the waveguide loose its hard properties. It has been proved that for $\varepsilon_r < 4$ this waveguide cannot propagate local waves. On the other hand, we can see that the lower limit of the soft band is much below the hard band, so its value is not relevant for us. The lower limit is imposed by the performance of the corrugated surface

27

as a soft surface, i.e. as a barrier to the transverse propagation, which requires $\lambda/4 < h < \lambda/2$.

However, the upper limit of the soft band is conditioned by the waveguide height, since for waveguide heights approaching to $\lambda/4$ the waveguide has not soft properties anymore and longitudinal components of the fields within the waveguide start to appear. This effect was shown in Fig. 2.15 for the ideal case, and it can also be seen for a dielectric-filled corrugated hard surface in Fig. 2.17. As expected, given a certain waveguide height, the soft band is wider for the ideal hard surface than for the real one. So, even for waveguide heights below $\lambda/4$ a realization of a single hard wall waveguide with dielectric-filled corrugations could not work properly, as it would not be blocking transverse waves. Thus, for practical realizations it is important to check whether the waveguide height is low enough to stop transverse currents.

In the same way as was done for the hard direction, it is convenient to establish a soft threshold. It is visible from Fig. 2.17 that the longitudinal z-component of the magnetic field cannot be neglected for soft field values over -15 dB. Therefore, a good upper soft threshold should be -15 dB.

A way of characterizing single hard wall waveguides has been introduced. As a result of such characterization it can be concluded that the single hard wall waveguide is a narrow band device, but it shows an acceptable bandwidth and can be controlled by the permittivity of the groove-filling material. This characterization is fitting to compare different realizations of the hard surface with respect to their bandwidths and quality as well as to carry out optimizations.

2.3 Practical realization and experimental results

This section reports an experimental study of this waveguiding structure. A practical realization is described, manufactured and measured to show the remarkable properties observed previously in simulations [130].

As it is stated in [90], longitudinal grooves must be filled with a dielectric material of permittivity ε_r, in order to work as a hard surface, and the groove depth should be approximately $h = \lambda/4\sqrt{\varepsilon_r - 1}$ at the working frequency.

From a manufacturing point of view, it is easier to construct the edges between corrugations by perforating a copper-clad laminate with a series of via-holes than machining a corrugated surface and filling the grooves up with the desired material (see Fig. 2.19). This is the procedure followed here to construct the hard surface at the expense of experiencing some deviation from the expected theoretical performance of a corrugated hard surface.

Fig. 2.20 shows the hard surface made out of metallic strips etched on a copper-clad laminate, and via-holes connecting the strips to the ground plane.

Figure 2.19: Drawing of the hard surface consisting of narrow strips and via-holes connecting the strips to the ground plane.

A detail of the hard surface is also shown in the picture where the coaxial probe used to feed the waveguide can also be seen. The probe is placed a quarter wavelength away from the shortcircuit.
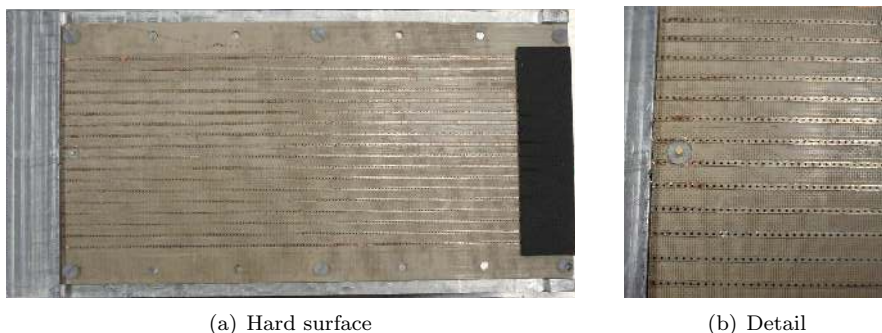
(a) Hard surface

(b) Detail

Figure 2.20: Hard surface made out of etched copper strips and plated via-holes on a PCB.

The hard surface has been designed and optimized through simulations [126] performed on a corrugated surface having continuous grooves instead of vias to relax the computational cost. Then, the width and period of the ridges of the corrugated surface are used to define the width and period of the strips. Vias period is selected out of a trade-off between good electric performance and manufacturing limitations. The strips are in our case chosen so narrow that there is no effect on their performance due to their width. See [76].

The SHWW is chosen to operate with 15 GHz as the center frequency. The substrate is a 1.5 mm thick Arlon AD1000 laminate with $\varepsilon_r = 10.7$ and $\tan \delta = 0.0023$. Eighteen 1 mm wide, 180 mm long copper strips have been etched on the PCB. The strip period is 4 mm. The via-holes are 0.4 mm in

diameter and are equispaced along each strip by 1.2 mm. The strips were made using a milling machine, and the vias were plated with a conductive polymer. As a rule of thumb, it can be stated that any combination of strip width and period will produce the expected behavior as long as both of these parameters are kept electrically small, i.e., with a period smaller than $\lambda/2$. Nevertheless, the most important parameters to be observed are the groove depth, h, and the gap height, d, as discussed.

Simulations showed a narrow quasi-TEM wave propagating along the longitudinal direction of the waveguide. Now we are interested in measuring two figures of merit: given a source and a range of frequency, the first figure is the comparison between the electric field in two locations. One measurement is done at a point at a certain distance in the longitudinal direction (known also as hard direction), and the other is performed at a given point in the transverse direction, the so-called soft direction. This comparison will give us an idea of the waveguide bandwidth. The second figure is the electric field pattern measured in the waveguide section at a given frequency. Cuts measured at several sections along the waveguide will show divergence of the local wave.

A scheme of the experimental setup is shown in Fig. 2.21. As can be seen, the hard surface is facing down and the conducting face is much larger than the hard surface. Each of the two probes is connected through a different face to make field sampling easier, just by sliding the hard surface above the plane, which has been conveniently ruled with a grid of horizontal and vertical lines.
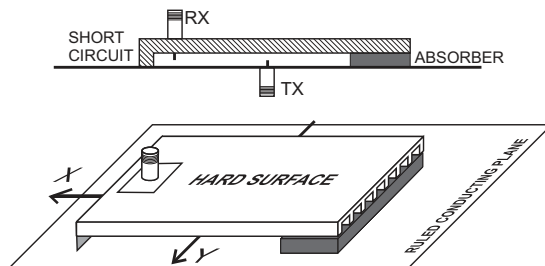
Figure 2.21: Scheme of the experimental setup.

The hard surface is 2 mm above the conducting surface. The waveguide is shortcircuited at 5 mm from the receiving probe and terminated with an absorbing material. Both, left and right sides are left open. Probes are 1.5 mm long. Even though such short probes are not well matched for the given range of frequencies, it does not represent a problem since we are only interested in measuring S_{21} parameter at this stage. Yet, results will be normalized with respect to the mismatch factors $1 - |S_{11}|^2$ and $1 - |S_{22}|^2$.

Assume the transmitting probe is fixed in position (0,0). For the first figure of merit we measure the S_{21} parameter 160 mm away in the hard direction, location (160,0) in Fig. 2.21, and the S_{21} parameter 20 mm away in the soft direction, location (0,20) in the same figure. Looking at Fig. 2.22, the band over which the SHWW focuses the field in the hard direction is given by those frequencies where measured values are not lower than -3 dB in the hard direction and, at the same time, are lower than -15 dB in the soft direction. For this case it goes from 14.8 to 15.4 GHz. A wider bandwidth can be achieved using a lower permittivity in the corrugations.
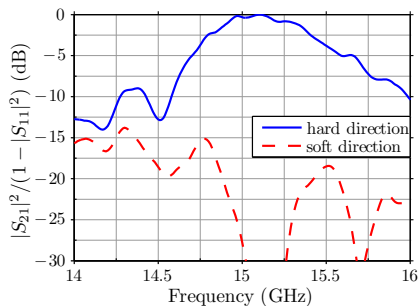
Figure 2.22: S_{21} parameter measured in the hard and soft directions as a function of frequency. Data is normalized to the S_{11} for each frequency.
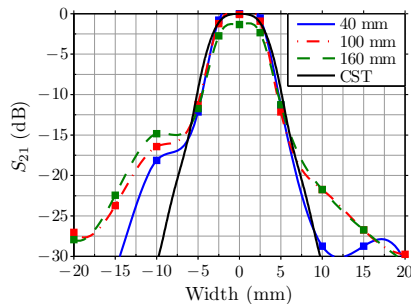
Figure 2.23: S_{21} parameter measured for three transverse cuts taken at $x = 40, 100, 160$ mm from the source. A CST simulation is shown for reference.

Let us consider now the field pattern measured at some transverse cuts within the waveguide. The working frequency is selected to be 15 GHz. The transmitting probe is again fixed in position (0,0). Firstly, to select the cuts to be measured, we slide the RX probe away from the TX probe along the

hard direction, $y = 0$ line. In doing so, a 4 dB VSWR is observed despite the presence of an absorber. Consequently, the cuts are done at the maxima of this standing wave. Then, the receiving probe is slid along cuts of fixed x.

Fig. 2.23 shows the patterns obtained for three cuts taken at $x = 40, 100, 160$ mm respectively. Samples were taken at the points shown with symbols. A spline interpolation has been added for the sake of clarity. The field obtained from simulations on a SHWW whose hard surface use continuous grooves is also shown for reference. As can be seen, the pattern is very well preserved with distance. A 1.3 dB attenuation can be observed in the 160 mm (8λ) cut. These losses may be attributed to a inexact location of the probe to measure a maximum of the standing wave. The beam is certainly very narrow: levels are more than 10 dB below the maximum 5 mm ($\lambda/4$) away from it. Asymmetries can also be seen for values lower than -13 dB. All values are normalized with respect to the first cut maximum.

Chapter 3

Analysis of corrugated surfaces

3.1 Introduction

Corrugated surfaces have been used for decades to design antennas with low cross polarization or chokes to reduce coupling. More recently, these structures got renewed interest due to its ability to control propagation in a desired way. This is the case of artificially soft/hard surfaces [90]. These are corrugated surfaces filled with a dielectric material, which facilitate propagation along the longitudinal direction and at the same time stop propagation in the direction transverse to the corrugation for a given frequency band. Among the novel applications of such a property, we may find cloaking [117], quasi-TEM waveguides [124] or oversized waveguides capable of propagating several independent quasi-TEM beams simultaneously [122].

Accurate and efficient modeling of corrugated surfaces is desirable to establish their reflection properties and bandwidth. However, brute-force computation of a large, densely-corrugated, dielectric-filled structure is a computationally costly task. Over the years, a number of approximate models have been proposed. An analytical approach came through the so-called Asymptotic Corrugated Boundary Condition (ACBC) [131], which gives good results for a corrugation period much smaller than the wavelength [132]. Recently, a more accurate approach was proposed exploiting the Impedance Boundary Condition (IBC) associated with the corrugated surface and solving the resulting integral equation by the method of moments for 2-D structures [133] and for the 3-D ones [134].

The use of an IBC to approximate a corrugated surface is in fact very intuitive and appealing. One replaces a complex grooved body by a surface, thus reducing considerably the computational cost. Furthermore the IBC method is easy to implement and its results are very satisfactory, as shown in the references cited. On the other hand, as explained in [134], the IBC shows numerical limitations, which imposes restrictions on the working geometrical properties of the corrugation, i.e., the width of the grooves must be small compared to wavelength, the walls of the grooves must be smaller than the width of the grooves themselves and the height of the grooves must be close to the resonant case.

Yet, there exists an alternative approach that seems to have been overlooked. The technique does not show any of the restrictions mentioned above. We are referring to the generalized network formulation for aperture problems. It applies to any two regions isolated except for the coupling through the aperture. In our case these two regions are the free-space region and the groove. In an already classic paper [135], Harrington describes how an aperture problem can be given in terms of the method of moments. The aperture characteristics are expressed in terms of two independent admittances, one for each region. Consequently, the groove effect can be characterized accurately, regardless of its particular shape, using any numerical method capable of giving the interior admittance. Furthermore, the grooves' walls can be any width. In fact, new realizations of hard/soft surfaces [102] like the L- and T-shaped ones, which are shown in Fig. 3.1, are now perfectly workable with this approach. Moreover, the standard U-shaped corrugations can be seen just as a particular case of those.
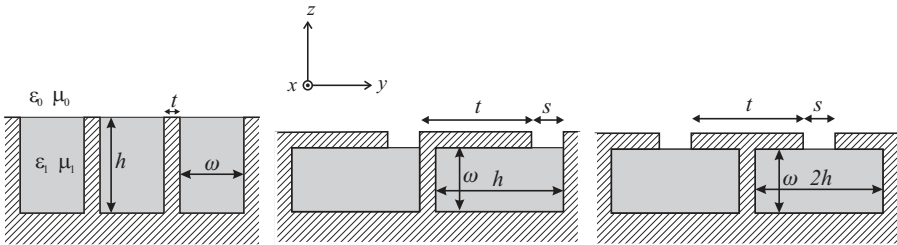
Figure 3.1: Different types of artificial soft and hard surfaces: standard U-shaped corrugations, inverted-L corrugations, and T-type corrugations.

We show the accuracy, versatility and limitations of the aperture approach for corrugated surfaces. Firstly, in section 3.2 the aperture integral equation (AIE) and its method of moments realization are briefly described emphasizing the particularities of this problem. Next in section 3.3 some results are shown

for various types of corrugated surfaces. The results are compared to those obtained by a commercial software, CST Microwave Studio.

3.2   MoM analysis based on the AIE

The AIE is the standard procedure to deal with apertures on conducting surfaces. The basic theory can be found in textbooks [136] and essentially establishes an integral equation by formulating two equivalent problems for regions a and b in Fig. 3.2. These two problems become independent as the aperture is closed by a conducting surface. Continuity of tangential electric fields in the aperture is assured by imposing opposite equivalent magnetic currents on both sides of the closed aperture, while the enforcement of the continuity condition of tangential magnetic fields yields the operator equation

$$H_{tan}^a(M) + H_{tan}^{inc} = H_{tan}^b(-M). \tag{3.1}$$

whose solution determines the unknown equivalent magnetic current M.
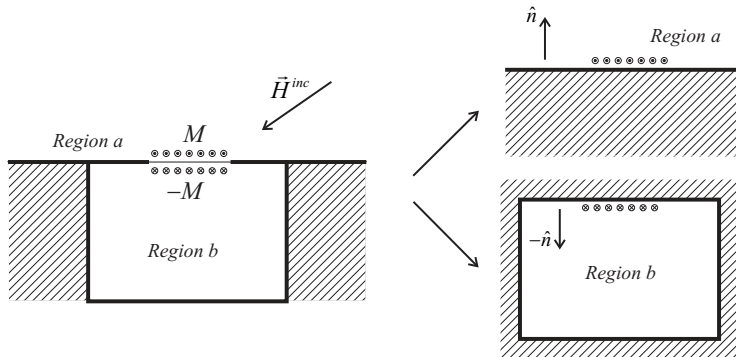
Figure 3.2: Side view of a groove in a corrugated surface and equivalent problems for regions a and b.

The drawing in Fig. 3.3 outlines a corrugated surface made up of a discrete number of finite T-type grooves. An approximate solution for M in (3.1) can be obtained using MoM. For this particular problem, rooftop functions are a good choice as expansion functions, M_n. They are oriented to allow magnetic current flow only along the corrugation's aperture, which is considered electrically thin. Therefore only one row of basis functions per groove is considered enough for scattering purposes. Magnetic currents oriented transverse to the corrugation are assumed negligible. Rooftop functions are also selected as testing functions, W_n, leading to the matrix equation
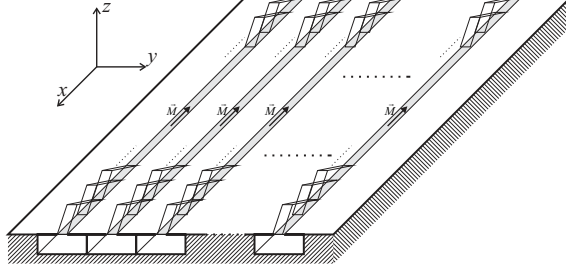
Figure 3.3: Outline of a corrugated surface made up of T-type grooves. The drawing also shows the rooftop basis functions oriented in accordance to the magnetic current vector.

$$[Y^a + Y^b]\bar{V} = \bar{I} \qquad (3.2)$$

where $[Y^a] = [\langle W_m, H^a_{tan}(M_n)\rangle]_{N \times N}$ is the external admittance matrix, $[Y^b] = [\langle W_m, H^b_{tan}(M_n)\rangle]_{N \times N}$ is the internal one and $\bar{I} = -[\langle W_m, H^{inc}_{tan}\rangle]_{N \times 1}$ the excitation vector.

As sketched in Fig. 3.2 the external problem, region a, involves a finite set of magnetic currents on an infinite conducting plane. Hence, the entries of $[Y^a]$ can be readily obtained after applying image theory and then using the free-space Green's function. Looking at Fig. 3.3 it is easy to realize that $[Y^a]$ will be a block-Toeplitz matrix. This property will be used later to accelerate computations. The use of image theory, quite common when dealing with magnetic currents on conducting planes, introduces a departure from the geometry of the actual problem since now the finite corrugated surface turns out to be surrounded by an infinite conducting plane. This will have an effect on the accuracy of the results. Indeed the field scattered at grazing angles will differ from the real one.

The equivalence of each groove, as represented by region b in Fig. 3.2 may be seen as a waveguide, being x its longitudinal axis, as shown in Fig. 3.3. Given the usual dimensions of the corrugations, such waveguides will be too small to allow any propagation in them. This means that mutual admittances between basis functions in the same groove will decay very rapidly with distance. Fig. 3.4 illustrates this behavior for the mutual admittances in one of the cases that will be studied later. Y^b_{21} is shown relative to Y^b_{11} to help visualization. The case is an U-shaped corrugation filled with a dielectric material of $\varepsilon_r = 10$, being $h = \lambda/(4\sqrt{\varepsilon_r - 1})$ and $\omega = 0.02\lambda$ at 10 GHz. The discretization cell is $0.02\lambda \times 0.05\lambda$.

In addition, mutual admittances between basis functions in different grooves will be clearly zero. Therefore, the entries of $[Y^b]$ are either zero or negligible
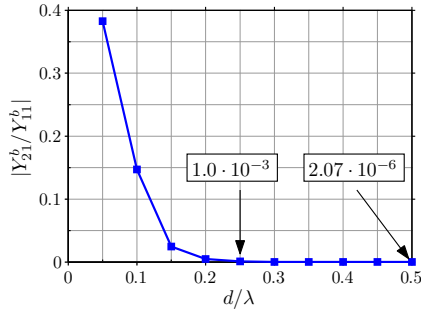
Figure 3.4: Y_{21}^b relative to Y_{11}^b versus electric distance between basis functions for a U-shaped corrugation filled with a dielectric material of $\varepsilon_r = 10$ with $h = \lambda/(4\sqrt{\varepsilon_r - 1})$ and width $\omega = 0.02\lambda$ at 10 GHz. The values are calculated at discrete steps of 0.05λ.

except for the main diagonal, holding the self-terms and a few diagonals below and above it, which contain the closest interactions, not further than half-wavelength away in the groove. All these entries are obviously reactive.

Consider now a $6\lambda \times 6\lambda$ hard surface made up of the U-shaped corrugations with dimensions mentioned above. The bistatic scattered field is depicted in Fig. 3.5 to show the convergence of the method employed depending on the internal interactions considered within a distance d away in the groove. As it can be seen the method has already converged when the interactions considered are within a quarter wavelength. Taking internal interactions for higher distances has no effect on the results.
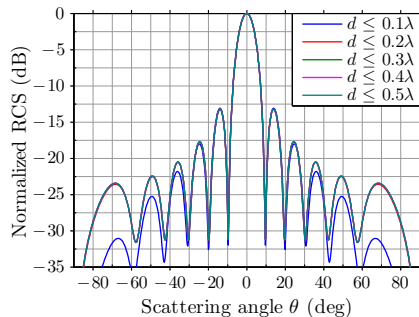
Figure 3.5: Normalized RCS for a $6\lambda \times 6\lambda$ U-shaped corrugated surface depending on the internal interactions Y_{ij}^b considered within a distance d away in the groove.

37

The computation of internal self- and mutual admittances is carried out using two slightly different approaches for the L- and T-type corrugations on the one hand and the standard U-shaped corrugations on the other.

3.2.1 Computation of internal admittances y_{ij}^b in L- and T-shaped corrugations

Let us first consider the computation of the self term, y_{11}^b. A single basis function can be regarded as a short magnetic dipole longitudinally oriented within the waveguide. Initially, image theory is applied with respect to the side walls of the waveguide giving rise to an equivalent problem consisting of an infinite series of parallel magnetic dipoles within a parallel-plate waveguide (see Fig. 3.6). Now the computation of the total magnetic field at the location of the real magnetic dipole will make use of the parallel plate Green's function. The sum of the infinite series of fields

$$y_{11}^b = Y_0 + \sum_{i=-\infty}^{\infty} Y_i \qquad (3.3)$$

take advantage of Shank's transformation [137] to accelerate convergence. Indeed, about 15 images are needed to assure good accuracy.

In general this procedure can not assure proper convergence when computing mutual admittances, y_{1n}^b, unless basis functions are electrically very close together in the longitudinal direction. Therefore the Green's function of a rectangular waveguide would have to be used instead. Fortunately, in our case the rectangular waveguide is below cutoff and mutual admittances decay very rapidly with distance along the waveguide. Significant mutual admittances are in the range of half-wavelength, where the computation based on image theory can still be used.
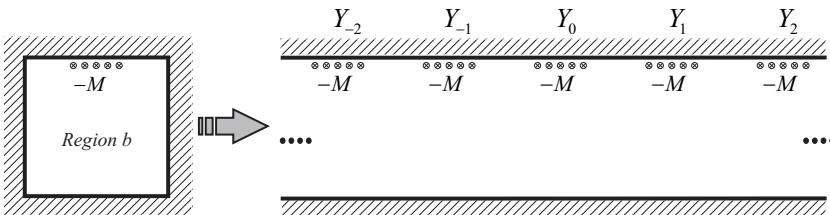
Figure 3.6: Equivalent problem after applying image theory for the computation of internal admittances y_{ij}^b for L- and T-shaped corrugations.

3.2.2 Computation of internal admittances y_{ij}^b in U-shaped corrugations

When a U-shaped corrugation is closed with a conducting plane following the AIE method, the magnetic current imposed within covers now the whole top face of the resultant rectangular waveguide. Proceeding like in section 3.2.1 will yield an infinite series of contiguous rooftop basis functions. If we attempt to sum the series we will find it hardly convergent this time due to the extreme proximity between the images. On the other hand, all these basis functions together can alternatively be seen as a continuous strip extending to infinite. Therefore now the equivalent of a magnetic short dipole within a waveguide is an infinite strip showing uniform distribution in the $\hat{y}$ direction and a triangular distribution in the $\hat{x}$ direction (see Fig. 3.3). Now, since the strip is within a parallel plate waveguide, in order to compute the magnetic field at the location of the actual basis function, it is most appropriate to apply image theory again, this time with respect to the top and bottom faces of the equivalent parallel plate waveguide. Then, as shown in Fig. 3.7, an infinite series of infinite strips is obtained, whose contribution to the desired magnetic field comes from the sum of the series of fields created by them following the expression (3.3), which now involves the use of the 2-D Green's function for free-space. Shank's transformation is used once again to accelerate computations.
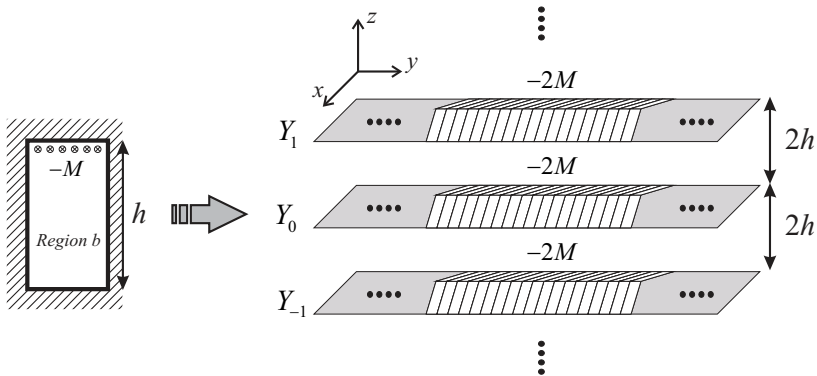
Figure 3.7: Equivalent problem after applying image theory for the computation of internal admittances y_{ij}^b for U-shaped corrugations.

Once the matrix equation is obtained, it can be solved for the magnetic currents using Gaussian elimination. Nevertheless, electrically large corrugated surfaces may involve thousands of unknowns, rendering the problem unsolvable using such a direct method. A solver combining the Conjugate Gradient method and the Fast Fourier Transform algorithm (CG-FFT) [138] has been

used instead to analyze large realistic problems. Corrugated surfaces are perfect candidates to be computed using the CG-FFT algorithm as they produce block-Toeplitz matrices naturally, without resorting to any type of approximation in the geometry to force such structure in the matrix.

3.3 Software validity demonstration

Several cases have been simulated and compared with commercial software CST Microwave Studio to establish the accuracy and limitations of this approach. At the same time these cases will give us valuable information on the differences among the various types of corrugated surfaces shown in Fig. 3.1.

First of all we consider the same test cases as in [134] where the IBC method is used. The object is a standard corrugated surface of size $3\lambda \times 3\lambda$. The grooves are not filled with dielectric material. The incident field is $\hat{y}$-polarized and the frequency is $f = 1$ GHz. Figs. 3.8(a) and 3.8(b) show the normalized bistatic scattered field for normal ($\theta = 0°$) and oblique incidence ($\theta = 40°$ with $\phi = 0°$) respectively. In the first case, the corrugation height is $h = 0.23\lambda$ and width $\omega = 0.05\lambda$ while for the second case $h = 0.19\lambda$ and $\omega = 0.08\lambda$. Very good agreement is observed with respect to the reference software for both cases. All fields shown are normalized with respect to their own maximum.

The differences seen for angles approaching $90°$ are due to the implicit presence of an infinite conducting surface surrounding the corrugated surface. This is the main deficiency of a method like this, based on the use of equivalent magnetic currents. Therefore horizontal components of the scattered field must vanish at grazing angles to accommodate the boundary conditions.

(a) $h = 0.23\lambda$, $w = 0.05\lambda$ (b) $h = 0.19\lambda$, $w = 0.08\lambda$
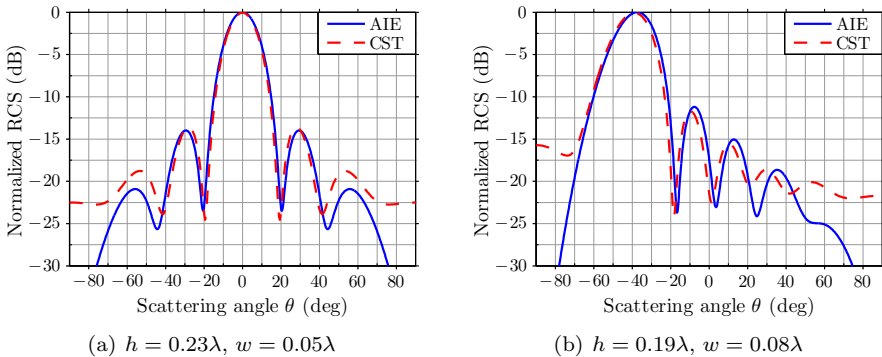
Figure 3.8: Normalized RCS of a $3\lambda \times 3\lambda$ U-shaped corrugated surface: (a) for normal incidence $\theta = 0°$, (b) for oblique incidence $\theta = 40°$, $\phi = 0°$.

It is clear now that the reflection properties of the surface are associated with the admittance shown by the grooves, $[Y^b]$. Therefore, it is expected that those surfaces whose corrugations show the same internal admittance will exhibit similar reflection characteristics, regardless of its shape. Fig. 3.9 shows the self-term of the internal admittance matrix for the three types of corrugations depicted in Fig. 3.1 as a function of its depth, h. Corrugations are filled with a dielectric material of $\varepsilon_r = 10$, the width is $\omega = 0.6$ mm, and the aperture s is also 0.6 mm for the L- and T-type corrugations. As expected, the three show similar admittances.
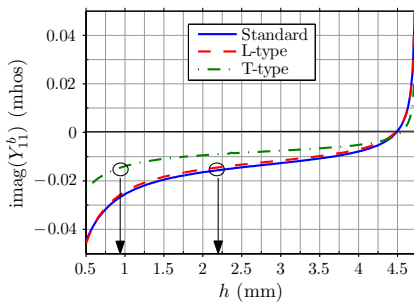
Figure 3.9: Self-term of the internal admittance matrix as a function of h for the three types of corrugations considered. The frequency is 10 GHz. Corrugations are filled with a dielectric material of $\varepsilon_r = 10$, the width is $\omega = 0.6$ mm, and the aperture s is also 0.6 mm for the L- and T-type corrugations.

Now, let us compare the L- and T-type corrugations with the standard corrugated surface when the latter is tuned to work as a hard surface at grazing incidence, $h = \lambda/(4\sqrt{\varepsilon_r - 1})$. From Fig. 3.9 it is expected that closely similar backscattered fields should be obtained if the internal admittances of the three types of corrugations are similar. In the example considered, the corrugated surface is $6\lambda \times 6\lambda$ and the corrugations are filled with a dielectric material of $\varepsilon_r = 10$. The frequency is $f = 10$ GHz and h is 2.5 mm. Therefore, the L-type corrugation should have an h value of 2.2 mm while for the T-type, this value should be around 0.95 mm for their Y_{11}^b to be like that of a standard corrugation. Notice however that the whole width of the T-type grooves is twice that value (see Fig. 3.1).

Figs. 3.10(a) and 3.10(b) show the normalized bistatic scattered field for normal ($\theta = 0°$) and oblique incidence ($\theta = 40°$ with $\phi = 0°$) respectively, for the three types of corrugated surfaces. As can be seen, L- and T-type corrugations produce very similar results. This is perfectly reasonable considering that the internal admittances are the same and the conducting surface between

(a) normal incidence $\theta = 0°$ (b) oblique incidence $\theta = 40°$, $\phi = 0°$
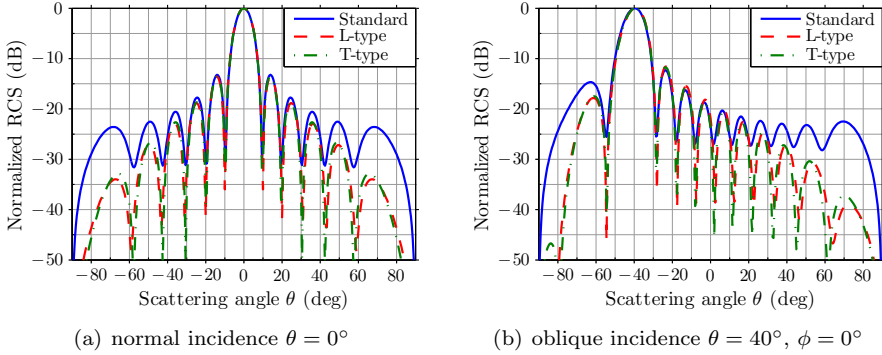
Figure 3.10: Normalized RCS for the three types of corrugated surfaces working as hard surfaces.

corrugations is also very similar: $t = 1.9$ mm for the L-type and $t = 1.6$ mm for the T-type corrugations. On the other hand, the standard corrugated surface exhibits a bit different RCS pattern because of the almost inexistent conducting surfaces between corrugations ($t = 0.3$ mm).

(a) normal incidence $\theta = 0°$ (b) oblique incidence $\theta = 40°$, $\phi = 0°$
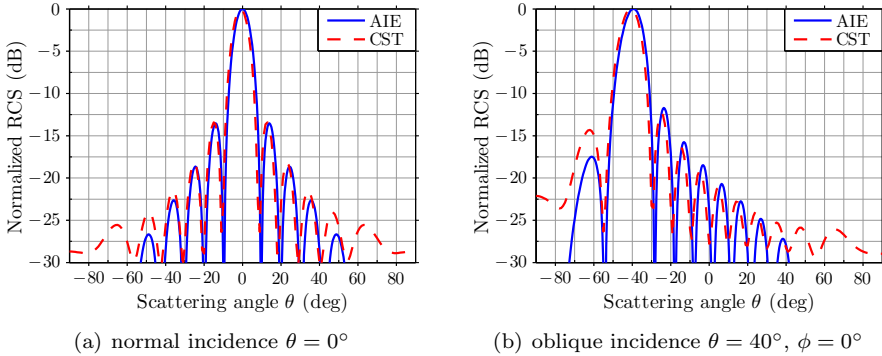
Figure 3.11: Comparison of the normalized RCS obtained with CST and the AIE approach for a T-type hard surface.

In Fig. 3.11, the AIE method is compared again with CST. Now for the T-type corrugations of the previous example, under normal incidence in Fig. 3.11(a) and under oblique incidence ($\theta = 40°$, $\phi = 0°$) in Fig. 3.11(b). Very good agreement is observed once more for these cases.

Finally we have solved for the scattered field of a $40\lambda \times 40\lambda$ large T-type hard surface under normal incidence. Groove dimensions are those of the previous
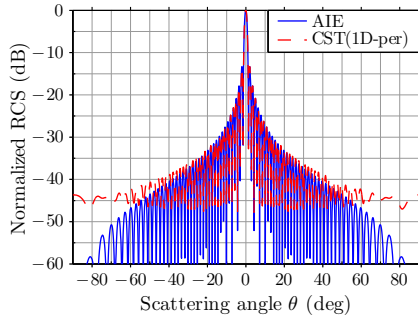
Figure 3.12: Normalized RCS of a $40\lambda \times 40\lambda$ T-type hard surface under normal incidence. Result is compared with an infinite $\times$ finite (40λ) hard surface simulated with CST.

example. The problem has been solved using the CG-FFT technique. The solver took 13 minutes to solve the 385000 unknowns involved (see Table 3.1). A surface of this size is beyond the reach of CST. Therefore, for comparison purposes, we have simulated a structure, which is equivalent to it, as long as the H-plane (XZ-plane) is concerned. The corrugated surface is 40λ in width in the H-plane and infinite periodic in the E-plane, otherwise CST would not be able to deal with the problem. Fig. 3.12 shows very good agreement between both plots. The differences again are due to the presence of an infinite conducting plane in our MoM model. It is worth mentioning that if other incidence angle was chosen, an infinite $\times$ finite model could not be used for comparison.

Size	Computation time	Unknowns number	Iterations number
$20\lambda \times 20\lambda$	2 min 47 sec	95760	14
$30\lambda \times 30\lambda$	7 min 42 sec	214682	15
$40\lambda \times 40\lambda$	13 min 18 sec	383520	17
$50\lambda \times 50\lambda$	25 min 25 sec	599400	18

Table 3.1: Analysis of large T-type corrugated surfaces of different sizes.

The problem was solved for different sizes of the hard surface. Table 3.1 brings together the number of unknowns involved for each case, the number of iterations needed by the CG algorithm to converge, and the computation time taken by the solver. It can be noted that the number of iterations hardly increases for larger surface sizes, thus the increase of computation time is basically due to a greater number of unknowns.

Chapter 4

MoM analysis of SHWWs using the AIE

4.1 Introduction

A method of moments formulation based on the Aperture Integral Equation (AIE) was developed and presented in chapter 3 to analyze corrugated surfaces. This approach is not only valid for standard U-shaped corrugations, but also for planar realizations of hard surfaces, like the inverted L-, and T-type corrugations. Besides, it has no restrictions on the geometrical parameters of the structure. The main disadvantage of the AIE approach for the scattering of corrugated surfaces is the intrinsic presence of an infinite conducting surface surrounding the corrugated surface, and thus distorting the results for the scattered field at grazing angles [139]. This is a general drawback for any aperture problem as image theory is applied.

Following the AIE approach to analyze corrugated surfaces described in the previous chapter, it is extended here to include the presence of a metal plate standing to some distance above the corrugated surface. Thus, the implemented code should be suitable to analyze a single hard wall waveguide consisting of a parallel plate waveguide whose bottom plate is a corrugated surface of one of the types seen in chapter 3 (U-, L-, and T-shaped corrugations). As was demonstrated in chapter 2, a single hard wall waveguide guides a collection of local quasi-TEM waves that share the whole cross-section of the waveguide. This especial feature lend the waveguide a promising potential to be used for applications, specially over 30 GHz, like slot array antennas and slotted-waveguide power amplifiers. A rigorous and efficient analysis method is therefore essential to study such complex problems, usually electrically large.

Slot array antennas have been frequently used for high gain applications so they can cover several tens of wavelengths of side. An optimized design could require hundreds of iterations to reach the antenna specifications rendering the problem unsolvable by means of commercial software. There is a need of more specific codes to solve this problem in particular in a rigorous and efficient manner. A MoM formulation based on the AIE to be used together with acceleration techniques represents a powerful tool to tackle the design of large SHW-waveguide fed slot arrays.

This chapter extends the AIE approach to solve for propagated fields within SHW-waveguides. Simulated results are compared to those obtained with commercial software. Slot coupling to the waveguide and influence of slot length on slot array currents pattern have been studied. The main disadvantage of the AIE approach as a result of the intrinsic presence of an infinite conducting surface surrounding the corrugated surface is now the creation of a standing wave that distorts the field pattern within the waveguide from the real one. From the propagation point of view this drawback is not so important, but for the slot array design becomes critical. The problem must be then overcome suppressing reflected fields at the end edges of the waveguide. The chapter concludes with a study of the mutual coupling between slots belonging to different rows of a planar array. Such study constitutes the first step towards the design of SHW-waveguide fed slot arrays.

4.2 MoM analysis based on the AIE

The aperture integral equation approach is extended here to solve for fields within single hard wall parallel-plate waveguides. As it was pointed in section 3.2 the AIE is the standard procedure to deal with apertures on conducting surfaces. The basic theory establishes two equivalent problems for regions a and b in Fig. 4.1. Now region a is a parallel-plate waveguide whereas region b is still a groove. These two problems become independent as the aperture is closed by a conducting surface. Continuity of tangential electric fields in the aperture is assured by imposing equivalent magnetic currents on both sides of the closed aperture, while the enforcement of the continuity condition of tangential magnetic fields yields the operator equation

$$H_{tan}^a(M) + H_{tan}^{inc} = H_{tan}^b(-M). \tag{4.1}$$

whose solution determines the unknown equivalent magnetic current M.

Look back to section 3.2 for more details of the MoM formulation based on the AIE approach. Using MoM the operator equation leads to a matrix equation
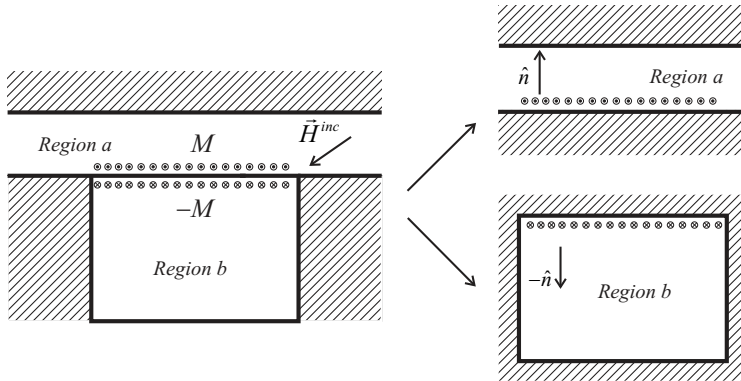
Figure 4.1: Side view of a groove in a standard U-corrugated surface, which is part of a SHWW, and equivalent problems for regions a and b.

$$[Y^a + Y^b]\bar{V} = \bar{I} \tag{4.2}$$

where $[Y^a] = [\langle W_m, H^a_{tan}(M_n)\rangle]_{N \times N}$ is the external admittance matrix, $[Y^b] = [\langle W_m, H^b_{tan}(M_n)\rangle]_{N \times N}$ is the internal one and $\bar{I} = -[\langle W_m, H^{inc}_{tan}\rangle]_{N \times 1}$ the excitation vector.

Since now the external problem, region a, is a parallel-plate waveguide, the entries of $[Y^a]$ can be obtained using the parallel-plate Green's function instead of the free-space Green's function employed in section 3.2. The external problem involves again a finite set of magnetic currents, but this time placed on the bottom plate of an infinite parallel-plate waveguide. As before, $[Y^a]$ will be a block-Toeplitz matrix and in consequence the CG-FFT method will be applied once more to accelerate computations. The procedure followed to compute internal admittances $[Y^b]$ is exactly the same as the one described in section 3.2 for U-shaped corrugations on one hand, and for L- and T-shaped corrugations on the other.

4.3   Numerical results

A case of a single hard wall parallel-plate waveguide has been simulated and compared with commercial software CST Microwave Studio to show the validity of this approach. Both, single and multiple excitation are applied. Afterwards, a radiating slot is placed on the top metal plate of a SHWW to study the coupling to the waveguide as a function of the slot length. Finally, a linear 8-slot array on a SHWW has been analyzed.

4.3.1 Wave propagation

Consider a 4λ wide $\times 12\lambda$ long SHWW whose hard wall is made up of standard U-shaped corrugations. Electric field is excited by a coaxial probe at its center and the working frequency is 10 GHz. Groove depth is $h = 4.33$ mm (around $\lambda/(4\sqrt{\varepsilon_r - 1})$ at 10 GHz), edge width $s = 1$ mm, corrugation period $p = 3$ mm and dielectric permittivity $\varepsilon_r = 4$. The gap between the corrugated surface and the top metal plate is $d = 2$ mm.
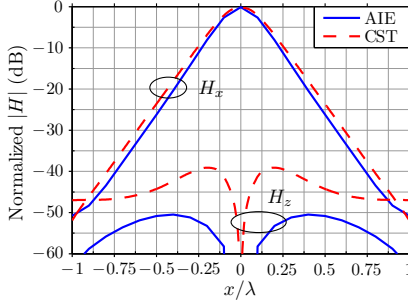
Figure 4.2: Magnetic field of the wave excited by a single probe at a transverse cut at 5λ away from the source obtained with the AIE approach and compared with CST.

Fig. 4.2 shows both, transverse x- and longitudinal z-components of the magnetic field of the wave excited by a single probe within the SHWW at 10 GHz. A transverse cut at 5λ away from the source is shown. Fields are normalized to the maximum. As can be seen, the agreement between the results obtained with the AIE approach and those from CST is good. For the CST calculation, an absorbing boundary condition around its rim was defined. Whereas, for the AIE approach infinite metal plates are considered, as a consequence of using image theory. The corrugated surface is finite, but beyond its edges a conducting surface extends to infinite. The top metal plate is also regarded infinite, remember the Green's function of a parallel-plate waveguide was used for the calculation of external admittances in the AIE approach. In spite of the different boundary conditions of both approaches, AIE approach and CST simulator, the agreement is reasonable good because the wave excited within the SHWW is a local wave, which should not be affected by whatever is beyond a certain distance from the wave in transverse direction. As presumed, a local quasi-TEM wave decaying fast to the sides can be observed. Longitudinal z-component is negligible. And as for the transverse x-component, at $\lambda/2$ away from the source in transverse direction field levels are almost -30 dB below the maximum. This can also be seen in Fig. 4.3 where fields at several

transverse cuts are displayed. The wave keeps its shape as it propagates along the waveguide.
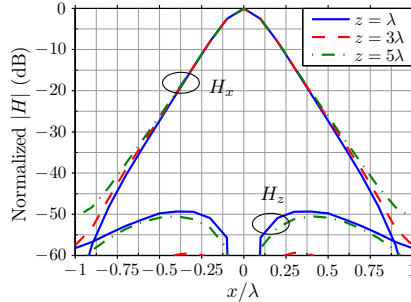
Figure 4.3: Magnitude of the magnetic field at several transverse cuts (at λ, 3λ, and 5λ away from the source) produced by a single probe.

Next, a multiple excitation is applied. Four source probes close to one end of the waveguide generate four quasi-TEM waves. Probes are fed with uniform magnitude and a linear phase of $45°$. They are equally spaced apart 0.7λ, a typical spacing between rows of slots in a slot array to avoid grating lobes. Fig. 4.4(a) shows the magnitude of the magnetic field at two transverse cuts. Four independent quasi-TEM waves can be observed. Even with a linear phasefront the waves do not intermingle keeping the magnitude pattern at the probes locations uniform along the propagation direction. As can be seen, isolation level between waves could be enough for slot array antennas. The preservation of the phase profile is also shown in Fig. 4.4(b).

(a) Magnitude of the transverse and longitudinal components

(b) Phase profile of the transverse component
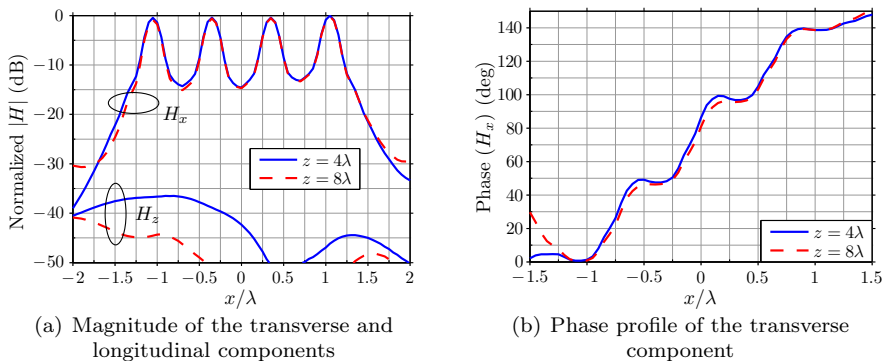
Figure 4.4: Magnetic field of four waves generated by four probes fed with the same amplitude and a linear phase of $45°$.

4.3.2 Slot resonance length

Once it has been demonstrated that the AIE approach is perfectly valid for the analysis of single hard wall waveguides, next step is to extend the code to include radiating slots in the top metal plate. Luckily, this step is quite immediate.

First of all, consider a slot in the top metal plate of a SHW-waveguide (see Fig. 4.5). For the calculations suppose a SHWW of the type and dimensions of section 4.3.1. The slot lies at the waveguide center and its width is $\omega_s = 1$ mm. Slot thickness is assumed infinitesimal.
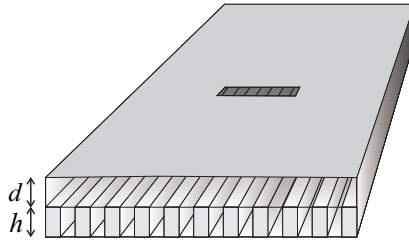
Figure 4.5: Radiating slot in the top metal plate of a SHWW.

(a) Slot admittance

(b) External radiated power
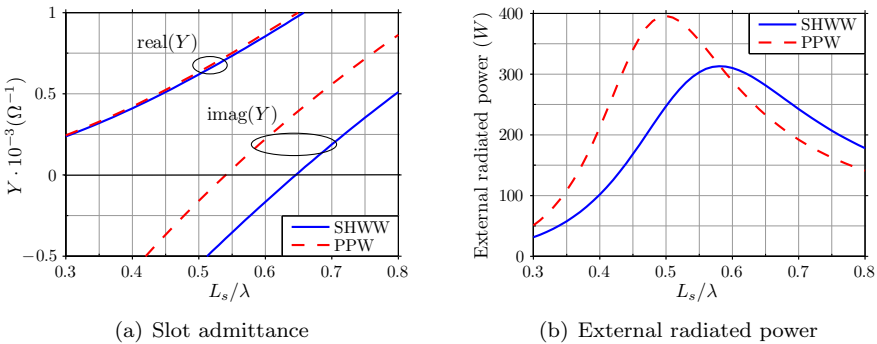
Figure 4.6: Slot admittance and external radiated power as a function of the slot length. Comparison between a SHWW and a PPW.

In order to find the resonance length of the slot, the admittance is represented in Fig. 4.6(a) as a function of slot length. Real and imaginary parts of the slot admittance can be seen for the SHWW. For the sake of comparison, calculations were also done for a metal Parallel Plate Waveguide (PPW) of the same height as the SHWW. It is said that the slot is resonant when it is totally

reactive, i.e., if the susceptance is zero. Looking at Fig. 4.6(a) it can be noticed that slot resonance length is around 0.64λ for the SHWW, and a bit shorter for the PPW, about 0.54λ. Anyway, Fig. 4.6(b) shows the external radiated power. The slot length corresponding to the maximum external radiated power is 0.58λ for the SHWW, and 0.5λ for the PPW. For a traveling-wave slot array design, this is the slot length that should be taken in order to get maximum efficiency, i.e., maximum radiated power. On the contrary, for resonant designs, slot length should be close to the resonant length.

4.3.3 Linear slot array

Let us now suppose a linear array consisting of 8 transverse slots fed by this SHWW as represented in Fig. 4.7. The excitation is a single probe. The waveguide has been filled with a dielectric material of permittivity $\varepsilon_{r\ gap} = 1.5$ to avoid grating lobes and the groove-filling material has a dielectric permittivity of $\varepsilon_r = 6$. The groove depth has changed to 3.54 mm to fulfill the hard condition $h = \lambda/(4\sqrt{\varepsilon_r - \varepsilon_{r\ gap}})$. The remaining parameters of the geometry are kept. Slots are 1 mm wide and they are equally spaced apart λ_g, being $\lambda_g = \lambda/\sqrt{\varepsilon_{r\ gap}}$.
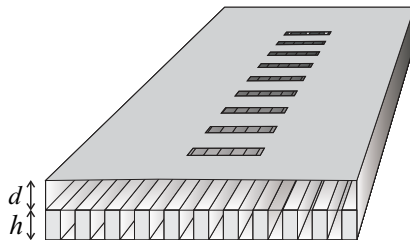
Figure 4.7: 8-element linear array of transverse slots on a SHW-waveguide.

The magnetic currents on the slots of the array are shown in Fig. 4.8 for two different slot lengths, a smaller one $L_s = 0.3\lambda$ and other closer to the resonant case $L_s = 0.4\lambda$ but still quite far away from this one. All the slots of the array are identical. Magnetic current values are indicated by icons, nevertheless a spline interpolation has been added for the sake of clarity. As expected, the first slots are more excited than the latest since some of the input power has already been radiated by the former. This is clearly seen in Fig. 4.8(a) where the magnitude of the magnetic current of slots is falling from the source. The decrease is more pronounced for the longest slots. Fig. 4.8(b) illustrates that the slot currents are much more affected by mutual couplings for longer slots whose lengths are closer to the resonant one than for shorter slots. For shorter

51

slots, the phase of the slot magnetic currents is almost uniform. This is not the case for longer slots closer to the resonance. Thus slot positions and array spacings should be modified to achieve all the slots to be in phase. Several repetitions are usually needed in this process that is carried out in general terms in the design of slot arrays.

The radiation patterns of the 8-element slot array for the two slot lengths considered are depicted in Fig. 4.9. The differences between both are not significative, just a slight shift of the main beam steering is hardly noticeable. Obviously, for slot lengths approaching to the resonant length, the phase shifting among slots is sharper and consequently the radiated beam is clearly tilted.
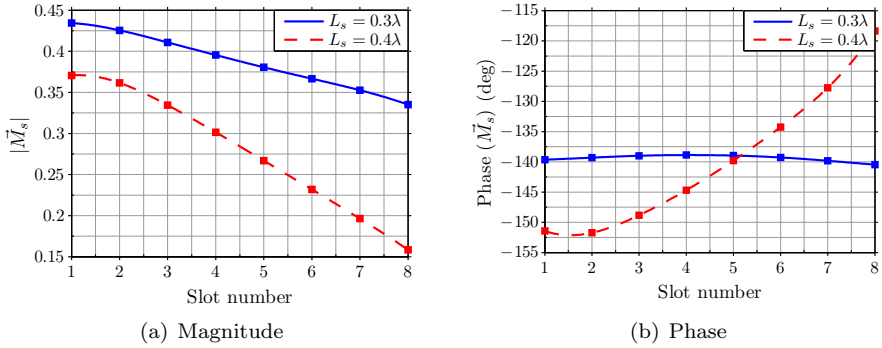
(a) Magnitude

(b) Phase

Figure 4.8: Magnitude and phase of slot magnetic currents of an 8-element slot array for two different slot lengths.
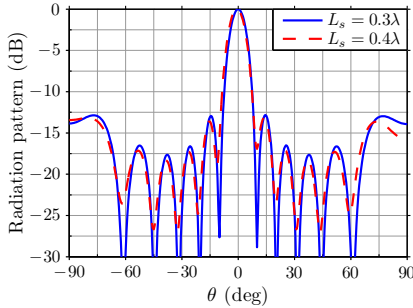
Figure 4.9: Radiation pattern of an 8-element slot array for two different slot lengths.

4.4 Improvements for the AIE approach

For the purpose of designing a traveling-wave slot array, the AIE approach the way it was explained is not entirely appropriate. And the reason is that the AIE approach gives rise to a standing wave inside the SHW-waveguide distorting the wave from the real one, which should be a traveling wave.

The presence of a standing wave within the waveguide comes from applying image theory for aperture problems. Magnetic currents are defined over the apertures, which are closed by a conducting surface extending to infinite. Thus, the wave propagating inside a SHWW encounters an infinite PPW as reaches the end edges of the SHWW. At the interfaces between both media some of the power is reflected back to the SHW-waveguide resulting in a standing wave inside.

The problem must be then overcome suppressing reflections at the end edges of the SHW-waveguide, i.e., ending the waveguide with a matched-load. For this aim, new elements, referred to as magnetic resistive cards, have been introduced into the waveguide. These resistive cards are added to the end portions of the waveguide in order to dissipate the power arriving to them. Actually, they are part of the magnetic currents that were initially established on the grooves, so that now a new term appears in the magnetic currents expression resembling the formulation for dielectric materials.

Magnetic resistive cards are only added to the magnetic currents, which are close to the end edges of the waveguide. And their weights grow exponentially towards the end edges to suppress the residual power gradually and avoid reflections. The exponential rise must be adjusted to dissipate all the power effectively.

(a) Magnitude   (b) Phase
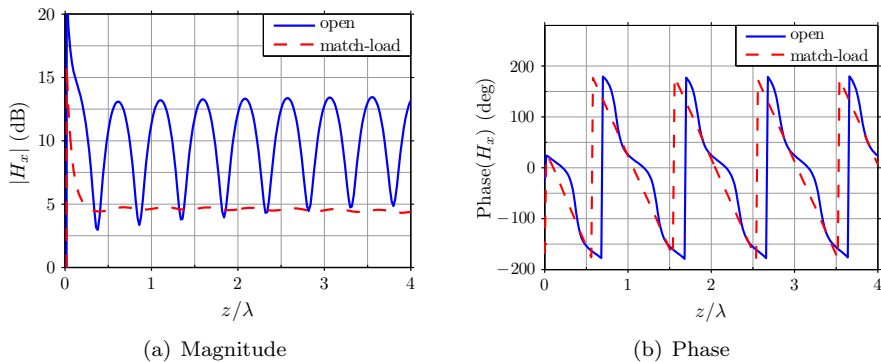
Figure 4.10: Magnetic field of the wave along a SHW-waveguide and a matched-load ended SHWW.

The result of using magnetic resistive cards to achieve a traveling-wave propagation within SHW-waveguides is illustrated in Fig. 4.10. A standing wave with a Voltage Standing Wave Ratio (VSWR) about 8 dB can be seen in Fig. 4.10(a). After adding resistive cards, reflections at the end edges are eliminated effectively and a traveling wave is obtained, just like in matched-load ended waveguides. This effect is also shown in Fig. 4.10(b) where the phase becomes perfectly linear.

4.5 Study of slot mutual coupling

Prior to face the design of SHW-waveguide fed slot arrays, it is convenient to study slot mutual couplings. Transverse slots belonging to the same row and transverse slots belonging to adjacent rows have been considered.

(a) two slots at the same row (b) two slots at adjacent rows
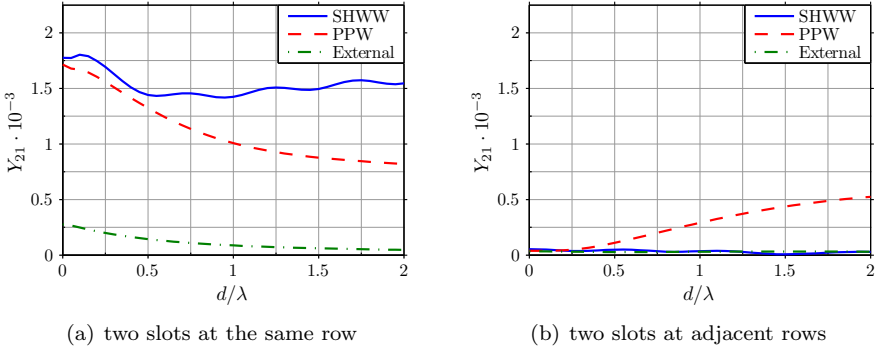
Figure 4.11: Mutual admittances of two transverse slots on a SHWW and a PPW as a function of the spacing d between them in longitudinal direction.

Fig. 4.11(a) shows mutual admittances between two slots belonging to the same row as a function of the spacing d between them. External admittances are almost insignificant with respect to the total ones. Total admittances have been obtained for the SHWW and for a PPW of the same height as the former. As can be seen, for a SHWW the values of mutual admittances are kept quite constant with the spacing between slots. On the contrary, for a PPW these values fall progressively as the spacing increases. These results were expected, since a wave propagates in just one direction within a SHWW whereas it spreads in all directions in a PPW.

Suppose now two slots belonging to adjacent rows. The spacing between rows is 0.7λ, a typical array spacing for planar slot arrays to avoid grating lobes. The spacing along the longitudinal direction between the two slots considered is d. Mutual admittances between both slots are shown in Fig. 4.11(b) as a

function of the spacing d. For a PPW, it is observed that mutual admittances go up with increasing spacing. This fact is related to the radiation pattern of a slot apart from the free propagation of waves within a PPW. On the other hand, for a SHWW, mutual admittances are again kept quite constant, but now they are almost negligible compared to the ones of a PPW, just like external admittances.

In short, for a SHWW, the mutual coupling between two slots at adjacent rows is much lower than the mutual coupling between slots at the same row. Besides, mutual coupling is not changing significatively with spacing d between slots. This is not the case for a PPW.

The results show that definitely the strong transverse attenuation experienced by the local quasi-TEM modes parallel to each other within a SHWW makes the coupling between slots belonging to different rows nearly negligible. Therefore, the design of a planar slot array made up of a collection of slot rows on a SHWW could be simplified. A first design taking into account only the self-admittance of a row of slots could be enough even as the final design of a 2-D slot array.

Chapter 5

Slot arrays on SHWWs

5.1 Introduction

This chapter has two objectives. On one hand, to demonstrate experimentally a realization of a SHWW fed slot array in order to show the isolation among rows of slots. And on the other, to show the design process of SHW-waveguide fed slot arrays by using the AIE approach presented in previous chapters.

Regarding to the latest objective, the design and optimization process of SHW-waveguide fed slot arrays using the AIE approach will be described. Firstly, a circularly polarized 1-D array design is carried out in two stages, a design stage in which the geometrical parameters are determined without considering mutual couplings, and an optimization stage where the geometrical parameters of the whole array are optimized to fulfil antenna specifications. Finally, the 2-D array design is shown.

5.2 Experimental demonstration of slot arrays on SHWWs

This section shows an experimental realization of a SHWW fed slot array for the only purpose of demonstrating the isolation among rows of slots. A hard surface like that shown in section 2.3 has been manufactured to work at 14 GHz. The hard surface is constructed by drilling and metalizing via-holes and etching narrow strips in a copper-clad laminate. Following this procedure, the hard surface experiences some deviation from the expected theoretical performance of a corrugated hard surface. Therefore, the propagation constant and the working frequency have to be found previously to place the radiating slots at the correct positions. This can be done by means of simulations obtained using

commercial software or by means of field measurements of the manufactured waveguide.

From the design point of view, the implemented code that was shown in previous chapters is only valid for hard surfaces with continuous grooves. Thus, in case of having a hard surface made up of metal strips and via-holes in a PCB, and in order to use this numerical code for the analysis, it is essential to know the propagation constant and the working frequency of the constructed hard surface. In this way, it is easy to find an equivalent corrugated surface with exactly the same behavior as the constructed one. This can be achieved filling the waveguide with a dielectric material of very low permittivity, slightly above 1 and usually below 2. Then, the simulations needed for the design and optimization of slot arrays can be done on this equivalent corrugated surface.

Nevertheless, this code was not used for this experimental demonstration whose objective is to show the isolation level among rows of slots. For that purpose, an array of 9×4 short slots fed by the constructed hard surface has been manufactured. All the slots have the same dimensions, which were arbitrarily chosen to 1 mm wide and 5 mm long. Transverse slots were used for linear polarization. Slots are a guiding wavelength, λ_g, equally spaced apart in longitudinal direction for broadside radiation, and the spacing between rows is $0.75\lambda_g$. The guiding wavelength was obtained by means of field measurements along the shortcircuit ended waveguide as an average of the spacing between the minima of a standing wave excited inside this cavity. The average distance between minima must be around $\lambda_g/2$.
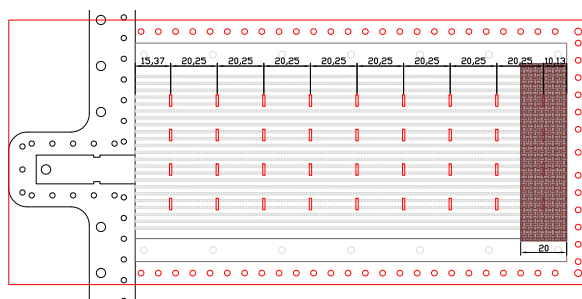
Figure 5.1: Sketch of the experimental prototype.

The sketch of the experimental prototype is shown in Fig. 5.1 where we can see that only one monomode port feeds the SHWW so that only one row of slots, the second one from the bottom, should be excited. In order to evaluate the isolation level between rows, three measurements were done at the working frequency of 14 GHz. For the first one, only the slots belonging to the row excited by the monomode port are present. For the second measure, apart

from the slots that should be excited, the slots belonging to one adjacent row, the first one from the bottom, are also present. And the last measure was done considering all the slots of the four rows.

Since the dimensions of the slots have not been designed to radiate all the power coming into the waveguide, most of the power arrives to the end edge of the waveguide. Thus, the waveguide was terminated with an absorbing material to avoid reflections at the end edge of the waveguide, but even though some part of the power will be reflected giving rise to a standing wave inside the waveguide. As can be seen in the sketch of Fig. 5.1 the last slot of each row is blocked by the absorber so that when the waveguide is ended with the absorber the slot array actually consists of 8×4 elements. This is not the case for the waveguide ended with a short-circuit where each row of slots will have 9 elements.

(a) Magnitude

(b) Phase
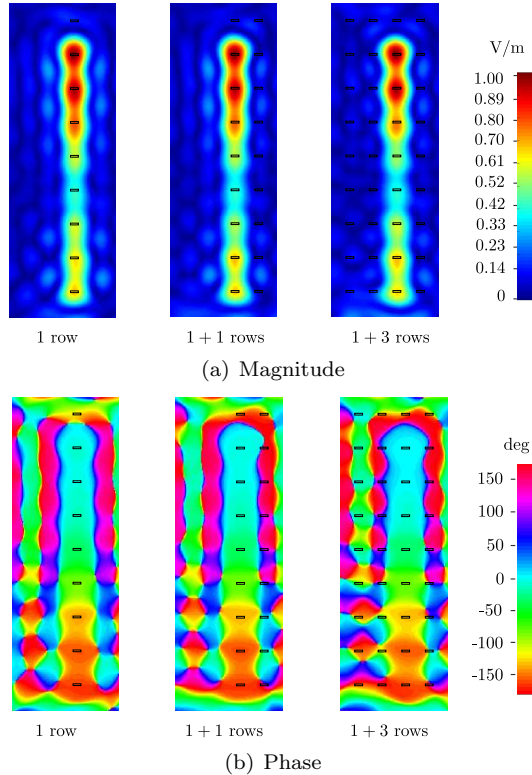
Figure 5.2: Transverse component of the magnetic currents over the slotted plate for a single excitation and different number of slot rows present.

(a) E-plane   (b) H-plane
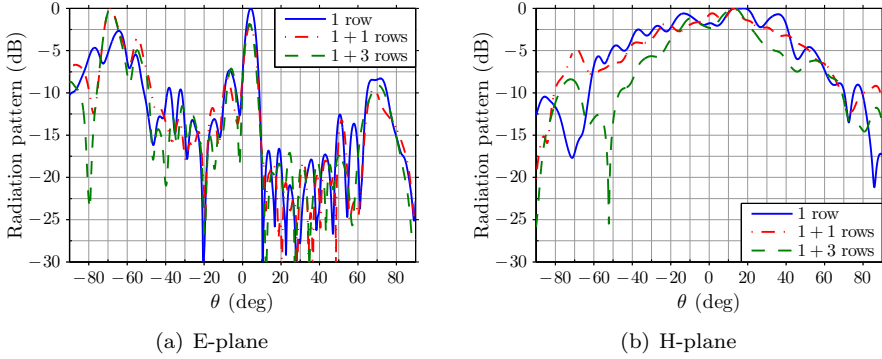
Figure 5.3: Radiation pattern for a single excitation and different number of slot rows present.

The transverse component of the magnetic currents over the slotted plate are shown in Fig. 5.2 for these three cases. It is observed that the agreement between these three cases is good, what means that fields inside the SHWW coming from a monomode waveguide and exciting one row of slots are not coupling to the other rows of slots. Even if the SHWW is working well, in the sense that it propagates very confined local quasi-TEM waves, this performance could be destroyed by the effect of the slots on the propagated fields. This experimental realization demonstrates that slots hardly affect the performance of the SHWW, which keeps a high isolation between rows. The coupling among rows of slots is so low that it could be neglected for design purposes.

The same conclusion can be extracted from Fig. 5.3 where two cuts of the radiation pattern are shown for these three cases. The maximum of the radiation pattern is shifted approximately 4° from broadside direction as can be seen in Fig. 5.3(a). This is due to the fact that the presence of slots affects to the propagation constant and thus the guiding wavelength inside the waveguide, what gives rise to a new effective guiding wavelength, which is usually a bit shorter than the former. In this way, slots are not actually in phase as it is observed in Fig. 5.2(b) where a difference of around 150° can be appreciated between the first and last slots of the radiating row, and in consequence the radiated beam is tilted.

The correct position of the radiating slots to give a broadside radiation would require an iterative process to adjust the positions, since every change on the slot positions involves also a variation of the effective guiding wavelength, but this is beyond of this simple experimental demonstration. Next section will expose the design and optimization of a slot array for circular polarization using ad-hoc codes, what will allow us to obtain nice radiation patterns.

(a) Magnitude   (b) Phase
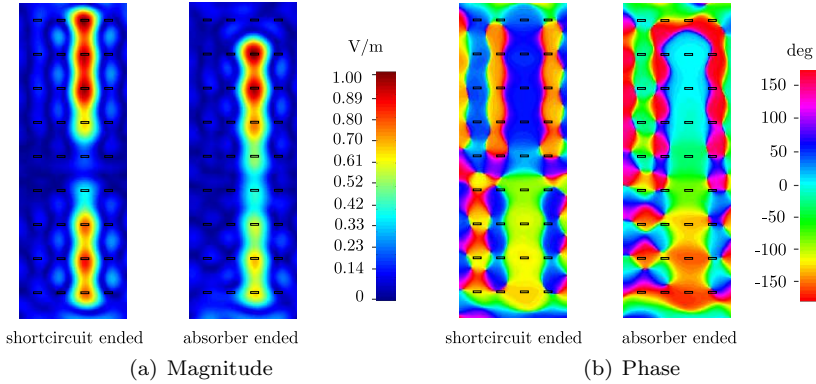
Figure 5.4: Transverse component of the magnetic currents over the slotted plate for a single excitation comparing the SHWW ended with an absorber and with a short-circuit.

To finish with this experimental demonstration, a last measure with the waveguide ended with a short-circuit was done to check if the ability of the SHWW to lead local waves loses in the presence of a short-circuit at the end edge of the waveguide. This short-circuit could spread the fields arriving to it over the cross-section and reflect them back to the waveguide following parallel paths. Fortunately, this phenomenon do not happen and the standing wave impinging and reflecting from one edge to the other is maintained confined. This can be clearly observed in Fig. 5.4 where only the slots belonging to the fed row are excited as in the case of having an absorber. Fig. 5.4(b) shows again that the slots have different phase being now the phase difference between the first and last slot even larger than for the absorber case. It must be noted that two slots at the central part of the waveguide were little excited for the absorber case, but now they hardly radiate (see Fig. 5.4(a)). This is due to the locations of these slots that must be close to minima of the standing wave. Obviously, the minima of the standing wave are lower for the short-circuit case.

5.3   Circularly polarized 1-D array

The design of a circularly polarized 1-D array at 15 GHz is shown in this section. Given that the unique propagation allowed inside a SHW-waveguide is a quasi-TEM mode, Left-Handed Circularly-Polarized (LH-CP) waves could be generated by a radiating element constituted by a pair of slots oriented at $\pm45°$, which are $d_s = \lambda_g/4$ apart, like the one shown in Fig. 5.5.

61
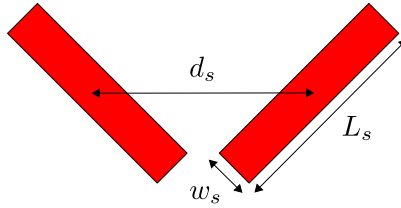
Figure 5.5: A $\pm 45°$ slot pair for circular polarization.

First of all, the steps followed to get the first design are described. Since the mutual couplings among array elements perturb the propagated fields inside the waveguide, a later optimization process is always needed to get a final design that fulfills antenna specifications. This optimization process is also explained here.

5.3.1 First design

A first design of a LH-CP 1-D array is obtained in this section. The design process is as follows.

Efficiencies of the array elements

Each pair of slots represents one array element. Depending on the number of elements of the array, each element must have a certain efficiency to get a given illumination over the array and synthesize a given radiation pattern.

The efficiency of each array element is defined as the ratio between the radiated power and the received power, being the received power the one that arrives to one element and the radiated power the one that is radiated by this element. The difference between both is the transmitted power that follows propagating within the waveguide towards the next element provided that the reflected power is negligible.

For a traveling-wave design, all the power inserted into the waveguide should be radiated by the array elements so that no power arrives to its end edge. For that, the last element has to radiate the remaining power, which has not been radiated yet by the previous elements. Thus, the efficiency of the last element has to be maximum. Assuming the last element is the element N, it must be realized

$$ef_N = 1 \tag{5.1}$$

Given an array of N elements and a radiated power distribution given by $[\omega_1, \omega_2, \ldots, \omega_i, \ldots, \omega_N]$ where $\omega_i \in [0, 1]$, and supposing reflected power is negligible, the efficiency of the rest of elements i can be expressed by

$$ef_i = \frac{\omega_i ef_{i+1}}{\omega_{i+1} + \omega_i ef_{i+1}}, \quad i = 1, \ldots, N - 1 \tag{5.2}$$

In our case, a uniform illumination over the array is desired in order to achieve maximum efficiency of the antenna. A number of 10 elements was arbitrarily chosen for the design. Table 5.1 shows the efficiencies of each array element.

Element	Efficiency
1	0.100
2	0.111
3	0.125
4	0.143
5	0.167
6	0.200
7	0.250
8	0.333
9	0.500
10	1

Table 5.1: Efficiencies of a 10-element 1-D array.

Afterwards, the physical parameters of each pair of slots giving rise to the efficiencies of Table 5.1 must be found. As it is known, shorter slots generate lower efficiencies. So, a table of values relating efficiency to slot length should be obtained. For this purpose, there is a task that has to be done previously, as stated below.

Slot pair parameters (L_s, d_s, of)

Each pair of slots has to be designed properly to radiate Left-Handed Circularly-Polarized (LH-CP) waves. Assume slot width is $w_s = 1$ mm, and the two slots forming a pair have the same length L_s. For each slot length, there must be a spacing d_s and offset of optima to radiate circularly polarized waves, being d_s the spacing between the two slots of one pair from center to center in longitudinal direction, and of the offset or distance between the center of each of the slots forming a pair and the array alignment axis in transverse direction (see Fig. 5.6). Two different offsets for the first and second slots can be seen, but by now only one offset is assumed so that $of_1 = of_2 = of$.
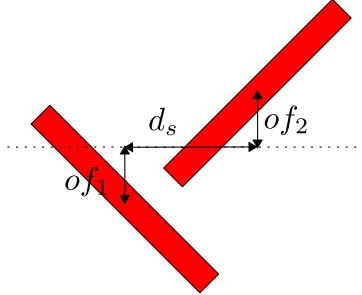
Figure 5.6: A $\pm 45°$ slot pair with offsets for circular polarization.

For the calculations it was considered only one pair of slots on the SHWW, without taking into account mutual couplings among slot pairs, and a coaxial probe as excitation. The slot pair is lying 4λ away from the source.

Given a slot length, the spacing and offset have been optimized to get a minimum Axial Ratio (AR). For that, the magnetic currents at both slots should have the same magnitude and a phase difference of $90°$. Assuming A_1 and A_2 are the magnitudes of the magnetic currents at the centers of the first and second slots, respectively, and ϕ_1 and ϕ_2 are their phases, the optimization process can be described as follows:

1. Check if $A_1 \neq A_2$. If $A_1 < A_2$, then slots are moved closer. If $A_1 > A_2$, then slots are moved away from each other.

2. Check if $\phi_1 \neq (\phi_2 + 90°)$. If $\phi_1 > (\phi_2 + 90°)$, then slots are moved closer. If $\phi_1 < (\phi_2 + 90°)$, then slots are moved away from each other.

3. If still $\phi_1 \neq (\phi_2 + 90°)$, then the offset is enlarged slightly and the cycle is closed starting again at step 1. Otherwise, the process is ended.

It must be noted that slots do not have to cross so that a minimum distance between slots suitable for the milling machine must be kept. This constraint has to be checked at steps 1-2. Besides, the offset has an upper limit to avoid that array elements belonging to adjacent rows interfere. Both constraints represents a limitation for the longest slots to get circular polarization.

Obviously, stop criteria must be established for steps 1-2 depending on the required results. Since a later optimization process must be carried out considering all the array elements, there is no sense in being excessively strict at this point.

Fig. 5.7(a) shows the values of the spacing and offset obtained for a given slot length. The values were obtained for slot lengths $L_s \in [0.3\lambda, 0.5\lambda]$ at intervals of

(a) Spacing and offset   (b) Axial Ratio
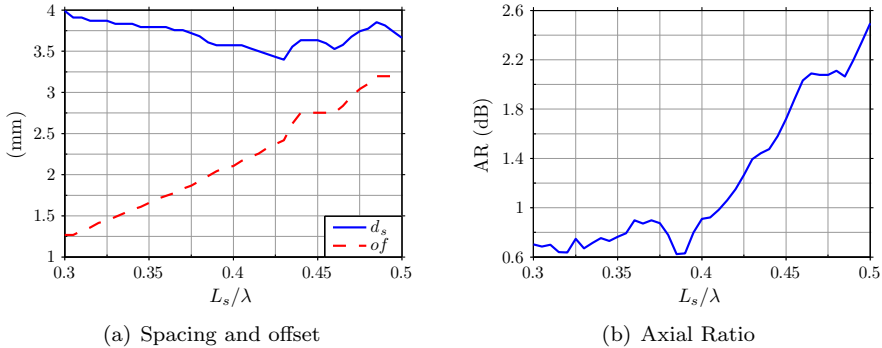
Figure 5.7: Spacing d_s and offset of as a function of slot length L_s of $\pm 45°$ slot pairs, and axial ratio obtained for those parameters.

0.01λ. As can be seen in Fig. 5.7(b), as a consequence of the above-mentioned constraints the axial ratio gets worse for larger slot lengths. This could be improved considering two different offsets for each slot of a pair, however it has been proved that this loss of symmetry has negative consequences on the total axial ratio given by the totality of slot pairs forming the 1-D array. Therefore, this option should be only employed in case of considering also mutual couplings among pairs for the calculations, at least among the closest ones, what would be more realistic. In our case, the results with one offset for the two slots were good enough as can be seen in Fig. 5.7(b), so we did not go further with this other possibility. Nevertheless, it is an alternative that is worth considering for future designs.

Efficiencies versus slot pair parameters table

Once groups of three parameters $(L_s,\ d_s,\ of)$ were founded, the efficiency corresponding to each group was obtained (see Fig. 5.8). The efficiency of one element is the ratio between the radiated power and the received power. Assuming reflected power is negligible, the efficiency can be calculated as

$$ef = 1 - \frac{P_t}{P_r} \tag{5.3}$$

where P_r is the received power by one element and P_t is the transmitted power towards the next element. P_t is obtained at a point aligned with the source probe in longitudinal direction after crossing the slot pair. As for P_r, it is obtained at the same point, but considering only the waveguide, without presence of slots at its upper plate.
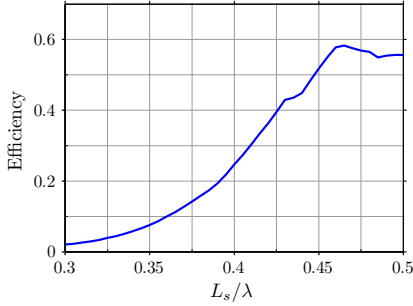
Figure 5.8: Efficiency of $\pm 45°$ slot pairs with parameters (L_s, d_s, of).

Fig. 5.8 shows the efficiency of $\pm 45°$ slot pairs as a function of the slot length L_s. There is one d_s and one of associated to each L_s as shown in Fig. 5.7(a).

Results of the first design

Now, the slot pair parameters of the array elements must be chosen to give the efficiencies reflected in Table 5.1. From Fig. 5.8, given a efficiency value, a L_s value is obtained as a linear interpolation of the calculated data. Then, from Fig. 5.7(a) the associated values of d_s and of are again obtained in the same way.

Element	Efficiency	L_s/λ	L_s (mm)	d_a (mm)	d_s (mm)	of (mm)
1	0.100	0.360	7.204	–	3.792	1.743
2	0.111	0.365	7.292	19.7	3.759	1.774
3	0.125	0.369	7.389	19.7	3.756	1.825
4	0.143	0.375	7.503	19.7	3.717	1.869
5	0.167	0.383	7.655	19.7	3.641	1.956
6	0.200	0.391	7.828	19.7	3.572	2.054
7	0.250	0.400	8.010	19.7	3.572	2.111
8	0.333	0.415	8.299	19.7	3.501	2.256
9	0.500	0.447	8.946	19.7	3.634	2.753
10	0.583	0.465	9.300	19.7	3.576	2.836

Table 5.2: Efficiency, slot length L_s, array spacing d_a, slot spacing d_s, and offset of values of the array elements for the first design.

Once the array elements have been designed to give a uniform illumination for maximum efficiency of the antenna, the array spacing d_a between elements is selected depending on the desired pointing direction of the radiated beam.
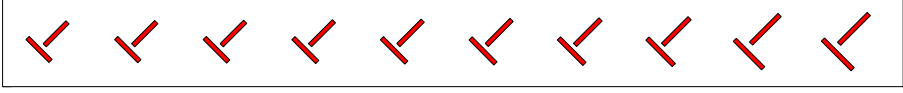
Figure 5.9: Sketch of the first design of a circularly polarized 1-D slot array.

(a) Magnitude

(b) Phase

(c) Axial Ratio

Figure 5.10: Magnitude and phase of the copolar component and axial ratio of the electric field radiated by the array elements for the first design.

In our case, a broadside design is required, so that all the elements should be in phase. Therefore, a spacing among elements of λ_g is imposed, where λ_g is the guiding wavelength.

Table 5.2 shows the values (efficiency,L_s,d_a,d_s,of) corresponding to each array element. It is important to point out that the last element is chosen to give the maximum efficiency in practice, which is below the maximum theoretical one, as can be seen in Fig. 5.8 .

The resulting 1-D array is drawn at Fig. 5.9 and represents the first design.
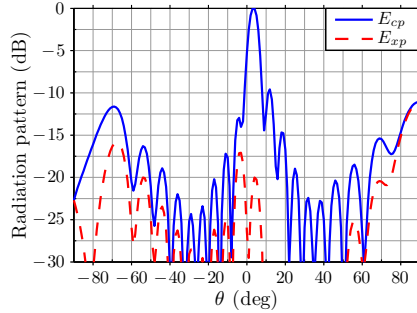
Figure 5.11: Radiation pattern of the first design of a 10-element 1-D array.

Fig. 5.10(a) and Fig. 5.10(b) show the magnitude and phase of the copolar component of the electric field radiated by the array elements, respectively. The magnitude is almost uniform, however there is an important phase shifting among elements that results in a tilt of the main beam, as can be appreciated in Fig. 5.11. This effect is common for array antenna designs due to the influence of mutual couplings on the guiding wavelength. The presence of slots introduces a change in the guiding wavelength λ_g, so that now it is more convenient to refer to the new guiding wavelength as an effective guiding wavelength λ_{ef}. This λ_{ef} is usually below λ_g. Besides, the axial ratio of the electric field radiated by the elements generally gets worse when they are put all together for the same reason, influence of mutual couplings (see Fig. 5.10(c)). The radiation pattern shows grating lobes slightly below -10 dB as a result of the array spacing, which is λ_g. The crosspolar component can also be seen in Fig. 5.11. An axial ratio of 1.52 dB at broadside direction has been obtained, what is acceptable. However, the phase shifting must be corrected by moving array element locations. This change will affect in turn to the electric field radiated by the elements, and not only to the phase, but also to the magnitude and polarization.

In consequence, an optimization process is always needed to fulfill antenna specifications.

5.3.2 Optimization process

The optimization process can be divided in two parts. A first part, referred here as partial optimization, where the steps needed to correct the phase-shifting and magnitude difference of the array elements are taken. And a second part, which is dedicated to get a good axial ratio of the electric field radiated by each element for circular polarization by adjusting physical parameters of slot pairs, such as spacing and offset.

The first part of the optimization process intends all the array elements to give the phases and magnitudes required to fulfill antenna specifications. Since a uniform distribution and broadside radiation patterns are desired in this case, all the elements should be in phase and have the same magnitude. In order to prove that, the electric field radiated by each slot pair at broadside direction is computed. Generally, it is necessary to make some changes to adjust phases and magnitudes of the array elements. Phases can be adjusted just by changing element locations along the array alignment axis. And magnitudes can be altered by modifying slot lengths.

Assuming ϕ_i and A_i are the phase and magnitude of the electric field radiated by the element i, the partial optimization process involves:

1. Check if the phases ϕ_i are equal. If not, element locations are moved Δd_i away, where

$$\Delta d_i = -\frac{\phi_i - \phi_1}{k_g}, \quad i = 2, \ldots, N \tag{5.4}$$

and $k_g = 2\pi/\lambda_g$.

2. Check if the magnitudes A_i are equal. If not, slot lengths of the array elements are changed to give a magnitude, which is an average value of the magnitudes of all the elements. These new slot lengths L_s are obtained from Fig. 5.8 as a linear interpolation of the calculated data, as was done in section 5.3.1. Then, from Fig. 5.7(a) the associated values of d_s and of are again obtained in the same way.

3. If still the phases ϕ_i or the magnitudes A_i are not equal, then the cycle is closed starting again at step 1. Otherwise, the process is ended.

Stop criteria are again established for steps 1-2 depending on the required results. An overrelaxation factor is applied to the deviations in steps 1-2 to facilitate convergence.

Results after partial optimization
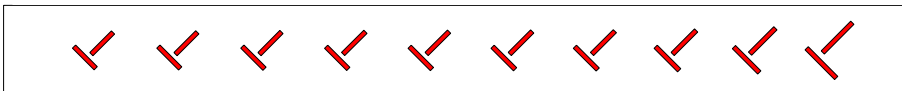
Figure 5.12: Sketch of the design after partial optimization of a circularly polarized 1-D slot array.
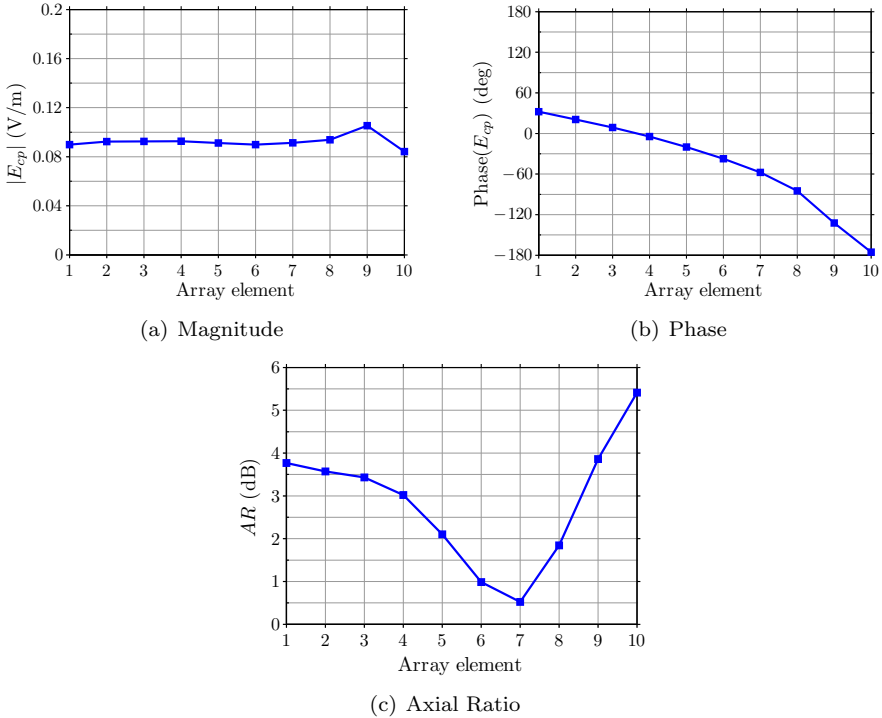
(a) Magnitude

(b) Phase

(c) Axial Ratio

Figure 5.13: Magnitude and phase of the copolar component and axial ratio of the electric field radiated by the array elements for the design after partial optimization.

Figure 5.14: Radiation pattern of the design after partial optimization of a 10-element 1-D array.

Element	L_s (mm)	d_a (mm)	d_s (mm)	of (mm)
1	6.799	–	3.832	1.577
2	6.864	18.725	3.807	1.597
3	6.936	18.673	3.794	1.626
4	6.993	18.613	3.794	1.654
5	7.033	18.551	3.794	1.674
6	7.074	18.459	3.794	1.694
7	7.149	18.311	3.794	1.724
8	7.381	17.986	3.756	1.821
9	7.957	17.509	3.572	2.095
10	9.300	16.613	3.576	2.836

Table 5.3: Slot length L_s, array spacing d_a, slot spacing d_s, and offset of values of the array elements for the design after partial optimization.

After carrying out the partial optimization, the array of Fig. 5.12 whose physical parameters are shown in Table 5.3 is obtained. It is easy to notice that array elements are now closer from each other, what was expected since usually $\lambda_{ef} < \lambda_g$. It is worth noting that spacing d_a between adjacent elements is going down as the elements get larger.

As a consequence of a greater proximity among array elements, grating lobes are lower now, below -15 dB, as Fig. 5.14 shows. As can be observed in Fig. 5.13, all the array elements are now in phase, what means the main beam of the radiation pattern is pointing now at broadside direction (see Fig. 5.14). The magnitude is kept quite uniform. And regarding to the axial ratio of the fields radiated by each element is also quite uniform, but not completely satisfactory. An axial ratio of 2.24 dB at broadside direction is obtained. This result could be improved by carrying out the second part of the optimization process.

Results after complete optimization
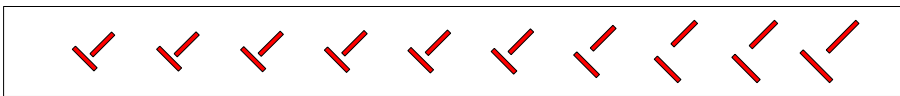
Figure 5.15: Sketch of the design after complete optimization of a circularly polarized 1-D slot array.

The second part of the optimization process entails an adjustment of the physical parameters of slot pairs, specifically slot spacing d_s and offset of, to

(a) Magnitude

(b) Phase
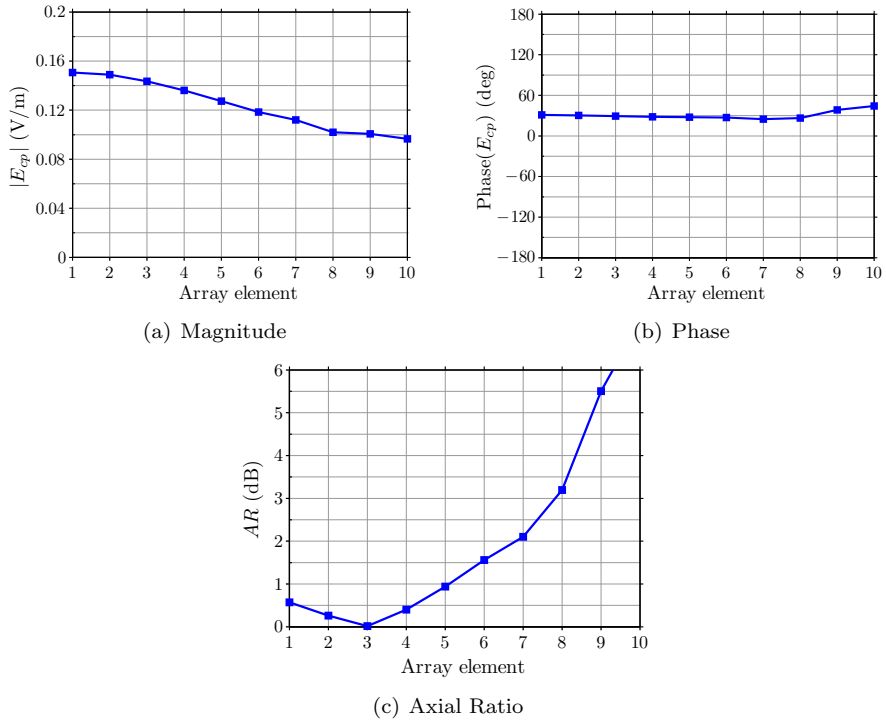
(c) Axial Ratio

Figure 5.16: Magnitude and phase of the copolar component and axial ratio of the electric field radiated by the array elements for the design after complete optimization.
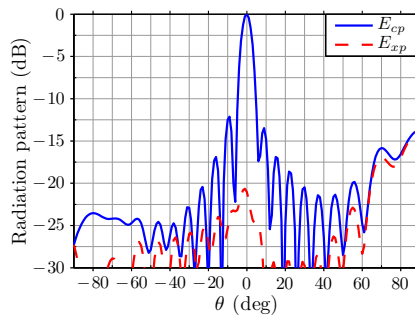
Figure 5.17: Radiation pattern of the design after complete optimization of a 10-element 1-D array.

Element	L_s (mm)	d_a (mm)	d_s (mm)	of (mm)
1	6.799	–	3.916	1.577
2	6.864	18.725	3.897	1.597
3	6.936	18.673	3.892	1.708
4	6.993	18.613	3.867	1.824
5	7.033	18.551	3.817	1.938
6	7.074	18.459	3.747	2.162
7	7.149	18.311	3.687	2.949
8	7.381	17.986	3.684	3.974
9	7.957	17.509	3.851	3.763
10	9.300	16.613	5.821	3.283

Table 5.4: Slot length L_s, array spacing d_a, slot spacing d_s, and offset of values of the array elements for the design after complete optimization.

achieve an axial ratio of the electric field radiated by each element good enough for circular polarization. The steps followed here are those of section 5.3.1.

Fig. 5.15 shows the resulting array, and Table 5.4 contains the values of the parameters of the geometry.

Fig. 5.16(c) shows that the axial ratio of the first elements has gone down, however we did not succeed in improving the axial ratio of the last elements, which is over 3 dB for the last three elements. Even though, an axial ratio of 1.54 dB for the complete array was obtained. Nevertheless, it turned out quite complicated to adjust the phases and magnitudes of each slot of a pair to get a good axial ratio by handling only two parameters, spacing d_s and offset of, specially for the longest ones. That is why it was tried to improve these results by adding a new parameter, so that, as was previously mentioned but not envisaged, now there are two different offsets for the first and second slots of a pair, being of_1 and of_2 respectively.

Results after complete optimization with two offsets
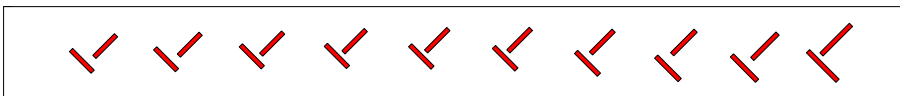
Figure 5.18: Sketch of the design after complete optimization with two offsets of a circularly polarized 1-D slot array.

From the offset values of previous section shown in Table 5.4, they are ascribed to of_1 and of_2. Then, these values are optimized to give a good axial
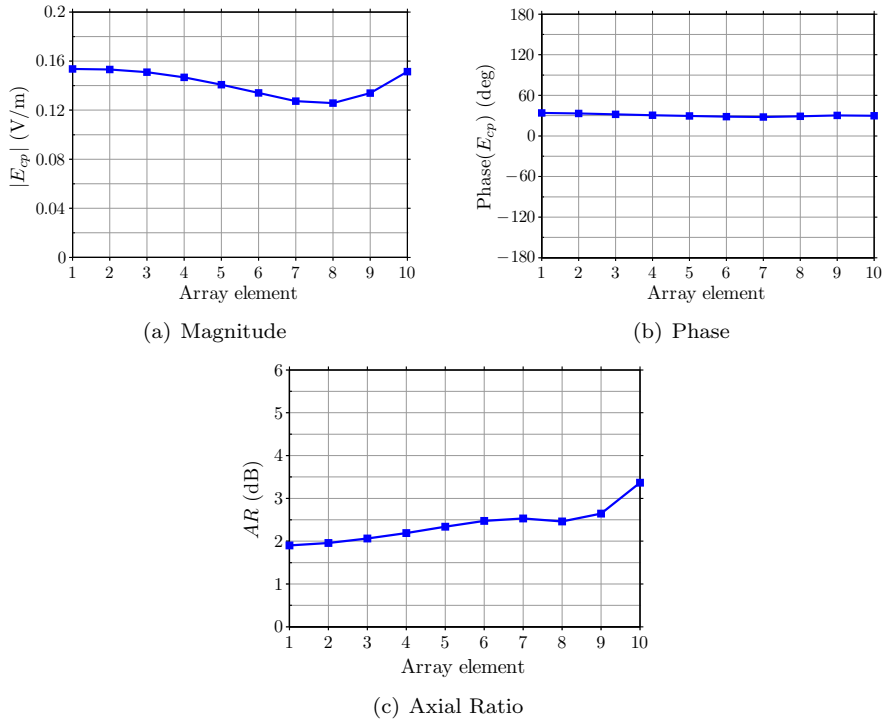
(a) Magnitude

(b) Phase
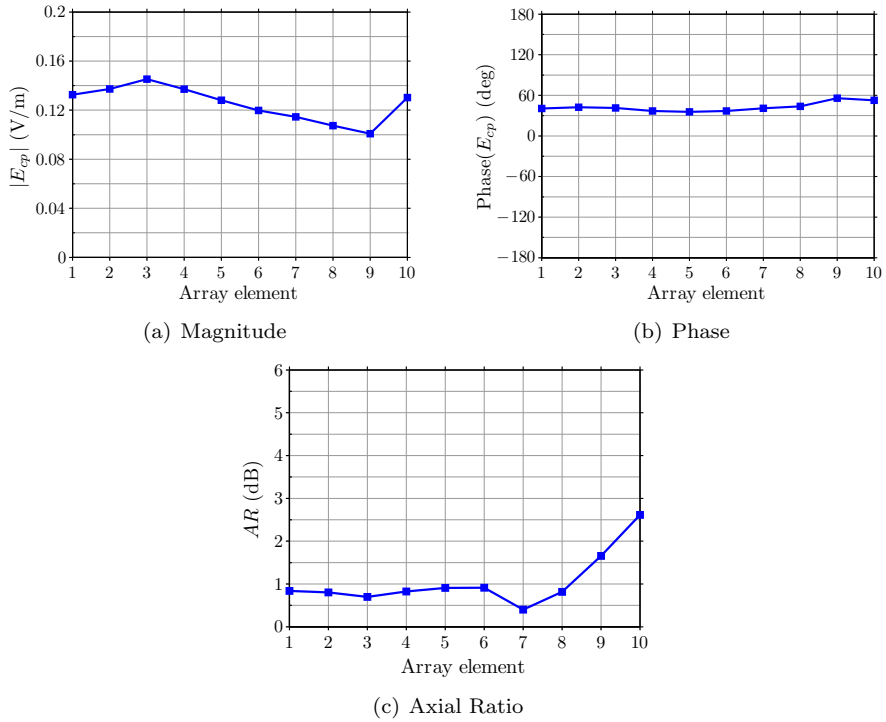
(c) Axial Ratio

Figure 5.19: Magnitude and phase of the copolar component and axial ratio of the electric field radiated by the array elements for the design after complete optimization with two offsets.
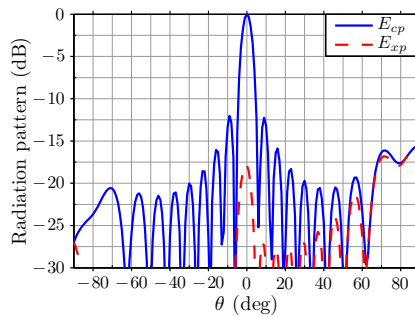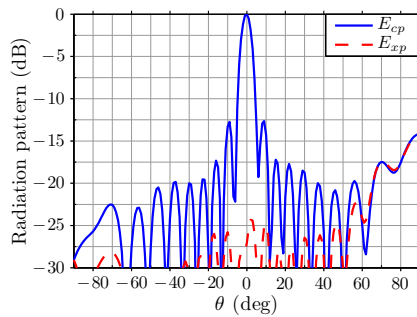

Figure 5.20: Radiation pattern of the design after complete optimization with two offsets of a 10-element 1-D array.

74

Element	L_s (mm)	d_a (mm)	d_s (mm)	of_1 (mm)	of_2 (mm)
1	6.799	–	5.196	2.045	1.217
2	6.864	18.725	5.266	1.709	1.545
3	6.936	18.673	4.518	1.044	1.781
4	6.993	18.613	3.945	0.959	2.318
5	7.033	18.551	3.535	1.069	2.523
6	7.074	18.459	3.202	1.465	2.551
7	7.149	18.311	3.301	2.596	2.125
8	7.381	17.986	3.557	3.700	2.029
9	7.957	17.509	4.528	3.661	1.199
10	9.300	16.613	3.001	3.178	2.661

Table 5.5: Slot length L_s, array spacing d_a, slot spacing d_s, and offsets of_1 and of_2 values of the array elements for the design after complete optimization with two offsets.

ratio for each pair of slots giving rise to the array of Fig. 5.18 whose geometrical parameters are shown in Table 5.5.

Now, the array elements have an axial ratio below -1 dB except for the two last ones, which are below -3 dB (see Fig. 5.19(c)). This results in an axial ratio of 0.78 dB at broadside direction for the complete array (see Fig. 5.20). Therefore, it is clear that the introduction of two offsets for the slots of each pair provides a greater versatility to fulfill antenna specifications. Magnitudes and phases of the array elements are still quite uniform, as shown in Fig. 5.19(a) and Fig. 5.19(b). Nevertheless, this could be improved by repeating the optimization process as many times as was necessary.

5.4 Circularly polarized 2-D array
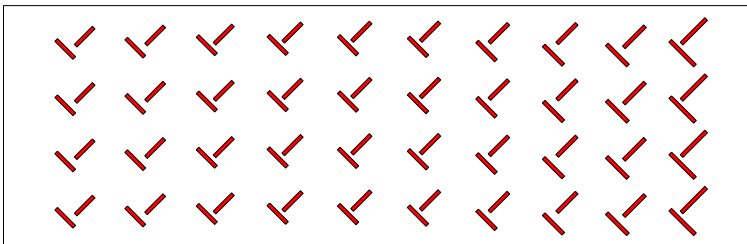
Figure 5.21: Sketch of a circularly polarized 2-D slot array of 4×10 elements.

(a) longitudinal cut

(b) transverse cut
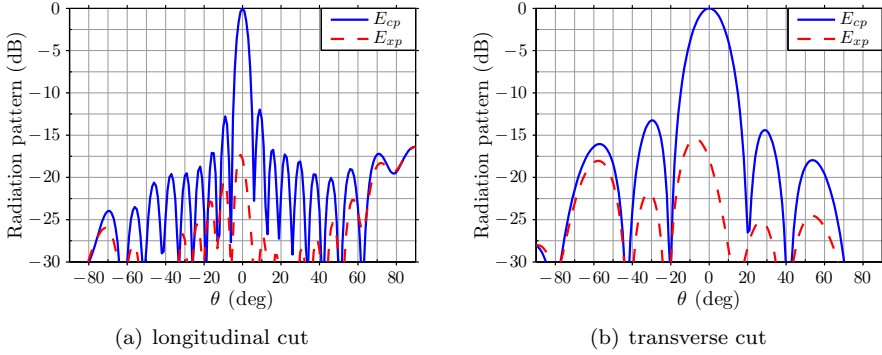
Figure 5.22: Cuts of the radiation pattern of the circularly polarized 2-D slot array.

(a) Directivity
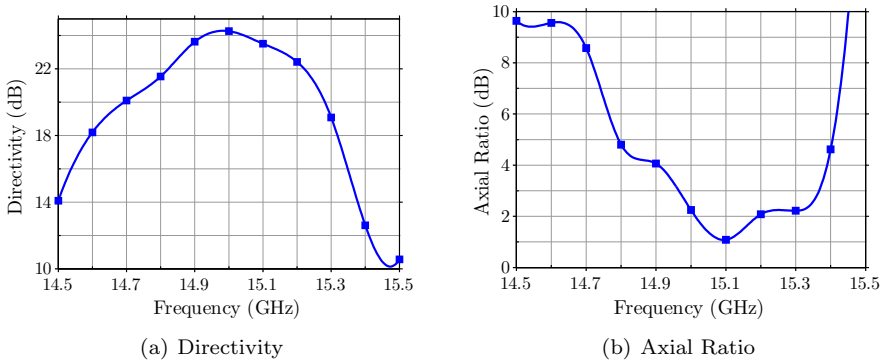
(b) Axial Ratio

Figure 5.23: Directivity and axial ratio vs frequency of the 2-D slot array.

Once the design of a row of slots has been done, the first approximation of a 2-D slot array can be obtained just by repeating this row so many times as it is required. In our case, four rows of slots were considered, as Fig. 5.21 shows. The rows are 0.75λ equally spaced apart.

Fortunately, the results are good enough to avoid any optimization of the whole array, what makes very simple the design of slot arrays on SHW-waveguides. An axial ratio of 2.25 dB at broadside direction is obtained. Fig. 5.22 shows two cuts of the radiation pattern, in longitudinal and transverse directions. Grating lobes below -15 dB can be seen. These results are promising because they confirm the high level of isolation between different rows of slots within the waveguide. In this case, external couplings hardly perturb the performance of the array, thus this first approximation of a planar array is valid as final

design. Nevertheless, an optimization process similar to that one described in section 5.3.2, but considering now all the elements of the 2-D array, could be carried out to fulfill more restrictive antenna specifications.

Directivity and axial ratio as a function of frequency are shown in Fig. 5.23. The calculations were done at the frequencies marked with icons.

Chapter 6

Quasi-TEM waveguides based on AMC surfaces: RGWs

6.1 Introduction

The single hard wall waveguide (SHWW) was originally conceived to feed a slot array. As it has already shown in previous chapters, this waveguide has unique properties. Even though the waveguide is oversized in one dimension it can support a single global quasi-TEM mode and also several degenerate local quasi-TEM waves with the same phase velocity.

   The single hard wall waveguide consists of an oversized rectangular metal waveguide or parallel-plate waveguide with the bottom metal plate replaced by a hard surface. The idea of using a hard surface as the bottom surface comes from the observation of how fields propagate within a parallel-plate waveguide (PPW) (see Fig. 6.1). On the one hand, a vertical electric field propagates freely between two parallel metal plates or PEC plates regardless of the distance between them. On the other, all modes are below cut-off between a PEC plate and a PMC plate provided the distance between the plates is smaller than $\lambda/4$. Thus, by using a hard surface (ideally, a PEC/PMC strip grating) and a parallel PEC plate separated by an air gap smaller than $\lambda/4$, it is possible to combine both performances depending on the direction of propagation, so that this waveguide works like a PEC-over-PEC PPW in the longitudinal direction, favoring vertically polarized waves, whereas it works like a PEC-over-PMC PPW (with $h < \lambda/4$) in the direction transverse to the strips suppressing any kind of propagation.

(a) PEC-over-PEC PPW   (b) PEC-over-PMC PPW

Figure 6.1: Field propagation between two parallel-plate waveguides. Above, waveguide cross-section. Below, top view of the waveguide excited by a punctual source.

The previous idea was also inspiration for a new metamaterial-based waveguide technology specially appropriate for millimeter and sub-millimeter waves comes up. This new technology, so-called ridge gap waveguide (RGW), was first introduced in [140]-[142]. This waveguide is made between two parallel metal plates. One of them is made of a texture to create a high impedance condition at the surface (ideally, a PMC boundary), and therefore to impose a cut-off for the parallel-plate modes. In between the bed of nails there are metal ridges to guide the waves along a particular path. Thereby, the waveguide is formed in the gap between the ridge and the metal plate on top, as illustrated in Fig. 6.2.
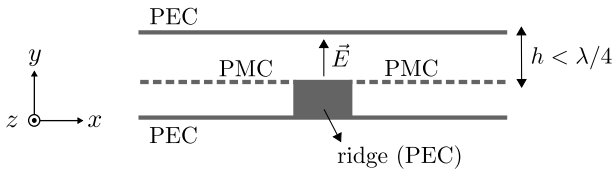
Figure 6.2: Cross section of a canonical ridge gap waveguide, with a ridge surrounded by a high impedance surface (ideally, a PMC surface).

Both waveguiding structures, the SHWW and the RGW, can guide local quasi-TEM waves. However, the waves are forced to follow straight paths within the SHWW since they must go parallel to the corrugations. Whereas, for the RGW the waves have to follow metal ridges, which can bend, split, make corners, etc. Therefore, the RGW is a more versatile structure than the SHWW to make high-frequency circuits.

The key factors of this new waveguide technology can be enumerated as follows:

- low losses, since gap waveguides do not require dielectrics and they can be completely realized with metal, actually, losses are comparable to those of rectangular waveguides [143],

- low cost, as there is no need for any conducting joint between the two plates, what makes the manufacturing easier,

- large bandwidth, indeed bandwidths larger than one octave appear possible [144],

- no packaging trouble, because gap waveguides can be designed to be completely enclosed, without the presence of cavity modes, which also makes it an attractive packaging technology as it has already been demonstrated for microstrip circuits [145],

- easy integration of active components like amplifiers and Monolithic Microwave Integrated Circuits (MMIC) because shielding and packaging are more or less automatically provided by the gap waveguide itself.

All these factors make the gap waveguide advantageous relative to existing high-frequency transmission lines, such as microstrip or coplanar waveguides, and hollow metal waveguides. One one hand, microstrip or coplanar waveguides need dielectrics and in consequence suffer from losses with increasing frequency, they have limited power handling capability, and spurious resonances when encapsulated. On the other, conventional hollow waveguides are realized in two parts, which have to be joined together, what increases its manufacturing cost, especially at high frequencies when the sidewalls become thinner and thinner. Thus, this new technology seems to be an interesting transmission line for realizing components and circuits from a frequency around 30 GHz, when the current technologies already exhibit some deficiencies, up to 100 GHz. A design and verification of ridge gap waveguide in bed of nails is reported in [146].

Substrate integrated waveguides (SIW) are widely used for high-frequency applications [59],[31], but still exhibit losses due to substrate at increasing frequencies. Other attempts to make metamaterial-based waveguides can be found in [147], [148]. However, these solutions make use of wave propagation inside the metamaterial or at the surface of it, both of which cause losses and dispersion.

This chapter starts with a description of the structure and operation of the ridge gap waveguide followed by a numerical analysis. Then, a study of the characteristic impedance of the waveguide is done in order to characterize it as a transmission line. And finally, a collection of circuits, in particular a power splitter and a coupler, are designed.

6.2   Structure and operation

The basic geometry of the ridge gap waveguide comprises two parallel conduct-
ing surfaces. One of the surfaces is provided with a texture that is used to
realize conducting ridges surrounded by a high impedance surface. The new
waveguide is located in the gap between metal surfaces. The gap is usually
filled with air, but it can also be dielectric-filled, and its size should be smaller
than $\lambda/4$. The textured surface stops waves in all directions (provided the wa-
veguide height is low enough) in such a way that the waves have to follow the
metal ridges.

   A metal parallel-plate waveguide with $h < \lambda/2$ can only guide vertically
polarized TEM waves in any direction without any low-frequency cut-off. These
TEM waves span throughout the whole waveguide, thus they are global parallel-
plate modes. Whereas, the quasi-TEM waves of a ridge gap waveguide are local
waves following one ridge. If the global parallel-plate modes are present in this
waveguide, they will destroy the local gap waveguide performance completely.
Therefore, it is crucial for the performance of the ridge gap waveguide that all
kinds of global parallel-plate modes are prohibited from propagating. This is
achieved by texturing the metal surface on both sides of the ridge in such a way
that it gets high surface impedance and provides cut-off for the global parallel-
plate modes within a certain frequency band. A bed of nails or a Fakir's bed
has been chosen to realize the high impedance surface because it can mimic an
ideal impedance boundary [125], meaning that the surface impedance does not
depend much on the angle of incidence in the vertical plane. This bed of nails
is formed by metal pins standing vertically over a ground plane. The depth
or height of the pins, d, should be approximately $\lambda/4$ to transform the ground
plane (PEC plate) to a high impedance surface (ideally, a PMC plate).

   The characteristics of the ridge gap waveguide can be seen from its disper-
sion diagram. Assume a ridge gap waveguide (see Fig. 6.3) having a uniform
pin surface whose pins are square of width $t = 2.5$ mm, period $p = 6.5$ mm,
and depth $d = 5$ mm ($\lambda/4$ at 15 GHz). The ridge has same depth as the pins
have, and ridge width is $w = 5.2$ mm. The gap between the ridge and the PEC
plate on top is $h = 1$ mm. The waveguide is 48.2 mm wide and sidewalls are
PEC. The waveguide width has been taken considering only three rows of pins
at each side of the ridge, what is enough for the calculations because field de-
cays very rapidly beyond the ridge. The diagram in Fig. 6.4 has been obtained
using the Eigenmode solver of CST, and it shows a set of rectangular wave-
guide type modes appearing below 10 GHz. They have a lower cut-off similar
to normal rectangular waveguide modes, but go into a stopband at 10 GHz
approximately, and appear again at the end of this stopband, around 20 GHz.
Inside the whole stopband there is only one mode very close to the light line.
This is the desired local quasi-TEM mode following one ridge. Therefore, it can

(a) Perspective view

(b) Cross section

(c) Top view of one period of pins
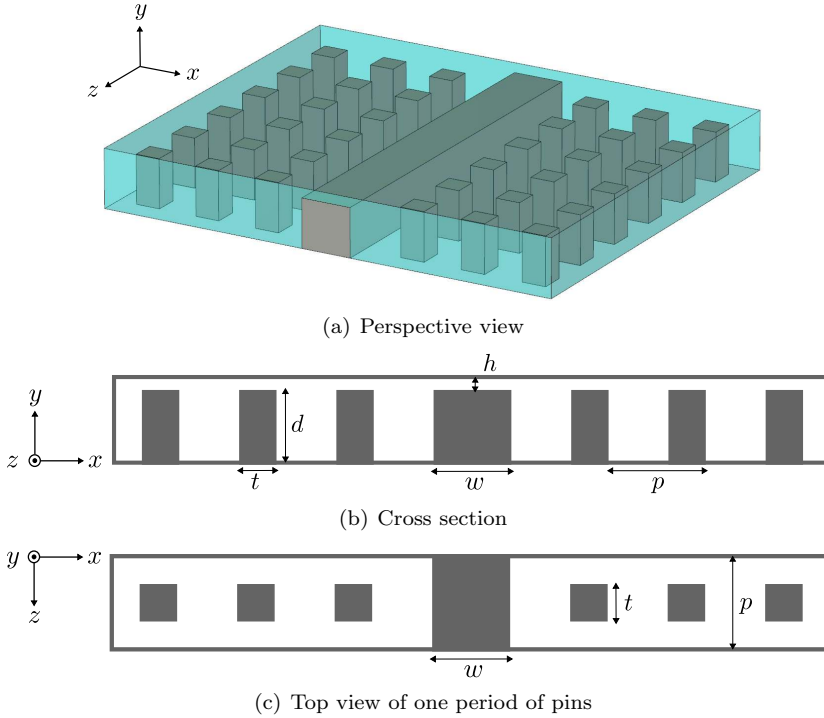
Figure 6.3: Geometry of the ridge gap waveguide in bed of nails.

be said that the bandwidth of the ridge gap waveguide, i.e. the frequency band where the waveguide works as expected, is nearly the unimodal band within which only one quasi-TEM mode is present.

An approximate analytical modal solution of the ridge gap waveguide was recently obtained and published in [149] and [150] where closed form expressions for the characteristic impedance can also be found. Here, they proved that the stopband of the bed of nails parallel-plate waveguide is hardly modified when the ridge is included. Thus, in general the upper limit of the unimodal band coincides with the upper frequency of the stopband of the parallel-plate structure. Nevertheless, they found that for ridge width not so small the first higher order mode over the ridge may have a cut-off within the bed of nails parallel-plate stopband, so that the cut-off frequency of this mode is the one that sets the upper limit of the unimodal band. This is the case, indeed, for the dispersion diagram of Fig. 6.4. The mode with the cut-off frequency below 20 GHz is inside the stopband (10 - 23 GHz approximately) and corresponds to

the first higher order mode appearing over the ridge. This mode is associated
with an odd transverse variation along the ridge.
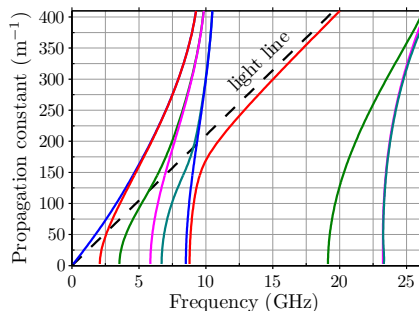
Figure 6.4: Dispersion diagram in the ridge direction of a RGW in bed of
nails.

6.3   Analysis

A numerical analysis of a ridge gap waveguide using CST Microwave Studio
has been done in this section to show its propagation properties. The ridge gap
waveguide in bed of nails analyzed here has the same parameters as those used
before for the calculation of the dispersion diagram. The physical parameters
of the waveguide were chosen to get a wide bandwidth. The most critical
parameter is the gap height, which sets the upper limit of the band. Except
for the pin depth, the parameters of the pin surface do not affect much the
bandwidth provided that they are kept electrically small. Nevertheless, a study
determining the cut-off frequencies as a function of the geometrical parameters
of the periodic surface, including the pin surface, and the ridge width, has
already been reported in [145], [151]. It has been obtained also analytical
formulas for the lower and upper cut-off frequencies of the stopband of the
pin surface [152], but these are only valid asymptotically for small period. In
principle and for small periods, the pin surface works as a PMC when they
are approximately $d = \lambda/4$ long, and they will provide a stopband from this
frequency to a frequency at which $d + h = \lambda/2$, where h is the height of the air
gap.

The dispersion diagram provides information about the bandwidth of the
ridge gap waveguide, however its calculation is a quite time-consuming task.
In order to get a fast estimation of the bandwidth, a way of characterizing
the RGW similar to that used for the single hard wall waveguide in section
2.2.3 is followed here. It is based on the study of the local quasi-TEM wave

following one ridge. This characterization represents a way of determining its bandwidth and it may be useful for optimizations. For the sake of comparison, we first analyze the ideal model of a ridge gap waveguide. This model consists of a metal strip (which plays the role of a ridge) surrounded by an ideal PMC surface, and leaving an air gap above them there is a PEC plate. Then, the analysis of a realization of the ridge gap waveguide, where the ideal PMC is replaced by a bed of nails, is performed.

Let us consider a waveguide 100 mm wide and 240 mm long. An excitation source is placed close to one end of the guide, and the whole structure is provided with an absorbing boundary condition around its rim. The source probe excites a local quasi-TEM mode that propagates along the metal ridge. To study the confinement of the local quasi-TEM wave, we calculate the coupling from the excitation probe to field probes (see Fig. 6.5) located at the top PEC surface at two positions corresponding to the cut-off region (H_{x2}, H_{z2} probes) and to the propagation region (H_{x1} probe). The propagation region is over the ridge and the cut-off region is the remaining region beyond the ridge. The objective is then to maximize the coupling in the propagation region and minimize the coupling in the cut-off region over the same frequency range. As we pointed out in section 2.2.3, it may also be useful for optimizations of the geometry to establish performance thresholds that represent a certain level of quality of such a waveguide. In order to establish such thresholds, we computed the fields at the two specified locations and normalized these values to the field values at the central H_{x0} probe.
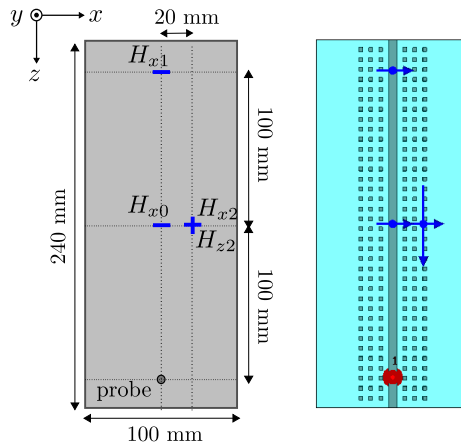
Figure 6.5: Dimensions of the waveguide and locations of the source and field probes used for the analysis.

6.3.1 Ideal gap waveguide

First the ideal model of a ridge gap waveguide is analyzed. The metal strip guiding the quasi-TEM wave is placed on an ideal PMC surface. Above it, a metal plate is located in such a way that there is an air gap between the plate and the strip. Fig. 6.6(a) shows the three field values at the three H-field probes shown in Fig. 6.5 after being normalized to the field values at the central H_{x0} probe. As it is expected a maximum coupling in the propagation region and no coupling in the cut-off region are obtained over the whole frequency band used for the analysis, since an ideal PMC surface has infinite bandwidth. Transverse and longitudinal components of H-field distribution, evaluated at the top PEC plate, are shown in Fig. 6.6(b) for some frequencies. It is seen that a local quasi-TEM wave very confined to the ridge propagates over the whole frequency band.
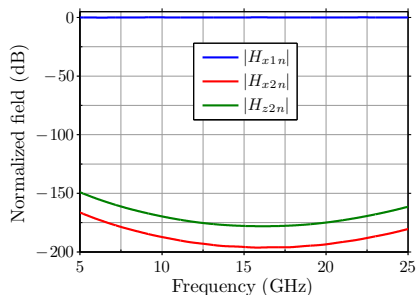
(a) Field measured at propagation and cut-off regions as a function of frequency
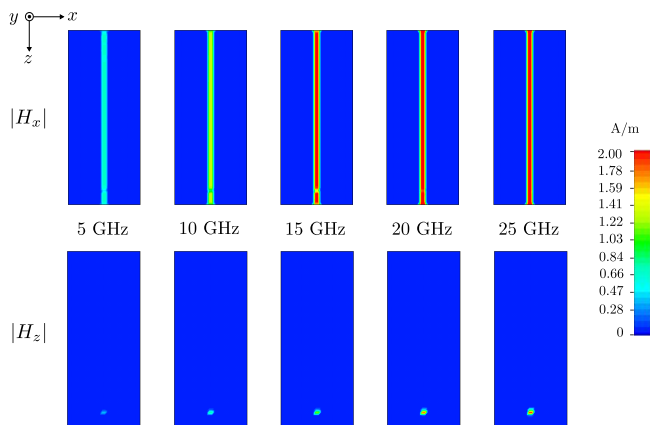
(b) $|H_x|$ and $|H_z|$ at different frequencies

Figure 6.6: Numerical analysis of the ideal model of a ridge gap waveguide.

6.3.2 Ridge gap waveguide in bed of nails

Now the ridge gap waveguide in bed of nails is analyzed. The geometrical parameters of the ridge and the pin surface were previously written. As it is already known, the metal ridge guiding the quasi-TEM wave is surrounded by a bed of nails to create a cut-off for the parallel-plate modes, and a metal plate is located above them leaving an air gap between the top plate and the ridge to guide the waves along it. Remarkably, only a few rows of pins are needed to guide the waves along the ridges. Three rows of pins at each side of the ridge have been considered here enough for the calculations, since adding more rows of pins do not cause any effect on the results.
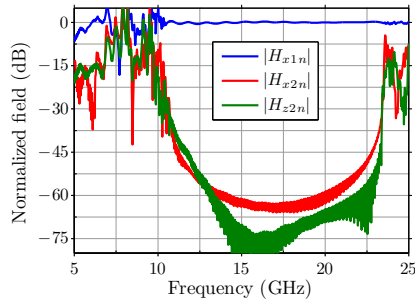
(a) Field measured at propagation and cut-off regions as a function of frequency
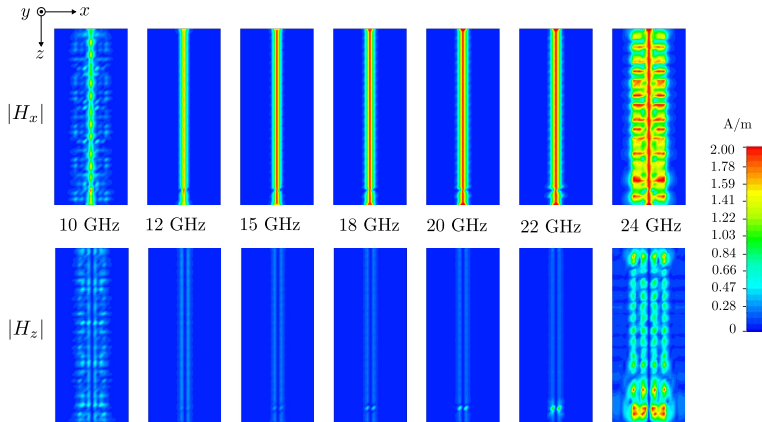
(b) $|H_x|$ and $|H_z|$ at different frequencies

Figure 6.7: Numerical analysis of a ridge gap waveguide in bed of nails.

Fig. 6.7(a) shows the three field values at the three H-field probes shown in Fig. 6.5, after being normalized to the field values at the central H_{x0} probe.

We see that within a certain frequency band, the transmitted field over the ridge has an almost constant level and the transmitted field beyond the ridge is negligible, which means that the wave is confined to the ridge. A small ripple is appreciated in the transmitted field, which is either due to reflections at the termination at the end of the guide, or due to computational accuracy. The useful frequency band is 10-23 GHz approximately, so that one octave bandwidth appears possible. This is shown in Fig. 6.7(b) as well, where field distribution plots evaluated at the top metal plate are shown.

(a) 11 GHz

(b) 17 GHz

(c) 23 GHz
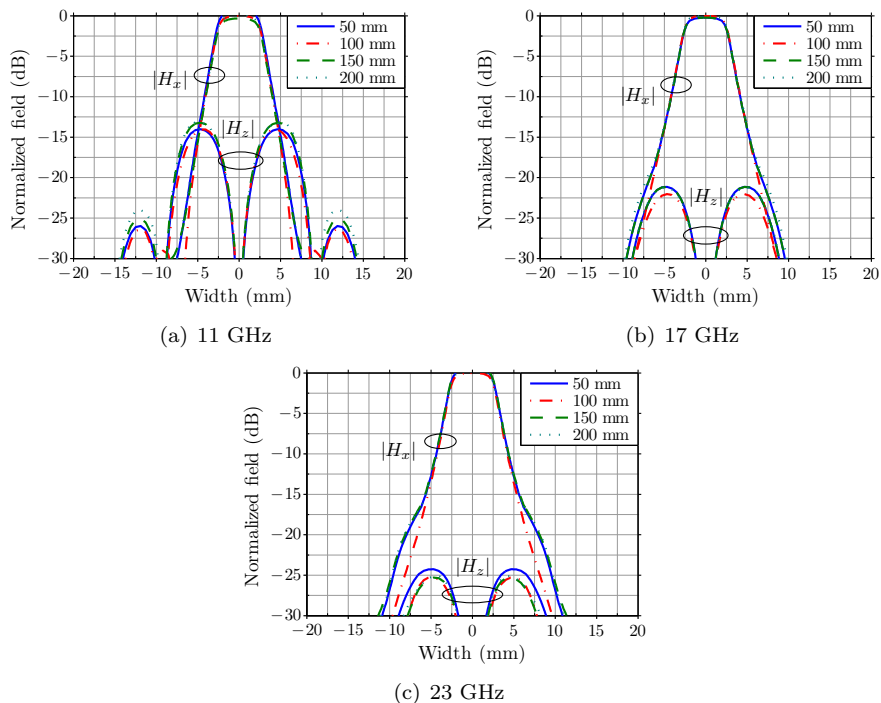
Figure 6.8: Field computed at several cross sections of the waveguide and at different frequencies.

It is worth noticing that this frequency band coincides with the stopband of the bed of nails parallel-plate instead of the unimodal band of the dispersion diagram of Fig. 6.4. This is due to the fact that the upper limit of the unimodal band is set by the cut-off frequency of the first higher order mode appearing over the ridge. Since this mode has an odd symmetry and therefore a field of zero value at the center of the ridge where the source is located, it has not been excited here, but it could be excited in experimental realizations. Nevertheless,

the bandwidth could be enlarged by stretching the ridge width in order to make the cut-off frequency of the higher order mode coincident with the upper limit of the bed of nails parallel-plate stopband.

Finally, to study how fast the quasi-TEM beam decays beyond the ridge borders and check whether there are losses along the ridge, both transverse and longitudinal components of the magnetic field are depicted in Fig. 6.8. These field components were taken at the top plate, on transverse sections of the waveguide at several distances from the source (50, 100, 150, 200 mm). Note that only a central part of the waveguide is visualized in Fig. 6.8 since fields beyond this region are negligible. As it can be seen, the confinement of a quasi-TEM wave is maintained along the ridge and there is almost no dispersion in the working frequency band. No losses can be appreciated from the simulations. The performance is very similar for these three frequencies, what confirms a bandwidth larger than one octave. Nevertheless, there is a significant difference in the level of H_z, about 10 dB, between the lower and the upper frequency. The H_z component is lower at higher frequencies.

In conclusion, the results prove the presence of a quasi-TEM wave confined to the region above the ridge in the air gap between the two plates for a bandwidth higher than one octave.

6.4 Characteristic impedance

To be able to design circuits in a new waveguide technology is essential to characterize it as a transmission line and therefore to know its propagation constant and characteristic impedance. The presence of a quasi-TEM propagation within one octave bandwidth has already been proved in the previous section and published in [144]. This section presents a study of the characteristic impedance of a RGW. This work can also be found in [153] and [154].

6.4.1 Approximate formulas

First, it was tried to find similarities between the RGW and other classical transmission lines, so that we could use the formulas for the characteristic impedance of the latest as a first approximation to the characteristic impedance of a RGW. For that, it is more convenient to consider the ideal model of a RGW, i.e., the PEC-over-PMC ridge gap waveguide. It consists of a metallic strip instead of the ridge directly on a PMC surface and a PEC plate above them that creates an air gap of less than $\lambda/4$. Looking at Fig. 6.9 it is clear the similarity between the ideal gap waveguide and the stripline. The stripline has a PMC-type symmetry plane in the middle of the gap, what makes it look like two opposite gap waveguides, one being the image of the other. Thus, the gap waveguide is a sort of half stripline, what means that we can use the formulas

for striplines in order to determine the characteristic impedance of the ideal gap waveguide and the approximate performance of realized ones.

(a) Ideal gap waveguide   (b) Stripline
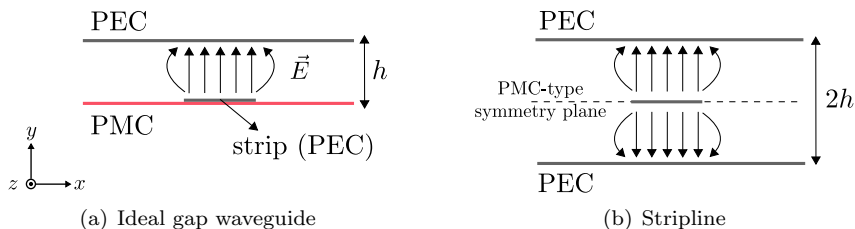
Figure 6.9: Ideal gap waveguide and stripline models.

Thereby, the characteristic impedance of the ideal gap waveguide is given by

$$Z_{gap\,waveguide} = 2Z_{stripline} \tag{6.1}$$

where $Z_{stripline}$ can be found in [155] to be

$$Z_{stripline} = \frac{\eta}{4} \left(\frac{W_e}{2h} + 0.441 \right)^{-1} \tag{6.2}$$

with

$$\frac{W_e}{2h} = \frac{W}{2h} - \begin{cases} 0, & W/(2h) > 0.35 \\ (0.35 - W/(2h))^2, & W/(2h) \leq 0.35 \end{cases} \tag{6.3}$$

This formula gives an accurate value of the characteristic impedance of an ideal gap waveguide, however it is not enough accurate for practical realizations of the PMC surface.

6.4.2 Numerical approaches

Since the previous formula is only valid for the ideal gap waveguide, the characteristic impedance of a ridge gap waveguide in bed of nails should be obtained numerically. But the computation is not so immediate, what is due to the periodical nature of the structure. The presence of metal pins makes this waveguide periodic along the direction of propagation. Commonly, commercial electromagnetic simulators make use of waveguide ports to excite transmission lines. E.g., CST computes the modal field and gives the line impedance for every mode at a chosen frequency. But unfortunately, this computation is only valid for waveguides of constant cross section, like the ideal gap waveguide.

Therefore, since CST cannot handle ports in waveguides with a longitudinal periodicity, we have to resort to the electromagnetic theory and impedance definitions to calculate the characteristic impedance numerically from the propagated fields within the waveguide. Two numerical approaches have been used.

First approach

The first approach employs the following definition for the characteristic impedance

$$Z = \frac{V}{I} \tag{6.4}$$

where,

$$V = \int E_y \, \mathrm{d}y \tag{6.5}$$

$$I = \int H_x \, \mathrm{d}x \tag{6.6}$$

V and I are calculated in a cross section. V is the voltage obtained as the field integral of the vertical component of the electric field E_y along a straight vertical line that links the center point of the ridge with the metal plate on top. I is the current obtained as the field integral of the horizontal component of the magnetic field H_x along a straight horizontal line on the upper metal plate that goes from side to side of the waveguide.

Second approach

The second approach employs the following definition for the characteristic impedance

$$Z = \frac{P}{|I|^2} \tag{6.7}$$

where,

$$P = \iint_S \left(E_x H_y^* - E_y H_x^* \right) \mathrm{d}S \tag{6.8}$$

P and I are calculated in a cross section S. P is the power obtained as the surface integral of Poynting vector given by (6.8). And I is obtained as above.

We have used both approaches to calculate the characteristic impedance of real and ideal ridge gap waveguides. It is observed that both methods provide almost the same results for the ideal PMC-type gap waveguide, what proves the validity of the methods employed. However, there is a difference between the results of the two methods for a real ridge gap waveguide realized by a

bed of nails. This difference is due to the quasi-TEM mode, which behaves more like a waveguide mode than the clean TEM mode of the ideal PMC-type gap waveguide. E_y and H_x are the desired field components of the quasi-TEM mode. The quasi-TEM mode has also weak non-desired field components (E_x, H_y) that are not taken into account with the first approach. Thus, we should consider the second approach provides more accurate results.

Still, the first approach is useful to give a first approximation. But its accuracy will depend on how constant is the field across the ridge, since there is not a unique definition for V, which could have been calculated as a line integral along any vertical line joining the ridge and the top metal plate, and also on the purity of the quasi-TEM mode.

6.4.3   Results

In this section, we include results for the characteristic impedance of real and ideal ridge gap waveguides. Numerical results showing the variation of the characteristic impedance with ridge width or gap height as well as frequency response and periodical behavior along the propagation direction have been obtained.

Let us consider for the calculations the ridge gap waveguide of section 6.3 with dimensions: $h = 1$ mm, $d = 5$ mm, $w = 5.2$ mm, $t = 2.5$ mm, $p = 6.5$ mm. The waveguide can be as many wavelengths wide as desired and its left and right sides can be left open since walls are not required to support the modes. Three rows of pins at each side of the ridge are considered, what is enough for the calculations.

First, the ideal PMC-type ridge gap waveguide is analyzed as a reference. The values of the characteristic impedance are shown in Table 6.1. We see that the values obtained numerically with both approaches, and the line impedance at the waveguide ports given by CST, agree well with the stripline approximation. As said previously, this fact confirms the validity of the methods employed.

	$Z_c(\Omega)$
Stripline approximation	62
Waveguide port (CST)	61
First approach: V/I	61.3
Second approach: P/I^2	62.3

Table 6.1: Characteristic impedance for the ideal PMC-type ridge gap waveguide using different methods.

Next, the real ridge gap waveguide in bed of nails is analyzed. Frequency variation of the characteristic impedance calculated by using both numerical

approaches is depicted in Fig. 6.10. The calculation was done at frequencies marked with icons. The stripline approximation of the ideal gap waveguide has been plotted as a reference. It is observed that the values obtained with both approaches are quite similar, and they are below the stripline approximation in a wide frequency band. It can be appreciated that the characteristic impedance varies with frequency slightly within the working band, whereas it undergoes big changes out of it.
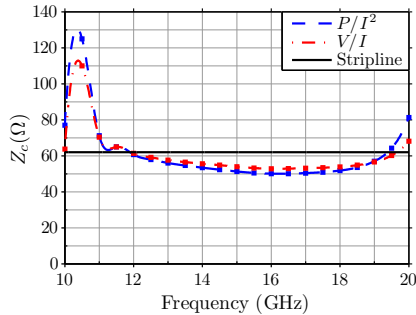
Figure 6.10: Characteristic impedance of a RGW as a function of frequency.

Table 6.2 contains characteristic impedances calculated at different cross sections ($z = z_1, z_2, z_3, z_4$) along the waveguide within one period, and at several frequencies. It is clear from the results that due to the periodical nature of the structure along the direction of propagation, the behavior of the characteristic impedance along it is periodic as well. Fortunately, it is not very significant.

	$Z_c(\Omega)$			
	z_1	z_2	z_3	z_4
12 GHz (P/I^2)	57.5	54.5	53.5	57.6
12 GHz (V/I)	60	58.8	58.1	59
15 GHz (P/I^2)	50.2	48.2	47.2	50.9
15 GHz (V/I)	53.5	53	52.6	54.3
18 GHz (P/I^2)	47.9	44.4	43.2	48.6
18 GHz (V/I)	51.9	49.6	49	52.7

Table 6.2: Characteristic impedance obtained at several cross sections within one period by using both numerical approaches and for different frequencies.

The variation of the characteristic impedance with ridge/strip width has been depicted in Fig. 6.11(a). We see that the range of values for the characteristic impedance is larger for the ideal PMC-type ridge gap waveguide (stripline

approximation) than for the realized ridge gap waveguide, even though, values above 100Ω can also be obtained for the real case. As expected, the larger ridge/strip width is, the lower the characteristic impedance is.

Finally, Fig. 6.11(b) shows the evolution of the characteristic impedance with gap height. Concerning the range of values, we extract the same conclusion as in Fig. 6.11(a). But now, the larger the gap height is, the higher the characteristic impedance is, up to a point in which the gap height is close to a quarter wavelength, i.e., 5 mm for this case. From this point up, there is no cut-off for the parallel plate modes and the waveguide does not work as a transmission line.

To point out that the characteristic impedance is closer to the stripline approximation for large ridge widths and small gap heights. This is due to the fact that the larger ridge width over gap height ratio is, the more confined are fields over the ridge and the more pure is the quasi-TEM mode, so that the real gap waveguide behaves more like the ideal one.

(a) Z_c vs W

(b) Z_c vs h
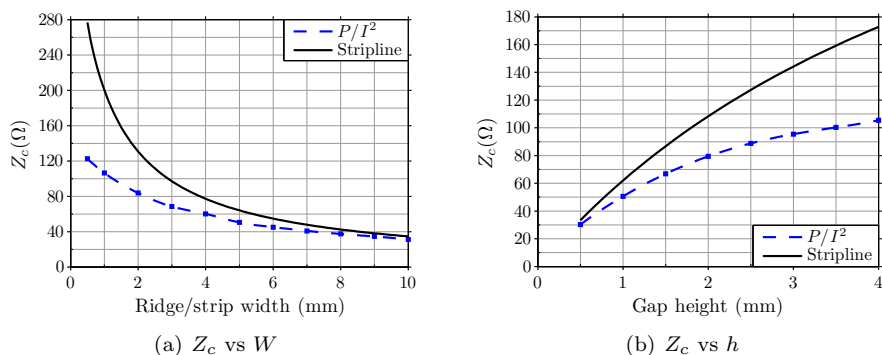
Figure 6.11: Evolution of the characteristic impedance of a RGW with ridge/strip width and gap height.

6.5 Microwave circuits

Once a ridge gap waveguide in bed of nails has been characterized, we can design circuits in ridge gap waveguide in the same way as we do it in microstrip technology, for instance.

This section shows the performance of some microwave circuits in ridge gap waveguide technology, in particular a power splitter and a coupler [154],[156]. Numerical results as well as measurements demonstrate good performance within a wide frequency band. Even though this technology is particularly

interesting for millimeter and submillimeter-wave bands, initial developments have been done in the microwave band for the sake of simplicity during the manufacturing stage.

6.5.1   Power divider

A power divider at 15 GHz was designed and manufactured. A line with impedance $Z_0' = Z_0/\sqrt{2}$ and length $3\lambda/4$ at 15 GHz was selected as matching network. A length longer than $\lambda/4$ was chosen in order to have more than a period of nails along the line. A 50Ω coaxial-to-ridge transition was designed with HFSS simulator. Fig. 6.12 shows the manufactured prototype of the power divider designed in ridge gap waveguide.
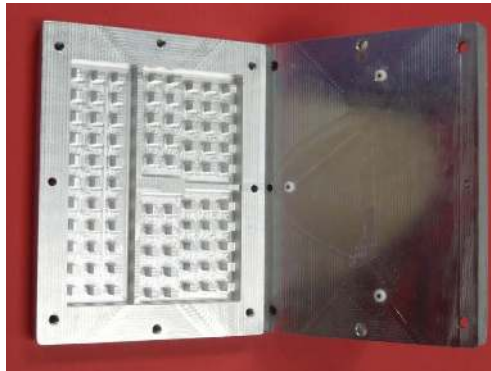
Figure 6.12: Prototype of the power divider in ridge gap waveguide technology.

For the purpose of comparison a power divider in stripline technology has been analyzed using Microwave Office simulator. Fig. 6.13(a) shows simulated S parameters for the ridge gap waveguide divider (dashed lines) and stripline divider (continuous lines). The agreement is reasonably good.

Measurements of the power divider in ridge gap waveguide were made with a Network Analyzer using an APC-3.5 mm calibration kit. The HFSS simulations (dashed lines) and the measurements (continuous lines) have been plotted in Fig. 6.13(b). Good agreement between simulations and measurements can be observed at 15 GHz. Return loss are lower than -15 dB while insertion loss is around 4 dB.

(a) RGW / stripline simulations   (b) RGW simulations / measurements
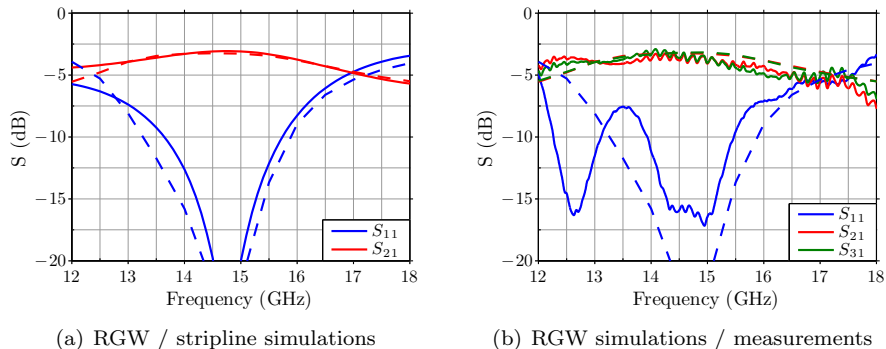
Figure 6.13: Simulated and measured S parameters of a power divider in
RGW and stripline technologies: a) RGW (dashed lines) and stripline
(continuous lines) simulations; b) RGW simulations (dashed lines) and RGW
measurements (continuous lines).

6.5.2   Couplers

Next, two couplers in ridge gap waveguide technology are presented. As a
first example a typical branch line coupler was designed at 15 GHz. Lines of
$3\lambda/4$ were used. A ridge of width $w = 2$ mm was chosen as the reference line.
A transition between a 50Ω coaxial probe and this ridge was designed using
HFSS. Fig. 6.14 shows a photo of the constructed prototype.

Figure 6.14: Prototype of the branch line coupler in ridge gap waveguide
technology.

Fig. 6.15 shows simulated total electric field at the top of the ridge. The
directional aptitude can be noted.
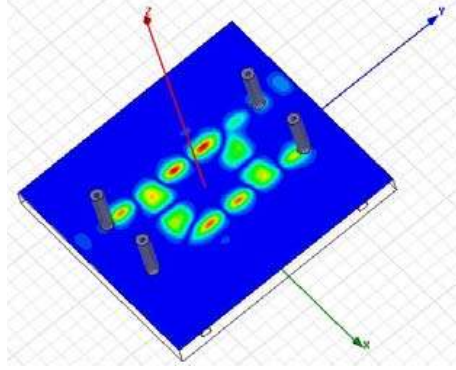
Figure 6.15: Electric field at 15 GHz in the branch line coupler in RGW.

(a) Simulated / measured S parameters

(b) Coupled branch phase difference
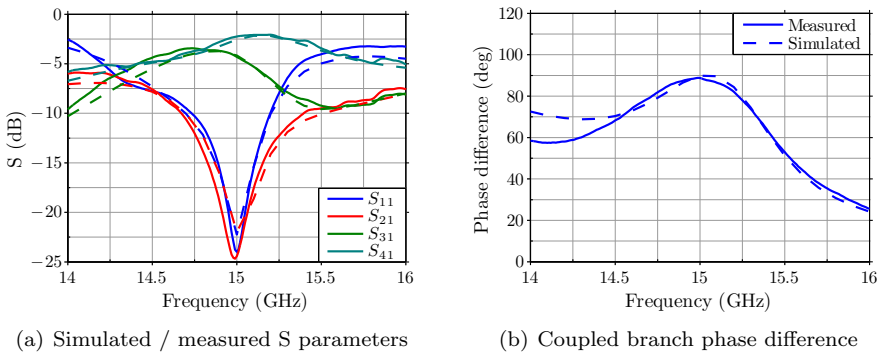
Figure 6.16: Simulated and measured S parameters of a branch line coupler in
RGW: a) Simulated (dashed lines) and measured (continuous lines)
magnitude of S parameters; b) coupled branch phase difference.

Measurements were made with a Network Analyzer using an APC-3.5mm
calibration kit. Fig. 6.16 shows the HFSS simulations and the measurements.
The magnitude of S parameters are shown in Fig. 6.16(a) where a good agree-
ment between simulations and measurements can be observed around 15 GHz.
Return loss are lower than -24 dB at 15 GHz while insertion loss in the coupled
branches are 2.2 dB and 4.2 dB. A bandwidth of 3% has been measured with
a threshold of -10 dB in S_{11} parameter. In this bandwidth a phase difference
between 81° and 89° has been measured, as it is shown in Fig. 6.16(b).

A second example is a coupled-line directional coupler. Fig. 6.17 shows
the geometry of the proposed coupler. Changing coupling length, ridge width
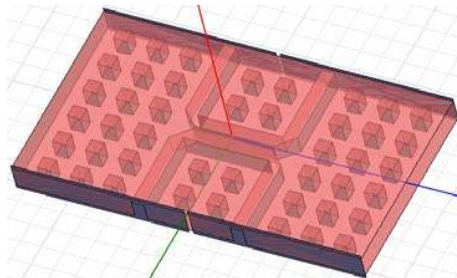
Figure 6.17: HFSS schematic of the coupled-line directional coupler in RGW.

and distance between ridges, it is possible to get some encouraging results. In
Fig. 6.18 the S parameters obtained with HFSS simulator are shown. Note
that isolation higher than 23 dB and directivity around 20 dB at 14 GHz can
be obtained. It is interesting to point out that 3 dB coupling can be obtained
with a mechanically feasible distance between ridges.
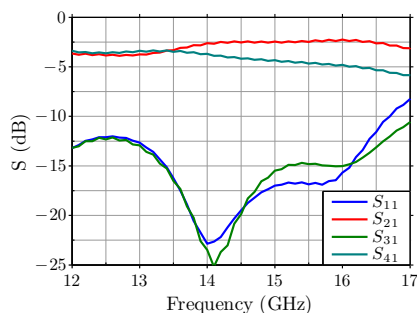
Figure 6.18: S parameters of a coupled-line directional coupler in RGW
obtained with HFSS.

To sum up, some microwave circuits have been designed in ridge gap wave-
guide technology showing good performance not only in simulations but also in
measurements. The circuits chosen can be useful to design more complex cir-
cuits, like microwave filters and corporate feeding networks for array antennas,
in future.

This chapter has presented recent developments in a new type of waveguid-
ing structure, which shows very appealing features to be used at the millimeter
and submillimeter-wave bands.

Chapter 7

Conclusions

This thesis was initiated being in pursuit of the general objective of presenting a new solution for low-cost high-gain steerable planar antennas at high frequencies, and studying its viability. From the research tasks that have been carried out for that purpose, the following conclusions are drawn.

- SHW-waveguides are able to propagate several independent local quasi-TEM waves along the propagation direction. Thus, this solution based on an oversized rectangular waveguide emulates the behavior of an array of monomode waveguides without resorting to internal sidewalls to keep waves independent. This fact simplifies the manufacturing process and reduces the final cost of slot arrays.

- The isolation among these local waves allow to realize phase-scanning in the transverse direction of the waveguide.

- SHW-waveguides are narrow band devices but they show an acceptable bandwidth for slot array antennas. The bandwidth can be controlled by the permittivity of the groove-filling material.

- The performance of SHW-waveguides has been validated by means of a low-cost experimental realization. The measurements showed a very confined field pattern that is maintained along the longitudinal direction and gave us an estimation of the bandwidth.

- A method of moments formulation based on the aperture integral equation has been proposed and implemented to solve for scattered fields on corrugated surfaces. This rigorous and efficient code represents a basic tool for the analysis and design of SHWW fed slot arrays.

- Some extensions and improvements of the code were needed to solve for propagated fields inside SHW-waveguides and to study the coupling of a radiating slot to the waveguide.

- The results obtained in the study of slot mutual coupling on SHWW show that definitely the strong transverse attenuation experienced by these local waves within a SHWW makes the coupling between slots belonging to different rows nearly negligible. Therefore, the design of 2-D slot arrays could be simplified.

- An optimized design of a 2-D slot array on a SHWW for circular polarization using the implemented code has been carried out. It has been shown that given the low mutual coupling among rows, an acceptable 2-D design can be obtained just by means of the repetition of a 1-D array.

- In addition, the investigation of SHW-waveguides has inspired the emergence of the ridge gap waveguide. The RGW has a large bandwidth and shows a great potential to make millimeter- and submillimeter-wave circuits and components.

- The RGW is a completely new technology that needs to be characterized as a transmission line. For that purpose, a study of the characteristic impedance has been done. The similarity between this waveguide and a stripline has also been stressed.

- The application of the RGW to the realization of microwave circuits is demonstrated by means of the design, manufacture and measurement of a power divider and a line branch coupler.

- The possibility of integration of the RGW technology with SHWW fed slot arrays is encouraging.

Appendix A

Modal propagation in ideal SHWWs

The aim of this appendix is to demonstrate that within an ideal single hard wall waveguide, i.e., a parallel-plate waveguide formed by a metallic upper face and a PEC/PMC strip grid hard surface as the lower face, which has a distance between the plates less than $\lambda/4$, propagation is only allowed in the longitudinal direction, the one parallel to the strips. It is also found that the only permitted propagation is a quasi-TEM type mode.

A.1 Field expressions

The set of electromagnetic modes that can exist within a certain structure must satisfy Maxwell's equations or the wave equation and the appropriate boundary conditions. It is common practice in the analysis of electromagnetic boundary-value problems to use auxiliary vector potentials as aids in obtaining solutions for the electric $\vec{E}$ and magnetic $\vec{H}$ fields [120]. This is the way followed here.

The electric $\vec{E}$ and magnetic $\vec{H}$ fields are expressed in terms of the vector potencials $\vec{A}$ and $\vec{F}$ as

$$\vec{E} = -\frac{1}{\varepsilon}\nabla \times \vec{F} + \frac{1}{j\omega\mu\varepsilon}\left[\nabla\left(\nabla \cdot \vec{A}\right) + k^2\vec{A}\right] \tag{A.1a}$$

$$\vec{H} = \frac{1}{\mu}\nabla \times \vec{A} + \frac{1}{j\omega\mu\varepsilon}\left[\nabla\left(\nabla \cdot \vec{F}\right) + k^2\vec{F}\right] \tag{A.1b}$$

where

$$k^2 = \omega^2 \mu \varepsilon \tag{A.2}$$

For many electromagnetic boundary-value problems, there are usually many modes that are solutions of Maxwell's equations and the boundary conditions. The most widely known modes are those that are referred to as Transverse ElectroMagnetic (TEM), Transverse Electric (TE), and Transverse Magnetic (TM). TE have the electric field components transverse to a given direction, TM modes have the magnetic field components transverse to a given direction, and TEM modes have both the electric and magnetic field components transverse to a given direction.

Next, the field expressions that will be used later to derive the modal solution within an ideal single hard wall parallel-plate waveguide have been written out. Let us assume TE, TM and TEM modes transverse to z-direction in a rectangular coordinate system.

TM^z modes

To derive field expressions that are TM to z, it is assumed

$$\vec{A} = \hat{z} A_z(x, y, z) \tag{A.3a}$$

$$\vec{F} = 0 \tag{A.3b}$$

then, TM^z fields can be expressed as a function of vector potentials by

$$E_x = \frac{1}{j\omega\mu\varepsilon} \frac{\partial^2 A_z}{\partial x \partial z} \tag{A.4a}$$

$$E_y = \frac{1}{j\omega\mu\varepsilon} \frac{\partial^2 A_z}{\partial y \partial z} \tag{A.4b}$$

$$E_z = \frac{1}{j\omega\mu\varepsilon} \left(\frac{\partial^2}{\partial z^2} + k^2 \right) A_z \tag{A.4c}$$

$$H_x = \frac{1}{\mu} \frac{\partial A_z}{\partial y} \tag{A.4d}$$

$$H_y = -\frac{1}{\mu} \frac{\partial A_z}{\partial x} \tag{A.4e}$$

$$H_z = 0 \tag{A.4f}$$

where

$$k^2 = k_x^2 + k_y^2 + k_z^2 \tag{A.5}$$

TE^z modes

In the same way, to derive field expressions that are TE to z, it is assumed

$$\vec{A} = 0 \tag{A.6a}$$

$$\vec{F} = \hat{z}F_z(x, y, z) \tag{A.6b}$$

then, TE^z fields can be expressed as a function of vector potentials by

$$E_x = -\frac{1}{\varepsilon}\frac{\partial F_z}{\partial y} \tag{A.7a}$$

$$E_y = \frac{1}{\varepsilon}\frac{\partial F_z}{\partial x} \tag{A.7b}$$

$$E_z = 0 \tag{A.7c}$$

$$H_x = \frac{1}{j\omega\mu\varepsilon}\frac{\partial^2 F_z}{\partial x \partial z} \tag{A.7d}$$

$$H_y = \frac{1}{j\omega\mu\varepsilon}\frac{\partial^2 F_z}{\partial y \partial z} \tag{A.7e}$$

$$H_z = \frac{1}{j\omega\mu\varepsilon}\left(\frac{\partial^2}{\partial z^2} + k^2\right)F_z \tag{A.7f}$$

TEM^z modes

TEM^z modes must fulfill $H_z = E_z = 0$, so that we can use the expressions of (A.4) and (A.7) provided that

$$k^2 = k_z^2 \tag{A.8}$$

A.2   Propagation in hard direction

Consider a parallel-plate waveguide consisting of a top metal plate and an ideal hard surface made up of a PEC/PMC strip grid as the bottom plate. Suppose

z-direction is the propagation direction and the hard surface is oriented with the strips parallel to z-axis, as seen in Fig. A.1.

Figure A.1: Propagation direction ($\hat{z}$) parallel to the strips.

The boundary conditions on the upper and lower plates are:

$$E_z(y = 0) = 0 \tag{A.9a}$$

$$H_z(y = 0) = 0 \tag{A.9b}$$

$$E_x(y = d) = 0 \tag{A.9c}$$

$$E_z(y = d) = 0 \tag{A.9d}$$

TM^z modes

For the parallel-plate waveguide, the solutions must take the form

$$A_z = [A \cos (k_y y) + B \sin (k_y y)] e^{-jk_z z} \tag{A.10}$$

where A and B are constants.

To accomplish boundary conditions in (A.9), the solutions should take the form

$$A_z = B \sin (k_y y) e^{-jk_z z} \tag{A.11a}$$

$$k_y = \frac{n\pi}{d}, \quad n = 0, 1, 2, ... \tag{A.11b}$$

The cutoff frequencies of the TM$_n$ modes are

$$f_c|_{TM_n} = n \frac{c}{2d}, \quad n = 0, 1, 2, ... \tag{A.12}$$

where $c = 1/\sqrt{\mu\varepsilon}$.

For $n = 0$, i.e., the TM$_0$ mode, there is no cutoff frequency and $k^2 = k_z^2$, thus this mode is the fundamental mode, i.e., the TEM mode. Next mode is the TM$_1$ appearing at a frequency at which $d > \lambda/2$.

TE^z modes

For the parallel-plate waveguide, the solutions must take the form

$$F_z = [A\cos(k_y y) + B\sin(k_y y)]\, e^{-jk_z z} \tag{A.13}$$

where A and B are constants.

To accomplish boundary conditions in (A.9), the solutions should take the form

$$F_z = B\sin(k_y y)\, e^{-jk_z z} \tag{A.14a}$$

$$k_y = \frac{(2n-1)\,\pi}{2d}, \quad n = 1, 2, ... \tag{A.14b}$$

The cutoff frequencies of the TE$_n$ modes are

$$f_c|_{TE_n} = \frac{2n-1}{2}\frac{c}{2d}, \quad n = 1, 2, ... \tag{A.15}$$

The first TE mode is the TE$_1$ appearing at a frequency at which $d > \lambda/4$.

Conclusion

To sum up, within an ideal single hard wall parallel-plate waveguide, there is only one propagating mode, which is TEM, in the direction parallel to the strips provided that the air gap between plates $d < \lambda/4$.

A.3   Propagation in soft direction

Consider again a parallel-plate waveguide consisting of a top metal plate and a hard surface as the bottom plate. And suppose z-direction as the propagation direction. But now, the hard surface is oriented with the strips transverse to z-axis, as Fig. A.2 shows.

The boundary conditions on the upper and lower plates are:
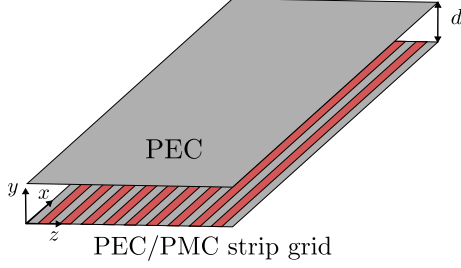
Figure A.2: Propagation direction ($\hat{z}$) transverse to the strips.

$$E_x(y=0) = 0 \tag{A.16a}$$

$$H_x(y=0) = 0 \tag{A.16b}$$

$$E_x(y=d) = 0 \tag{A.16c}$$

$$E_z(y=d) = 0 \tag{A.16d}$$

TM^z modes

For the parallel-plate waveguide, the solutions should have a form as the one of (A.10). To accomplish boundary conditions given in (A.16), the solutions should take the form

$$A_z = A \cos\left(k_y y\right) e^{-jk_z z} \tag{A.17a}$$

$$k_y = \frac{(2n-1)\pi}{2d}, \quad n = 1, 2, ... \tag{A.17b}$$

The cutoff frequencies of the TM$_n$ modes are

$$f_c|_{TM_n} = \frac{2n-1}{2} \frac{c}{2d}, \quad n = 1, 2, ... \tag{A.18}$$

The first TM mode is the TM$_1$ appearing at a frequency at which $d > \lambda/4$.

TE^z modes

For the parallel-plate waveguide, the solutions should have a form as the one of (A.13). To accomplish boundary conditions given in (A.16), the solutions should take the form

$$F_z = B \cos\left(k_y y\right) e^{-jk_z z} \tag{A.19a}$$

$$k_y = \frac{n\pi}{d}, \quad n = 1, 2, ... \tag{A.19b}$$

The cutoff frequencies of the TE_n modes are

$$f_c|_{TE_n} = n\frac{c}{2d}, \quad n = 1, 2, ... \tag{A.20}$$

The first TE mode is the TE_1 appearing at a frequency at which $d > \lambda/2$.

Conclusion

In short, within an ideal single hard wall parallel-plate waveguide, all modes are below cutoff in the direction transverse to the strips provided that the air gap between plates $d < \lambda/4$.

A.4 Propagation in arbitrary direction

Consider again a parallel-plate waveguide consisting of a top metal plate and a hard surface as the bottom plate. And suppose z-direction as the propagation direction. But now, the hard surface is oriented with the strips along l-direction, which forms an angle α with respect to the z-axis and an angle $(\pi - \alpha)$ with respect to the x-axis (see Fig. A.3).
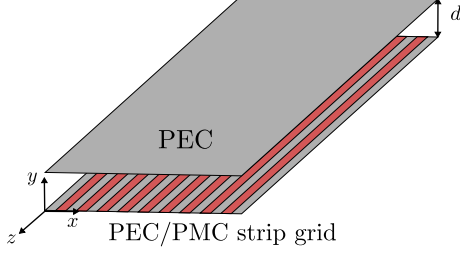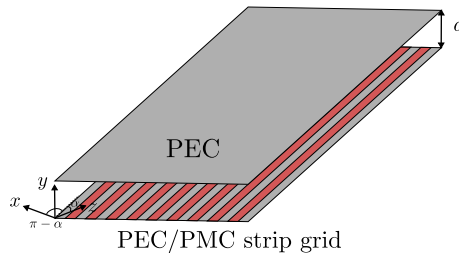

Figure A.3: Propagation direction ($\hat{z}$) arbitrary with respect to the strips.

The boundary conditions on the upper and lower plates are:

$$E_l(y = 0) = E_z(y = 0)\cos\alpha + E_x(y = 0)\sin\alpha = 0 \tag{A.21a}$$

$$H_l(y = 0) = H_z(y = 0)\cos\alpha + H_x(y = 0)\sin\alpha = 0 \tag{A.21b}$$

$$E_x(y = d) = 0 \tag{A.21c}$$

$$E_z(y = d) = 0 \tag{A.21d}$$

TE^z and TM^z modes do not fulfill boundary conditions. Let us consider then hybrid modes as a combination of TE and TM modes.

Hybrid modes

Hybrid modes can be written as

$$E_x = -\frac{1}{\varepsilon}\frac{\partial F_z}{\partial y} + C_{TM}\frac{1}{j\omega\mu\varepsilon}\frac{\partial^2 A_z}{\partial x\partial z} \tag{A.22a}$$

$$E_y = \frac{1}{\varepsilon}\frac{\partial F_z}{\partial x} + C_{TM}\frac{1}{j\omega\mu\varepsilon}\frac{\partial^2 A_z}{\partial y\partial z} \tag{A.22b}$$

$$E_z = C_{TM}\frac{1}{j\omega\mu\varepsilon}\left(\frac{\partial^2}{\partial z^2} + k^2\right)A_z \tag{A.22c}$$

$$H_x = \frac{1}{j\omega\mu\varepsilon}\frac{\partial^2 F_z}{\partial x\partial z} + C_{TM}\frac{1}{\mu}\frac{\partial A_z}{\partial y} \tag{A.22d}$$

$$H_y = \frac{1}{j\omega\mu\varepsilon}\frac{\partial^2 F_z}{\partial y\partial z} - C_{TM}\frac{1}{\mu}\frac{\partial A_z}{\partial x} \tag{A.22e}$$

$$H_z = \frac{1}{j\omega\mu\varepsilon}\left(\frac{\partial^2}{\partial z^2} + k^2\right)F_z \tag{A.22f}$$

where C_{TM} is a constant.
The solutions should take the form

$$A_z = [A\cos(k_y y) + B\sin(k_y y)]\,e^{-jk_z z} \tag{A.23a}$$

$$F_z = [C\cos(k_y y) + D\sin(k_y y)]\,e^{-jk_z z} \tag{A.23b}$$

where A, B, C, and D, are constants.

To accomplish the boundary condition (A.21a)

$$C_{TM} = \frac{D}{A} \frac{j\omega\mu \tan\alpha}{k_y} \tag{A.24}$$

and the boundary condition (A.21b) yields to the equation

$$C_{TM} = \frac{C}{B} \frac{jk_y}{\omega\varepsilon \tan\alpha} \tag{A.25}$$

Equations (A.24) and (A.25) give rise to two sets of solutions, which could be named A-type and B-type hybrid modes.

A-type hybrid modes

From (A.24) and imposing $D = 0$, then $A = 0$ for $C_{TM} \neq 0$. To accomplish boundary conditions (A.21c) and (A.21d), solutions should take the form

$$A_z = B \sin(k_y y) e^{-jk_z z} \tag{A.26a}$$

$$F_z = C \cos(k_y y) e^{-jk_z z} \tag{A.26b}$$

$$C_{TM} = \frac{C}{B} \frac{jk_y}{\omega\varepsilon \tan\alpha} \tag{A.26c}$$

$$k_y = \frac{n\pi}{d}, \quad n = 1, 2, ... \tag{A.26d}$$

The cutoff frequencies of the HA_n modes are

$$f_c|_{HA_n} = n\frac{c}{2d}, \quad n = 1, 2, ... \tag{A.27}$$

For $n = 0$, then $k_y = 0$ and we get the trivial solution. So, the first HA mode is the HA_1 appearing at a frequency at which $d > \lambda/2$.

B-type hybrid modes

From (A.25) and imposing $B = 0$, then $C = 0$ for $C_{TM} \neq 0$. To accomplish boundary conditions (A.21c) and (A.21d), solutions should take the form

$$A_z = A \cos{(k_y y)} \, e^{-jk_z z} \tag{A.28a}$$

$$F_z = D \sin{(k_y y)} \, e^{-jk_z z} \tag{A.28b}$$

$$C_{TM} = \frac{D}{A} \frac{j\omega\mu \tan{\alpha}}{k_y} \tag{A.28c}$$

$$k_y = \frac{(2n-1)\,\pi}{2d}, \quad n = 1, 2, ... \tag{A.28d}$$

The cutoff frequencies of the HB_n modes are

$$f_c|_{HB_n} = \frac{2n-1}{2} \frac{c}{2d}, \quad n = 1, 2, ... \tag{A.29}$$

The first HB mode is the HB_1 appearing at a frequency at which $d > \lambda/4$.

Conclusion

It has been demonstrated that within an ideal single hard wall parallel-plate waveguide, all modes are below cutoff in any direction other than the one parallel to the strips provided that the air gap between plates $d < \lambda/4$, and that the only propagation allowed is TEM.

References

[1] M. Ando, K. Sakurai, and N. Goto, "Characteristics of a radial line slot antenna for 12 GHz band satellite TV reception," *Antennas and Propagation, IEEE Transactions on*, vol. 34, no. 10, pp. 1269–1272, Oct. 1986.

[2] K. Sakakibara, J. Hirokawa, M. Ando, and N. Goto, "High-gain and high-efficiency single-layer slotted waveguide array for use in 22 GHz band," *Electronics Letters*, vol. 32, no. 4, pp. 283–284, Feb. 1996.

[3] Y. Kimura, Y. Miura, T. Shirosaki, T. Taniguchi, Y. Kazama, J. Hirokawa, M. Ando, and T. Shirouzu, "A low-cost and very compact wireless terminal integrated on the back of a waveguide planar array for 26 GHz band Fixed Wireless Access (FWA) systems," *Antennas and Propagation, IEEE Transactions on*, vol. 53, no. 8, pp. 2456–2463, Aug. 2005.

[4] A. Akiyama, T. Yamamoto, J. Hirokawa, M. Ando, E. Takeda, and Y. Arai, "High gain radial line slot antennas for millimetre wave applications," *Microwaves, Antennas and Propagation, IEE Proceedings -*, vol. 147, no. 2, pp. 134–138, Apr. 2000.

[5] J. Hirokawa and M. Ando, "Efficiency of 76-GHz post-wall waveguide-fed parallel-plate slot arrays," *Antennas and Propagation, IEEE Transactions on*, vol. 48, no. 11, pp. 1742–1745, Nov. 2000.

[6] M. Ando, J. Hirokawa, T. Yamamoto, A. Akiyama, Y. Kimura, and N. Goto, "Novel single-layer waveguides for high-efficiency millimeter-wave arrays," *Microwave Theory and Techniques, IEEE Transactions on*, vol. 46, no. 6, pp. 792–799, Jun. 1998.

[7] M. Ando, J. Hirokawa, T. Hirano, P. Hyun, and H. Kai, "Advances in the design of single-layer slotted waveguide arrays and their system applications," in *Applied Electromagnetics and Communications, 2003. ICECom 2003. 17th International Conference on*, Oct. 2003, pp. 352–359.

REFERENCES

[8] M. Sierra Castañer, M. Sierra Pérez, M. Vera Isasa, and J. Fernández Jambrina, "Design method, analysis and prototypes of radial line slot antennas," in *Antennas and Propagation Society International Symposium, 2001. IEEE*, vol. 3, July 2001, pp. 574–577.

[9] M. Bialkowski and P. Davis, "Design and development of a radial line slot array antenna of arbitrary polarisation," in *Microwave Conference, 2000 Asia-Pacific*, 2000, pp. 13–16.

[10] J. Herranz-Herruzo, M. Ferrando-Bataller, and A. Valero-Nogueira, "Optimized design of linearly polarized radial-line slot-array antennas using multiple sweep method of moments," in *Antennas and Propagation Society International Symposium, 2002. IEEE*, vol. 3, June 2002, pp. 526–529.

[11] M. Takahashi, J.-I. Takada, M. Ando, and N. Goto, "A slot design for uniform aperture field distribution in single-layered radial line slot antennas," *Antennas and Propagation, IEEE Transactions on*, vol. 39, no. 7, pp. 954–959, Jul. 1991.

[12] P. Davis and M. Bialkowski, "Linearly polarized radial-line slot-array antennas with improved return-loss performance," *Antennas and Propagation Magazine, IEEE*, vol. 41, no. 1, pp. 52–61, Feb. 1999.

[13] J. Herranz-Herruzo, A. Valero-Nogueira, E. Alfonso-Alos, and D. Sanchez-Escuderos, "New topologies of radial-line slot-dipole array antennas," in *Antennas and Propagation, 2006. EuCAP 2006. First European Conference on*, Nov. 2006, pp. 1–5.

[14] A. Akiyama, T. Yamamoto, M. Ando, and N. Goto, "Numerical optimisation of slot parameters for a concentric array radial line slot antenna," *Microwaves, Antennas and Propagation, IEE Proceedings -*, vol. 145, no. 2, pp. 141–146, Apr. 1998.

[15] A. Simmons, "Circularly polarized slot radiators," *Antennas and Propagation, IRE Transactions on*, vol. 5, no. 1, pp. 31–36, Jan. 1957.

[16] W. Getsinger, "Elliptically polarized leaky-wave array," *Antennas and Propagation, IRE Transactions on*, vol. 10, no. 2, pp. 165–171, Mar. 1962.

[17] R. Johnson, *Antenna engineering handbook*, 1993.

[18] J. Hirokawa, M. Ando, N. Goto, N. Takahashi, T. Ojima, and M. Uematsu, "A low-profile single-layer leaky wave slotted waveguide array for mobile DBS reception," in *Antennas and Propagation Society International Symposium, 1993. AP-S. Digest*, vol. 1, 28 1993, pp. 132–135.

[19] ——, "A low-profile mobile DBS receiving system using a single-layer slotted leaky waveguide array," in *Antennas and Propagation Society International Symposium, 1994. AP-S. Digest*, vol. 2, June 1994, pp. 1012–1015.

[20] J. Hirokawa, K. Sakurai, M. Ando, and N. Goto, "Matching slot pair for a circularly-polarised slotted waveguide array," *Microwaves, Antennas and Propagation, IEE Proceedings H*, vol. 137, no. 6, pp. 367–371, Dec. 1990.

[21] K. Sakakibara, Y. Kimura, J. Hirokawa, M. Ando, and N. Goto, "A two-beam slotted leaky waveguide array for mobile reception of dual-polarization DBS," *Vehicular Technology, IEEE Transactions on*, vol. 48, no. 1, pp. 1–7, Jan. 1999.

[22] T. Hirano, J. Hirokawa, and M. Ando, "Method of moments analysis of a waveguide crossed slot by using the eigenmode basis functions derived by the edge-based finite-element method," *Microwaves, Antennas and Propagation, IEE Proceedings -*, vol. 147, no. 5, pp. 349–353, Oct. 2000.

[23] ——, "Analysis of a waveguide matching crossed slot by the method of moments using numerical eigenmode basis functions," in *Antennas and Propagation Society International Symposium, 2001. IEEE*, vol. 2, 2001, pp. 258–261.

[24] ——, "Design of a waveguide crossed-slot array with matching elements using the method of moments with numerical-eigenmode basis functions," in *Antennas and Propagation Society International Symposium, 2003. IEEE*, vol. 3, June 2003, pp. 1046–1049.

[25] J. Hirokawa, T. Nanbu, M. Ando, and N. Goto, "Circularly-polarized waveguide array with slots and dipoles," in *Antennas and Propagation Society International Symposium, 1991. AP-S. Digest*, vol. 3, June 1991, pp. 1338–1341.

[26] K.-S. Min, J. Hirokawa, K. Sakurai, M. Ando, and N. Goto, "Single-layer dipole array for linear-to-circular polarisation conversion of slotted waveguide array," *Microwaves, Antennas and Propagation, IEE Proceedings -*, vol. 143, no. 3, pp. 211–216, June 1996.

[27] K.-S. Min, J. Hirokawa, M. Ando, and N. Goto, "U-shaped slots for circularly polarized slotted waveguide array," in *Antennas and Propagation Society International Symposium, 1995. AP-S. Digest*, vol. 3, June 1995, pp. 1434–1437.

REFERENCES

[28] K. Sakakibara, J. Hirokawa, M. Ando, and N. Goto, "A slotted waveguide array using reflection-cancelling slot pairs," in *Antennas and Propagation Society International Symposium, 1993. AP-S. Digest*, vol. 3, June 1993, pp. 1570–1573.

[29] J. Hirokawa, M. Kirita, and M. Ando, "A linear array of transverse slots on a hollow waveguide with a layer of parasitic dipole-quartets for sidelobe suppression," in *Microwave Conference, 2007. APMC 2007. Asia-Pacific*, Dec. 2007, pp. 1–4.

[30] H. Uchimura, T. Takenoshita, and M. Fujii, "Development of a laminated waveguide," *Microwave Theory and Techniques, IEEE Transactions on*, vol. 46, no. 12, pp. 2438–2443, Dec. 1998.

[31] D. Deslandes and K. Wu, "Integrated microstrip and rectangular waveguide in planar form," *Microwave and Wireless Components Letters, IEEE*, vol. 11, no. 2, pp. 68–70, Feb. 2001.

[32] S. Yamamoto, J. Hirokawa, and M. Ando, "A beam switching slot array with a 4-way Butler matrix installed in a single layer post-wall waveguide," in *Antennas and Propagation Society International Symposium, 2002. IEEE*, vol. 1, 2002, pp. 138–141.

[33] J. Hirokawa, K. Morimoto, and M. Ando, "Beam-switching single-layer post-wall waveguide slot array controlling crossover and sidelobes," in *Antennas and Propagation, 2007. EuCAP 2007. The Second European Conference on*, Nov. 2007, pp. 1–5.

[34] S.-I. Yamamoto, N. Hikono, J. Hirokawa, and M. Ando, "A 120-degree beamwidth post-wall waveguide slot array with a three-way power divider on a single-layer dielectric substrate," in *Wireless Communication Technology, 2003. IEEE Topical Conference on*, Oct. 2003, pp. 354–355.

[35] K. Sakakibara, T. Takahashi, J. Hirokawa, M. Ando, and N. Goto, "A single layer slotted waveguide array for 22 GHz band radio system between mobile base stations," in *Antennas and Propagation Society International Symposium, 1994. AP-S. Digest*, vol. 1, June 1994, pp. 356–359.

[36] K. Sakakibara, J. Hirokawa, M. Ando, and N. Goto, "A slotted waveguide planar array antenna for entrance radio system in mobile communication," in *Universal Personal Communications. 1995. Record., 1995 Fourth IEEE International Conference on*, Nov. 1995, pp. 373–376.

[37] M. Ando, K. Sakakibara, J. Hirokawa, N. Goto, and T. Watanabe, "A 60 GHz band single-layer planar waveguide arrays," in *Antennas and*

Propagation Society International Symposium, 1996. AP-S. Digest, vol. 1, July 1996, pp. 204–207.

[38] J. Sato, J. Hirokawa, and M. Ando, "Reflection-canceling of slotted waveguide antenna by using a circular pit," in *Antennas and Propagation Society International Symposium, 1998. IEEE*, vol. 3, June 1998, pp. 1706–1709.

[39] S. Park, J. Hirokawa, and M. Ando, "Analysis and design of a waveguide slot and a reflection-canceling inductive wall," in *Wireless Communication Technology, 2003. IEEE Topical Conference on*, Oct. 2003, pp. 362–363.

[40] M. Hossain, J. Hirokawa, and M. Ando, "Parasitic strip dipoles to suppress grating lobes in a waveguide transverse slot array," in *Antennas and Propagation Society International Symposium, 2004. IEEE*, vol. 3, June 2004, pp. 2376–2379.

[41] Y. Kimura, J. Hirokawa, and M. Ando, "Low sidelobe single-layer slotted waveguide arrays at 76 GHz band," in *Antennas and Propagation Society International Symposium, 2000. IEEE*, vol. 1, 2000, pp. 86–89.

[42] S. Park, Y. Okajima, J. Hirokawa, and M. Ando, "A slotted post-wall waveguide array with interdigital structure for 45 deg linear and dual polarization," *Antennas and Propagation, IEEE Transactions on*, vol. 53, no. 9, pp. 2865–2871, Sep. 2005.

[43] Sakakibara, Y. Kimura, A. Akiyama, J. Hirokawa, M. Ando, and N. Goto, "Alternating phase-fed waveguide slot arrays with a single-layer multiple-way power divider," *Microwaves, Antennas and Propagation, IEE Proceedings -*, vol. 144, no. 6, pp. 425–430, Dec. 1997.

[44] Y. Kimura, J. Hirokawa, M. Ando, and N. Goto, "Frequency characteristics of alternating-phase single-layer slotted waveguide array with reduced narrow walls," in *Antennas and Propagation Society International Symposium, 1997. IEEE., 1997 Digest*, vol. 2, July 1997, pp. 1450–1453.

[45] Y. Kimura, J. Hirokawa, and M. Ando, "Alternating-phase single-layer slotted waveguide arrays at 25 GHz band," in *Antennas and Propagation Society International Symposium, 1999. IEEE*, vol. 1, Aug. 1999, pp. 142–145.

[46] Y. Kimura, T. Hirano, J. Hirokawa, and M. Ando, "Alternating-phase fed single-layer slotted waveguide arrays with chokes dispensing with narrow wall contacts," *Microwaves, Antennas and Propagation, IEE Proceedings -*, vol. 148, no. 5, pp. 295–301, Oct. 2001.

REFERENCES

[47] S. Park, Y. Tsunemitsu, J. Hirokawa, and M. Ando, "Center feed single layer slotted waveguide array," *Antennas and Propagation, IEEE Transactions on*, vol. 54, no. 5, pp. 1474–1480, May 2006.

[48] Y. Kimura, M. Takahashi, J. Hirokawa, M. Ando, and M. Haneishi, "76 GHz alternating-phase fed single-layer slotted waveguide arrays with suppressed sidelobes in the E-plane," in *Antennas and Propagation Society International Symposium, 2003. IEEE*, vol. 3, June 2003, pp. 1042–1045.

[49] M. Zhang, J. Hirokawa, and M. Ando, "Design and fabrication of a waveguide two-dimensional slot array with low sidelobe level of -35dB," in *Antennas and Propagation, 2009. EuCAP 2009. 3rd European Conference on*, Mar. 2009, pp. 1300–1303.

[50] K. Hashimoto, J. Hirokawa, and M. Ando, "Parallel plate slot array fed by post-wall center-feed waveguide consisting of T-junctions," in *Antennas and Propagation Society International Symposium, 2008. AP-S 2008. IEEE*, July 2008, pp. 1–4.

[51] Y. Tsunemitsu, J. Hirokawa, M. Ando, G. Yoshida, and N. Goto, "A ridged cross-junction power divider for small blockage and symmetrical slot arrangement in the center-feed single-layer slotted waveguide array," in *Antennas and Propagation Society International Symposium, 2007 IEEE*, June 2007, pp. 457–460.

[52] Y. Tsunemitsu, S. Matsumoto, Y. Kazama, J. Hirokawa, and M. Ando, "Reduction of aperture blockage in the center-feed alternating-phase fed single-layer slotted waveguide array antenna by E- to H-plane cross-junction power dividers," *Antennas and Propagation, IEEE Transactions on*, vol. 56, no. 6, pp. 1787–1790, June 2008.

[53] D. Arai, M. Zhang, K. Sakurai, J. Hirokawa, and M. Ando, "Obliquely arranged feed waveguide for alternating-phase fed single-layer slotted waveguide array," *Antennas and Propagation, IEEE Transactions on*, vol. 53, no. 2, pp. 594–600, Feb. 2005.

[54] J. Hirokawa, M. Ando, and N. Goto, "Waveguide-fed parallel plate slot array antenna," *Antennas and Propagation, IEEE Transactions on*, vol. 40, no. 2, pp. 218–223, Feb. 1992.

[55] M. Castañer, J. Izquierdo, M. Perez, J. Jambrina, and M. Isasa, "Linear polarization parallel plate slot antenna," in *Antennas and Propagation Society International Symposium, 2000. IEEE*, vol. 3, July 2000, pp. 1608–1611.

[56] M. Vera-Isasa, A. Álvarez, M. Sierra-Castañer, and M. Sierra-Pérez, "Broadside parallel-plate slot antenna without dielectric," in *Antennas and Propagation Society International Symposium, 2001. IEEE*, vol. 3, July 2001, pp. 502–505.

[57] M. Sierra-Castañer, M. Vera-Isasa, M. Sierra-Pérez, and J. Fernández-Jambrina, "Double-beam parallel-plate slot antenna," *Antennas and Propagation, IEEE Transactions on*, vol. 53, no. 3, pp. 977–984, Mar. 2005.

[58] J. Hirokawa and M. Ando, "40 GHz parallel plate slot array fed by single-layer waveguide consisting of posts in a dielectric substrate," in *Antennas and Propagation Society International Symposium, 1998. IEEE*, vol. 3, June 1998, pp. 1698–1701.

[59] ——, "Single-layer feed waveguide consisting of posts for plane TEM wave excitation in parallel plates," *Antennas and Propagation, IEEE Transactions on*, vol. 46, no. 5, pp. 625–630, May 1998.

[60] ——, "45 deg linearly polarised post-wall waveguide-fed parallel-plate slot arrays," *Microwaves, Antennas and Propagation, IEE Proceedings -*, vol. 147, no. 6, pp. 515–519, Dec. 2000.

[61] M. Castañer, J. Hirokawa, and M. Ando, "Moment method analysis of parallel plate slot antennas," in *Antennas and Propagation Society International Symposium, 1999. IEEE*, vol. 2, Aug. 1999, pp. 850–853.

[62] H. Kai, J. Hirokawa, and M. Ando, "Analysis of inner fields and aperture illumination of an oversize rectangular slotted waveguide," *Microwaves, Antennas and Propagation, IEE Proceedings -*, vol. 150, no. 6, pp. 415–421, Dec. 2003.

[63] C. Caloz and T. Itoh, *Electromagnetic metamaterials: transmission line theory and microwave applications: the engineering approach.* Wiley-IEEE Press, 2006.

[64] G. Eleftheriades and K. Balmain, *Negative-refraction metamaterials: fundamental principles and applications.* Wiley-IEEE Press, 2005.

[65] N. Engheta and R. Ziolkowski, *Metamaterials: physics and engineering explorations.* Wiley-IEEE Press, 2006.

[66] R. Marqués, F. Martín, and M. Sorolla, *Metamaterials with negative parameters.* Wiley, 2008.

[67] F. Capolino, *Theory and phenomena of metamaterials.* CRC, 2009.

REFERENCES

[68] N. Karmakar and M. Mollah, "Potential applications of PBG engineered structures in microwave engineering: Part I," *Microwave journal*, vol. 47, no. 7, 2004.

[69] ——, "Potential applications of PBG engineered structures in microwave engineering: Part II," *Microwave journal*, vol. 47, no. 9, pp. 122–137, 2004.

[70] E. Yablonovitch, "Photonic band-gap structures," *Journal of the optical society of America B*, vol. 10, no. 2, pp. 283–295, 1993.

[71] ——, "Inhibited spontaneous emission in solid-state physics and electronics," *Physical review letters*, vol. 58, no. 20, pp. 2059–2062, 1987.

[72] I. McKinzie, W.E. and R. Fahr, "A low profile polarization diversity antenna built on an artificial magnetic conductor," in *Antennas and Propagation Society International Symposium, 2002. IEEE*, vol. 1, 2002, pp. 762–765.

[73] A. Feresidis, G. Goussetis, S. Wang, and J. Vardaxoglou, "Artificial magnetic conductor surfaces and their application to low-profile high-gain planar antennas," *Antennas and Propagation, IEEE Transactions on*, vol. 53, no. 1, pp. 209–215, Jan. 2005.

[74] R. Coccioli, F.-R. Yang, K.-P. Ma, and T. Itoh, "Aperture-coupled patch antenna on UC-PBG substrate," *Microwave Theory and Techniques, IEEE Transactions on*, vol. 47, no. 11, pp. 2123–2130, Nov. 1999.

[75] D. Sievenpiper, L. Zhang, R. Broas, N. Alexopolous, and E. Yablonovitch, "High-impedance electromagnetic surfaces with a forbidden frequency band," *Microwave Theory and Techniques, IEEE Transactions on*, vol. 47, no. 11, pp. 2059–2074, Nov. 1999.

[76] E. Rajo-Iglesias, O. Quevedo-Teruel, and L. Inclan-Sanchez, "Mutual coupling reduction in patch antenna arrays by using a planar EBG structure and a multilayer dielectric substrate," *Antennas and Propagation, IEEE Transactions on*, vol. 56, no. 6, pp. 1648–1655, June 2008.

[77] F.-R. Yang, K.-P. Ma, Y. Qian, and T. Itoh, "A uniplanar compact photonic-bandgap (UC-PBG) structure and its applications for microwave circuits," *Microwave Theory and Techniques, IEEE Transactions on*, vol. 47, no. 8, pp. 1509–1514, Aug. 1999.

[78] V. Sanchez, W. McKinzie, and R. Diaz, "Broadband antennas over electronically reconfigurable artificial magnetic conductor surfaces," September 2002, uS Patent App. 10/246,198.

[79] D. Sievenpiper, "Forward and backward leaky wave radiation with large effective aperture from an electronically tunable textured surface," *Antennas and Propagation, IEEE Transactions on*, vol. 53, no. 1, pp. 236–247, Jan. 2005.

[80] F.-R. Yang, K.-P. Ma, Y. Qian, and T. Itoh, "A novel TEM waveguide using uniplanar compact photonic-bandgap (UC-PBG) structure," *Microwave Theory and Techniques, IEEE Transactions on*, vol. 47, no. 11, pp. 2092–2098, Nov. 1999.

[81] M. Kehn and P.-S. Kildal, "Miniaturized rectangular hard waveguides for use in multifrequency phased arrays," *Antennas and Propagation, IEEE Transactions on*, vol. 53, no. 1, pp. 100–109, Jan. 2005.

[82] M. Samardzija, T. Kai, J. Hirokawa, and M. Ando, "Single-layer waveguide feed for uniform plane TEM-wave in oversized-rectangular waveguide with hard-surface sidewalls," *Antennas and Propagation, IEEE Transactions on*, vol. 54, no. 10, pp. 2813–2819, Oct. 2006.

[83] M. Ozkar and A. Mortazawi, "Electromagnetic modeling and optimization of spatial power combiners/dividers with hard horns," *Antennas and Propagation, IEEE Transactions on*, vol. 53, no. 1, pp. 144–150, Jan. 2005.

[84] M. Ali, S. Ortiz, T. Ivanov, and A. Mortazawi, "Analysis and measurement of hard-horn feeds for the excitation of quasi-optical amplifiers," *Microwave Theory and Techniques, IEEE Transactions on*, vol. 47, no. 4, pp. 479–487, Apr. 1999.

[85] J. Fernández and M. Sierra-Castañer, "Electromagnetic bandgap structures as artificial magnetic conductor surfaces sidewalls in parallel plate slot antennas," *Microwave and optical technology letters*, vol. 48, no. 7, pp. 1441–1446, 2006.

[86] H. Xin, T.-C. Chen, and H. Kazemi, "A W-band low-loss dual-polarization quasi-TEM waveguide," *Antennas and Propagation, IEEE Transactions on*, vol. 56, no. 6, pp. 1661–1668, June 2008.

[87] P. de la Torre, J. Fernandez-Gonzalez, and M. Sierra-Castaner, "AMC-PEC-AMC strips in parallel plate waveguides," in *Antennas and Propagation Society International Symposium 2006, IEEE*, July 2006, pp. 1223–1226.

[88] P. de la Torre, J. Fernández, and M. Sierra-Castañer, "Characterization of artificial magnetic conductor strips for parallel plate planar antennas,"

Microwave and Optical Technology Letters, vol. 50, no. 2, pp. 498–504, 2008.

[89] D. Li, F. Boone, M. Bozzi, L. Perregrini, and K. Wu, "Concept of virtual electric/magnetic walls and its realization with artificial magnetic conductor technique," *Microwave and Wireless Components Letters, IEEE*, vol. 18, no. 11, pp. 743–745, Nov. 2008.

[90] P.-S. Kildal, "Artificially soft and hard surfaces in electromagnetics," *Antennas and Propagation, IEEE Transactions on*, vol. 38, no. 10, pp. 1537–1544, Oct. 1990.

[91] E. Lier, "Analysis of soft and hard strip-loaded horns using a circular cylindrical model," *Antennas and Propagation, IEEE Transactions on*, vol. 38, no. 6, pp. 783–793, June 1990.

[92] R. Elliott, "On the theory of corrugated plane surfaces," *Antennas and Propagation, Transactions of the IRE Professional Group on*, vol. 2, no. 2, pp. 71–81, Apr. 1954.

[93] L. Goldstone and A. Oliner, "A note on surface waves along corrugated structures," *Antennas and Propagation, IRE Transactions on*, vol. 7, no. 3, pp. 274–276, July 1959.

[94] H. Minnett and B. Thomas, "A method of synthesizing radiation patterns with axial symmetry," *Antennas and Propagation, IEEE Transactions on*, vol. 14, no. 5, pp. 654–656, Sep. 1966.

[95] V. Rumsey, "Horn antennas with uniform power patterns around their axes," *Antennas and Propagation, IEEE Transactions on*, vol. 14, no. 5, pp. 656–658, Sep. 1966.

[96] P. Clarricoats and P. Saha, "Propagation and radiation behaviour of corrugated feeds. Part 1: Corrugated-waveguide feed," *Electrical Engineers, Proceedings of the Institution of*, vol. 118, no. 9, pp. 1167–1176, Sep. 1971.

[97] P.-S. Kildal and E. Lier, "Hard horns improve cluster feeds of satellite antennas," *Electronics Letters*, vol. 24, no. 8, pp. 491–492, Apr. 1988.

[98] E. Lier and P.-S. Kildal, "Soft and hard horn antennas," *Antennas and Propagation, IEEE Transactions on*, vol. 36, no. 8, pp. 1152–1157, Aug. 1988.

[99] E. Lier, "Hard waveguide feeds with circular symmetry for aperture efficiency enhancement," *Electronics Letters*, vol. 24, no. 3, pp. 166–167, Feb. 1988.

[100] O. Sotoudeh, P.-S. Kildal, P. Ingvarson, and C. Mangenot, "Dual band hard horn for use in cluster-fed multi-beam antennas in Ka-band," in *Antennas and Propagation Society International Symposium, 2005 IEEE*, vol. 3A, July 2005, pp. 379–382.

[101] P.-S. Kildal, "Definition of artificially soft and hard surfaces for electromagnetic waves," *Electronics Letters*, vol. 24, no. 3, pp. 168–170, Apr. 1988.

[102] P. Kildal and A. Kishk, "EM Modeling of surfaces with STOP or GO characteristics - artificial magnetic conductors and soft and hard surfaces," *ACES Journal*, vol. 18, no. 1, pp. 32–40, Mar. 2003.

[103] P.-S. Kildal, A. Kishk, and S. Maci, "Special issue on artificial magnetic conductors, soft/hard surfaces, and other complex surfaces," *Antennas and Propagation, IEEE Transactions on*, vol. 53, no. 1, pp. 2–7, Jan. 2005.

[104] J. Aas, "Plane-wave reflection properties of two artificially hard surfaces," *Antennas and Propagation, IEEE Transactions on*, vol. 39, no. 5, pp. 651–656, May 1991.

[105] ——, "Properties of waves guided between parallel, artificially hard surfaces," in *Antennas and Propagation Society International Symposium, 1993. AP-S. Digest*, vol. 1, June 1993, pp. 390–393.

[106] S. Chen, M. Ando, and N. Goto, "Analytical expressions for reflection coefficients of artificially soft and hard surfaces: dielectric slab loaded with a periodic array of strips over a ground plane," *Microwaves, Antennas and Propagation, IEE Proceedings -*, vol. 142, no. 2, pp. 145–150, Apr. 1995.

[107] I. Lindell, "Image theory for the soft and hard surface," *Antennas and Propagation, IEEE Transactions on*, vol. 43, no. 1, pp. 117–119, Jan. 1995.

[108] Z. Sipus, H. Merkel, and P.-S. Kildal, "Green's functions for planar soft and hard surfaces derived by asymptotic boundary conditions," *Microwaves, Antennas and Propagation, IEE Proceedings -*, vol. 144, no. 5, pp. 321–328, Oct. 1997.

[109] T. Uusitupa, "Polarization and bandwidth studies on finite-width corrugated plates," *Microwave and optical technology letters*, vol. 47, no. 5, pp. 446–454, 2005.

REFERENCES

[110] M. Caiazzo, P.-S. Kildal, S. Maci, and E. Rajo-Iglesias, "Numerical investigation of bandgaps of different soft surfaces: corrugations and strip loaded substrate with vias," in *Antennas and Propagation Society International Symposium, 2005 IEEE*, vol. 2B, July 2005, pp. 312–315.

[111] S. Maci and P.-S. Kildal, "Hard and soft surfaces realized by FSS printed on a grounded dielectric slab," in *Antennas and Propagation Society International Symposium, 2004. IEEE*, vol. 1, June 2004, pp. 285–288 Vol.1.

[112] E. Rajo-Iglesias, M. Caiazzo, L. Inclan-Sanchez, and P.-S. Kildal, "Comparison of bandgaps of mushroom-type EBG surface and corrugated and strip-type soft surfaces," *Microwaves, Antennas Propagation, IET*, vol. 1, no. 1, pp. 184–189, Feb. 2007.

[113] L. Inclan-Sanchez, J. Vazquez-Roy, O. Quevedo-Teruel, and E. Rajo-Iglesias, "New topologies for miniaturized horizontal corrugations," *Antennas and Propagation (EuCAP), 2010 Proceedings of the Fourth European Conference on*, pp. 1–3, Apr. 2010.

[114] E. Rajo-Iglesias, P.-S. Kildal, M. Caiazzo, and J. Yang, "Comparison between bandgaps and bandwidths of back radiation of different narrow soft ground planes," in *Antennas and Propagation Society International Symposium, 2005 IEEE*, vol. 1A, June 2005, pp. 697–700.

[115] P.-S. Kildal, A. Kishk, and A. Tengs, "Reduction of forward scattering from cylindrical objects using hard surfaces," *Antennas and Propagation, IEEE Transactions on*, vol. 44, no. 11, pp. 1509–1520, Nov. 1996.

[116] P.-S. Kildal, A. Kishk, and Z. Sipus, "RF invisibility using metamaterials: Harry Potter's cloak or The Emperor's new clothes?" in *Antennas and Propagation Society International Symposium, 2007 IEEE*, June 2007, pp. 2361–2364.

[117] P.-S. Kildal, "Bandgaps and cloaks with soft and hard surfaces," in *Applied Electromagnetics and Communications, 2007. ICECom 2007. 19th International Conference on*, Sep. 2007, pp. 1–4.

[118] D. Schurig, J. Mock, B. Justice, S. Cummer, J. Pendry, A. Starr, and D. Smith, "Metamaterial electromagnetic cloak at microwave frequencies," *Science Express*, vol. 314, no. 5801, pp. 977–980, Oct. 2006.

[119] M. Samardzija, J. Hirokawa, and M. Ando, "Dominant quasi-TEM mode generator for thin oversized dielectric coated rectangular waveguide," in *Antennas and Propagation Society International Symposium 2007, IEEE*, June 2007, pp. 4272–4275.

[120] C. Balanis, *Advanced engineering electromagnetics.* Wiley New York, 1989.

[121] E. Alfonso, A. Valero-Nogueira, J. Herranz, and D. Sánchez, "Oversized waveguides for TEM propagation using hard surfaces," in *Antennas and Propagation Society International Symposium 2006, IEEE*, July 2006, pp. 1193–1196.

[122] A. Valero-Nogueira, E. Alfonso, J. Herranz, and M. Baquero, "Planar slot-array antenna fed by an oversized quasi-TEM waveguide," *Microwave and Optical Technology Letters*, vol. 49, no. 8, pp. 1875–1877, 2007.

[123] A. Valero-Nogueira, E. Alfonso, and J. Herranz, "Multi-beam waveguide for quasi-TEM modes," Spanish Patent No. P200803558, December 2008.

[124] G. Ruvio, P.-S. Kildal, and S. Maci, "Modal propagation in ideal soft and hard waveguides," in *Antennas and Propagation Society International Symposium 2003, IEEE*, vol. 4, June 2003, pp. 438–441.

[125] M. Silveirinha, C. Fernandes, and J. Costa, "Electromagnetic characterization of textured surfaces formed by metallic pins," *Antennas and Propagation, IEEE Transactions on*, vol. 56, no. 2, pp. 405–415, Feb. 2008.

[126] CST Microwave Studio 2010. Available at: www.cst.com.

[127] S. Skobelev and P.-S. Kildal, "Analysis of global eigenmodes in an oversized rectangular waveguide with a hard surface on one broad wall for planar slot array antenna applications," in *Antennas and Propagation, 2009. EuCAP 2009. 3rd European Conference on*, Mar. 2009, pp. 41–44.

[128] Z. Sipus, M. Bosiljevac, and P.-S. Kildal, "Local wave Green's functions of parallel plate metamaterial-based gap waveguides with one hard wall," in *Antennas and Propagation, 2009. EuCAP 2009. 3rd European Conference on*, Mar. 2009, pp. 37–40.

[129] E. Alfonso, P.-S. Kildal, A. Valero, and J. Herranz, "Study of local quasi-TEM waves in oversized waveguides with one hard wall for killing higher order global modes," in *Antennas and Propagation Society International Symposium, 2008. AP-S 2008. IEEE*, July 2008, pp. 1–4.

[130] A. Valero-Nogueira, E. Alfonso, J. Herranz, and P.-S. Kildal, "Experimental demonstration of local quasi-TEM gap modes in single-hard-wall waveguides," *Microwave and Wireless Components Letters, IEEE*, vol. 19, no. 9, pp. 536 –538, Sep. 2009.

REFERENCES

[131] P. Kildal, A. Kishk, and Z. Sipus, "Asymptotic boundary conditions for strip-loaded and corrugated surfaces," *Microwave and optical technology letters*, vol. 14, no. 2, pp. 99–101, 1997.

[132] A. Kishk, P. Kildal, A. Monorchio, and G. Manara, "Asymptotic boundary condition for corrugated surfaces, and its application to scattering from circular cylinders with dielectric filled corrugations," *IEE Proceedings-Microwaves, Antennas and Propagation*, vol. 145, p. 116, 1998.

[133] T. Uusitupa, "Usability studies on approximate corrugation models in scattering analysis," *Antennas and Propagation, IEEE Transactions on*, vol. 54, no. 9, pp. 2486–2496, Sep. 2006.

[134] I. Hanninen and K. Nikoskinen, "Implementation of method of moments for numerical analysis of corrugated surfaces with impedance boundary condition," *Antennas and Propagation, IEEE Transactions on*, vol. 56, no. 1, pp. 278–281, Jan. 2008.

[135] R. Harrington and J. Mautz, "A generalized network formulation for aperture problems," *Antennas and Propagation, IEEE Transactions on*, vol. 24, no. 6, pp. 870–873, Nov. 1976.

[136] A. Peterson, S. Ray, and R. Mittra, *Computational methods for electromagnetics*. IEEE Press, 1998.

[137] S. Singh, W. Richards, J. Zinecker, and D. Wilton, "Accelerating the convergence of series representing the free space periodic Green's function," *Antennas and Propagation, IEEE Transactions on*, vol. 38, no. 12, pp. 1958–1962, Dec. 1990.

[138] M. Cátedra, R. Torres, J. Basterrechea, and E. Gago, *The CG-FFT method: Application of signal processing techniques to electromagnetics*. Artech House Boston, MA, 1995.

[139] E. Alfonso, A. Valero-Nogueira, J. Herranz, and F. Vico, "Moment method analysis of corrugated surfaces using the aperture integral equation," *Antennas and Propagation, IEEE Transactions on*, vol. 57, no. 7, pp. 2208–2212, July 2009.

[140] P.-S. Kildal, "Waveguides and transmission lines in gaps between parallel conducting surfaces," European patent application EP08159791.6, July 2008.

[141] P.-S. Kildal, E. Alfonso, A. Valero-Nogueira, and E. Rajo-Iglesias, "Local metamaterial-based waveguides in gaps between parallel metal plates,"

Antennas and Wireless Propagation Letters, IEEE, vol. 8, pp. 84–87, 2009.

[142] P.-S. Kildal, "Three metamaterial-based gap waveguides between parallel metal plates for mm/submm waves," in *Antennas and Propagation, 2009. EuCAP 2009. 3rd European Conference on*, Mar. 2009, pp. 28–32.

[143] E. Pucci, A. U. Zaman, E. Rajo-Iglesias, P.-S. Kildal, and A. Kishk, "Losses in ridge gap waveguide compared with rectangular waveguides and microstrip transmission lines," in *Antennas and Propagation (Eu-CAP), 2010 Proceedings of the Fourth European Conference on*, Apr. 2010, pp. 1–4.

[144] E. Alfonso, P.-S. Kildal, A. Valero-Nogueira, and J. Herranz, "Numerical analysis of a metamaterial-based ridge gap waveguide with a bed of nails as parallel-plate mode killer," in *Antennas and Propagation, 2009. EuCAP 2009. 3rd European Conference on*, Mar. 2009, pp. 23–27.

[145] E. Rajo-Iglesias, A. Zaman, and P.-S. Kildal, "Parallel plate cavity mode suppression in microstrip circuit packages using a lid of nails," *Microwave and Wireless Components Letters, IEEE*, vol. 20, no. 1, pp. 31–33, Jan. 2010.

[146] P.-S. Kildal, A. Zaman, E. Rajo-Iglesias, E. Alfonso, and A. Valero-Nogueira, "Design and experimental verification of ridge gap waveguide in bed of nails for parallel-plate mode suppression," *Microwaves, Antennas Propagation, IET*, vol. 5, no. 3, pp. 262–270, Feb. 2011.

[147] A. Grbic and G. Eleftheriades, "Periodic analysis of a 2-d negative refractive index transmission line structure," *Antennas and Propagation, IEEE Transactions on*, vol. 51, no. 10, pp. 2604–2611, Oct. 2003.

[148] B. K. Eleftheriades, G.V., "Metamaterials for controlling and guiding electromagnetic radiation," US Patent 6859114, June 2003.

[149] A. Polemi and S. Maci, "Closed form expressions for the modal dispersion equations and for the characteristic impedance of a metamaterial-based gap waveguide," *Microwaves, Antennas Propagation, IET*, vol. 4, no. 8, pp. 1073–1080, Aug. 2010.

[150] A. Polemi, S. Maci, and P.-S. Kildal, "Dispersion characteristics of a metamaterial-based parallel-plate ridge gap waveguide realized by bed of nails," *Antennas and Propagation, IEEE Transactions on*, vol. 59, no. 3, pp. 904–913, Mar. 2011.

[151] E. Rajo-Iglesias and P.-S. Kildal, "Numerical studies of bandwidth of parallel-plate cut-off realised by a bed of nails, corrugations and mushroom-type electromagnetic bandgap for use in gap waveguides," *Microwaves, Antennas Propagation, IET*, vol. 5, no. 3, pp. 282–289, Feb. 2011.

[152] M. Bosiljevac, Z. Sipus, and P.-S. Kildal, "Construction of Green's functions of parallel plates with periodic texture with application to gap waveguides - a plane-wave spectral-domain approach," *Microwaves, Antennas Propagation, IET*, vol. 4, no. 11, pp. 1799–1810, Nov. 2010.

[153] E. Alfonso, P.-S. Kildal, A. Valero-Nogueira, and M. Baquero, "Study of the characteristic impedance of a ridge gap waveguide," in *Antennas and Propagation Society International Symposium, 2009. APSURSI '09. IEEE*, June 2009, pp. 1–4.

[154] E. Alfonso, M. Baquero, A. Valero-Nogueira, J. Herranz, and P.-S. Kildal, "Power divider in ridge gap waveguide technology," in *Antennas and Propagation, 2010. EuCAP 2010. 4th European Conference on*, Apr. 2010.

[155] D. Pozar, *Microwave engineering*. Wiley, 2005.

[156] E. Alfonso, M. Baquero, P.-S. Kildal, A. Valero-Nogueira, E. Rajo-Iglesias, and J. Herranz, "Microwave circuits in ridge-gap waveguide technology," in *Microwave Symposium, 2010. IEEE/MTT-S International*, May 2010.

Related Publications

JCR indexed journals

1. A. Valero-Nogueira, E. Alfonso, J. I. Herranz, and M. Baquero, "Planar slot-array antenna fed by an oversized quasi-TEM waveguide," *Microwave and Optical Technology Letters*, vol. 49, no. 8, pp. 1875-1877, 2007.

2. E. Alfonso, A. Valero-Nogueira, J. I. Herranz, and F. Vico, "Moment method analysis of corrugated surfaces using the aperture integral equation," *Antennas and Propagation, IEEE Transactions on*, vol. 57, no. 7, pp. 2208-2212, July 2009.

3. A. Valero-Nogueira, E. Alfonso, J. I. Herranz, and P.-S. Kildal, "Experimental demonstration of local quasi-TEM gap modes in single-hard-wall waveguides," *Microwave and Wireless Components Letters, IEEE*, vol. 19, no. 9, pp. 536-538, Sept. 2009.

4. P.-S. Kildal, E. Alfonso, A. Valero-Nogueira, and E. Rajo-Iglesias, "Local metamaterial-based waveguides in gaps between parallel metal plates," *Antennas and Wireless Propagation Letters, IEEE*, vol. 8, pp. 84-87, 2009.

5. P.-S. Kildal, A. Zaman, E. Rajo-Iglesias, E. Alfonso, and A. Valero-Nogueira, "Design and experimental verification of ridge gap waveguide in bed of nails for parallel-plate mode suppression," *Microwaves, Antennas Propagation, IET*, vol. 5, no. 3, pp. 262–270, Feb. 2011.

International conferences

1. E. Alfonso, A. Valero-Nogueira, J. I. Herranz, and D. Sánchez, "Oversized waveguides for TEM propagation using hard surfaces," in *Antennas and Propagation Society International Symposium 2006, IEEE*, July 2006, pp. 1193-1196.

RELATED PUBLICATIONS

2. E. Alfonso, A. Valero-Nogueira, J. I. Herranz, and V.-M. Rodrigo-Peñarrocha, "Slot array fed by an oversized TEM waveguide," in *Antennas and Propagation, 2006. EuCAP 2006. First European Conference on*, Nov. 2006, pp. 1-5.

3. E. Alfonso, A. Valero-Nogueira, J. I. Herranz, and F. Vico, "Optimization of hard surfaces within parallel-plate waveguides applied to slot-array antennas," in *Antennas and Propagation, 2007. EuCAP 2007. The Second European Conference on*, June 2007, pp. 1-6.

4. E. Alfonso, A. Valero, J. I. Herranz, and D. Sánchez, "Analysis and applications of hard surfaces within parallel-plate waveguides," in *Antennas and Propagation Society International Symposium, 2007 IEEE*, Nov. 2007, pp. 453-456.

5. E. Alfonso, P.-S. Kildal, A. Valero, and J. I. Herranz, "Study of local quasi-TEM waves in oversized waveguides with one hard wall for killing higher order global modes," in *Antennas and Propagation Society International Symposium, 2008. AP-S 2008. IEEE*, July 2008, pp. 1-4.

6. E. Alfonso, P.-S. Kildal, A. Valero-Nogueira, and J. I. Herranz, "Numerical analysis of a metamaterial-based ridge gap waveguide with a bed of nails as parallel-plate mode killer," in *Antennas and Propagation, 2009. EuCAP 2009. 3rd European Conference on*, Mar. 2009, pp. 23-27.

7. E. Alfonso, P.-S. Kildal, A. Valero-Nogueira, and M. Baquero, "Study of the characteristic impedance of a ridge gap waveguide," in *Antennas and Propagation Society International Symposium, 2009. APSURSI '09. IEEE*, June 2009, pp. 1-4.

8. E. Alfonso, A. Valero-Nogueira, J. I. Herranz, and F. Vico, "Analysis of a multi-quasi-TEM-mode oversized waveguide with one hard wall using the aperture integral equation," in *Antennas and Propagation Society International Symposium, 2009. APSURSI '09. IEEE*, June 2009, pp. 1-4.

9. E. Alfonso, A. Valero-Nogueira, E. Rajo-Iglesias, U. Ashraf, M. Baquero, and P.-S. Kildal, "The ridge gap waveguide: operation and characterization as transmission line," in *Young Scientist Meeting on Metamaterials 2009*, July 2009.

10. P.-S. Kildal, E. Rajo-Iglesias, E. Alfonso, A. Valero, and A. Zaman, "Wideband, lowloss, low-cost, quasi-TEM metamaterial-based local waveguides in air gaps between parallel metal plates," in *Electromagnetics in Advanced Applications, 2009. ICEAA '09. International Conference on*, Oct. 2009, pp. 588-591.

11. E. Alfonso, M. Baquero, A. Valero-Nogueira, J. I. Herranz, and P.-S. Kildal, "Power divider in ridge gap waveguide technology," in *Antennas and Propagation, 2010. EuCAP 2010. 4th European Conference on*, Apr. 2010.

12. E. Alfonso, M. Baquero, P.-S. Kildal, A. Valero-Nogueira, E. Rajo-Iglesias, and J. I. Herranz, "Microwave circuits in ridge-gap waveguide technology," in *Microwave Symposium, 2010. IEEE/MTT-S International*, May 2010.

13. E. Alfonso, A. Valero-Nogueira, J. Herranz, and F. Vico, "Slot arrays on single-hard-wall waveguides: a study of slot mutual coupling using the aperture integral equation," in *Antennas and Propagation Society International Symposium, 2010. APSURSI '10. IEEE*, July 2010.

14. E. Alfonso, A. Valero-Nogueira, J. Herranz, and D. Sánchez-Escuderos, "Oversized waveguides for multiple local quasi-TEM waves using hard surfaces," in *Young Scientist Meeting on Metamaterials 2011*, Feb. 2011.

National conferences

1. E. Alfonso, A. Valero-Nogueira, J. I. Herranz, and D. Sánchez, "Análisis eficiente de estructuras periódicas finitas mediante CG-FFT," in *Simposium Nacional de la URSI 2005*, Sep. 2005.

2. E. Alfonso, F. Vico, A. Valero-Nogueira, and D. González, "Análisis eficiente de un reflectarray mediante el AIM," in *Simposium Nacional de la URSI 2005*, Sep. 2005.

3. E. Alfonso, A. Valero-Nogueira, J. I. Herranz, and D. Sánchez, "Propagación TEM en guiaondas sobredimensionadas mediante superficies hard," in *Simposium Nacional de la URSI 2006*, Sep. 2006.

4. E. Alfonso, A. Valero-Nogueira, J. I. Herranz, and P.-S. Kildal, "Estudio de ondas quasi-TEM locales en guías anchas con una pared hard para eliminar los modos de orden superior," in *Simposium Nacional de la URSI 2008*, Sep. 2008.

Patents

1. A. Valero-Nogueira, E. Alfonso, and J. I. Herranz, "Multi-beam waveguide for quasi-TEM modes," Spanish Patent No. P200803558, December 2008.